RCA Review

December 1975 Volume 36 No. 4

RCARCI 36(4) 653-786(1975)

RCA Review, published quarterly in March, June, September and December by RCA Research and Engineering, RCA Corporation, Princeton, New Jersey 08540. Entered as second class matter July 3, 1950 under the Act of March 3, 1879. Second-class postage paid at Princeton, New Jersey, and at additional mailing offices. Effective Jan. 1, 1971, subscription rates as follows: United States and Canada: one year $6.00, two years $10.50, three years $13.50; in other countries, one year $6.40, two years $11.30, three years $14.70. Single copies (except for special issues) up to five years old $3.00.

RCA Review

A technical journal published quarterly by RCA Research and Engineering in cooperation with the subsidiaries and divisions of RCA.

Contents

December 1975 Volume 36 Number 4

Spontaneous-Emission-Rate Alteration by Dielectric and Other Waveguiding Structures*

James P. Wittke

RCA Laboratories, Princeton, N.J. 08540

Abstract—The spontaneous emission rate of an excited electron is altered by the presence of structures that, at least partially, localize the electromagnetic fields. This effect is discussed in connection with the dielectric waveguide associated with double heterojunction structures in light-emitting diodes and with (lossless) microwave waveguides.

Introduction

In 1946, Purcell[1] pointed out that the spontaneous emission rate of an excited electron can be drastically altered by its surroundings. In particular, he showed that enclosing a nuclear spin, spontaneously emitting at a radio frequency, in a high-Q resonant cavity can increase its radiation rate by orders of magnitude. An example of the effect in the optical frequency range was given by Drexhage,[2] who altered the fluorescent lifetime of a Eu chelate by bringing it very close to a flat mirror. Variants of this latter system have received considerable attention in the literature.[3,4] However, in the literature of quantum electronics, the fact that structures that can direct (guide) the flow of electromagnetic energy will alter the coupling of the field to a radiating electron has been neglected.[5] This paper will discuss this effect by applying it to an important type of light source, the double

* The research reported in this paper was jointly sponsored by the Department of the Navy, Office of Naval Research, under Contract No. N00014-75-C-0365, and by RCA Laboratories, Princeton, N.J.

heterojunction light-emitting diode (LED). It will be shown how the presence of heterojunctions in an LED can alter the radiation from such a diode in a way that is of considerable practical significance for the utilization of such LED's in optical communications.

The usual non-relativistic theoretical treatment of spontaneous emission uses perturbation theory, and leads to a transition probability given by Fermi's "Golden Rule",[6]

$$w = \frac{1}{\hbar^2}|\langle f|H_1|i\rangle|^2 \cdot \rho(\nu). \qquad [1]$$

Here w is the emission probability per unit time, $\langle f|H_1|i\rangle$ is the matrix element of the term in the Hamiltonian coupling the radiating electron to the radiation field, and $\rho(\nu)$ is the density of final states at the emission frequency ν. Eq. [1] is derived[6] by assuming that the matrix elements are essentially the same for all possible radiation modes in the appropriate frequency range. This assumption is valid when the electron radiates into (the plane-wave modes of) free space, but, in the presence of structure that affects the spatial distribution of the electromagnetic fields, the radiation modes can become quite different, altering the mode density (in frequency space) and making the matrix elements drastically different from one another.

Edge-Emitting Double-Heterojunction LED

As an example, consider the case of an edge-emitting double-heterojunction LED such as used[7] in optical fiber communications. Here the recombination of electrons and holes occurs in a thin slab of high-index-of-refraction material sandwiched between two (thick) regions of lower index. (For simplicity, we assume the two low-index regions to be identical; extension of the argument to the asymmetric case is straight-forward.) It is well known[8] that a constant-thickness slab of high-index material sandwiched between two (assumed infinitely thick) regions of (equal) lower index can support modes of the electromagnetic field that are *guided*, in the sense that the field energy density decreases exponentially with distance away from the slab, with the highest fields occurring within the high-index slab. This situation is quite similar to that treated in the literature[4] for chelate fluorescence between two parallel, plane mirrors. In addition to these guided modes, in the double heterojunction LED there exist *unguided* modes in which significant electromagnetic energy density is found throughout all regions of the system. To describe the modes, consider the electromagnetic field to be confined to a large cubical box, of side L, filled with dielectric of relatively low index except in a

thin slab of higher-index material that extends across the middle of the box, parallel to the top face, and intersecting the four vertical walls of the box (see Fig. 1a). The standard assumption[9] of periodic boundary conditions on the walls of the box will be made. In the limit of vanishing slab thickness, the modes become the usual (unguided) plane waves.

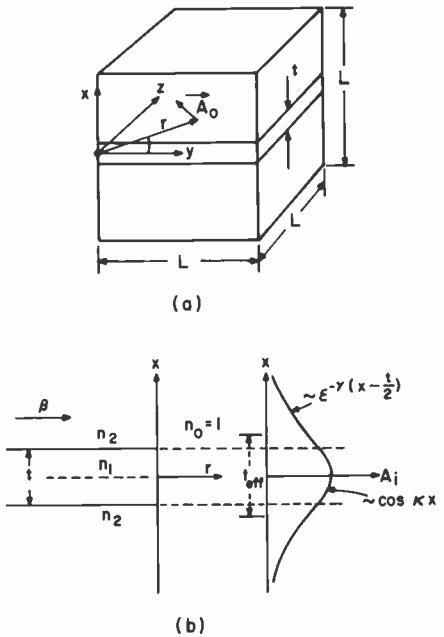

Fig. 1—Geometry of the system. (a) The normalization cube with the higher-index slab, of thickness t, extending across it. The radial coordinate r and the field vector A_0 are parallel to the y-z plane. (b) Details of the high-index region near an air–semiconductor interface. The field pattern for the lowest order TE mode is also shown.

The presence of the slab perturbs all the modes. Its effect is that of a Fabry-Perot interferometer placed in the cavity. However, for the index differences available with (AlGa)As heterojunctions, $\Delta n < 0.3$, the finesse of this interferometer is essentially zero: the maximum power reflectivity at normal incidence is only about 0.002. Thus, except for modes that correspond to energy flow at grazing angles of incidence to the slab, the modes are essentially unchanged by the presence of the slab, with the field intensity within the slab not differing significantly from that outside (apart from that associated with the

index difference). In other words, there are no appreciable resonant enhancements of the fields (standing waves) within the slab.

A few modes, however, are *strongly* perturbed by the presence of the higher-index slab. These include the guided modes.[8] The guided modes of such a system have been discussed in connection with the modes of "integrated optics" structures[10] and of injection lasers.[11] It is these modes that can strongly alter both the spontaneous emission probability of electrons recombining between the two heterojunctions and the isotropy of the emitted radiation. Since the guided modes are so few in number compared to the vast number of unguided ones, it might be thought that their overall effect might be negligible. However, this is not the case, since the radiating electrons couple much more strongly to a guided mode than to an unguided one.

Effect on Matrix Elements

Consider first the matrix elements $\langle f|H_1|i\rangle$. The interaction term H_1 in the Hamiltonian that couples the electronic states to the radiation modes can be taken of the form appropriate to an electric dipole:

$$H_1 = -\frac{e}{m}\,\mathbf{p}\cdot\mathbf{A}, \qquad [2]$$

where $\mathbf{p}$ is the electron momentum operator and $\mathbf{A}$ is the vector potential of the radiation field. The $\mathbf{p}$ operator acts on the electron coordinates, while the $\mathbf{A}$ operator acts on those of the radiation field. When the electronic states are not discrete, as implicitly assumed in the usual derivation of Eq. (1), the situation becomes more complex. For the case of a minority carrier recombining in a semiconductor, the problem becomes a many-body one, and even in the one-electron band approximation, the electron can occupy a continuum of states. Some of the problems arising from these complications have been treated by Lasher and Stern.[12] However, only the electron-coordinate part of the interaction requires modification; that part of the matrix element depending upon the radiation field, and hence on the heterojunction structure, is unaffected. Therefore, for the present considerations, one can ignore the details of the electronic part of the process.

The radiation field can be decomposed in a superposition of modes:

$$\mathbf{A} = \sum_i q_i \mathbf{A}_i. \qquad [3]$$

With the fields confined to a large cubical box filled with a homogeneous dielectric, the modes can be taken as plane waves. With a high-

index slab crossing the box, the associated guided modes have their peak amplitude within the slab, with an exponential decay in the direction perpendicular to the slab outside it, while the unguided modes are essentially the plane waves. In quantizing the radiation field, the mode amplitudes q_i become the usual photon creation and annihilation operators. The spatial terms describing the fields of the modes $\mathbf{A}_i$ must form a complete orthonormal set:[13]

$$\int \mathbf{A}_i \cdot \mathbf{A}_j \, dv = \delta_{ij}. \tag{4}$$

The quasi-plane wave unguided modes will therefore have a normalization constant proportional to $L^{-3/2}$. In the case of the guided modes, however, the mode energy is confined to a much smaller region, and the corresponding normalization factor is $(Lt_{eff}{}^{1/2})^{-1}$. Here t_{eff} is an effective mode width.[14] The normalization condition, therefore, gives, for the unguided (plane wave) modes,

$$|\langle f|H_1|i\rangle_u|^2 = \frac{B}{L^3}, \tag{5}$$

where B is a constant incorporating the details of the electronic states. Similarly, for the guided modes,

$$|\langle f|H_1|i\rangle_g|^2 = \frac{B}{L^2 t_{eff}}. \tag{6}$$

The value of t_{eff} is obtained from the details of the modal pattern. These are discussed in the literature,[15] where it is shown that, for the lowest order guided TE mode, the field is given by

$$\mathbf{A}_1 = \mathbf{A}_0 \exp(i\beta r) \cdot \begin{cases} \cos \kappa x, & |x| \leqslant \tfrac{1}{2}t, \\ \cos \kappa t/2 \cdot \exp[-\gamma(|x| - t/2)], & |x| \geqslant \tfrac{1}{2}t. \end{cases} \tag{7}$$

Here r is the (two-dimensional) radial coordinate in the plane of the slab and β is the guided-mode propagation constant (in this plane); see Fig. 1. $\mathbf{A}_0$ is the plane of the slab, and is perpendicular to the propagation direction $\mathbf{r}$. The parameters κ and γ are given by

$$\kappa^2 = n_1{}^2 k_0{}^2 - \beta^2,$$
$$\gamma^2 = \beta^2 - n_2{}^2 k_0{}^2, \tag{8}$$

where $k_0 = 2\pi/\lambda_0$ is the free-space propagation constant of an optical wave of the same frequency ν. The lowest TE mode is determined by the eigenvalue equation

$$\tan \frac{\kappa t}{2} = \frac{\gamma}{\kappa}. \qquad [9]$$

For this lowest mode, the effective mode width t_{eff} is

$$t_{eff} = \frac{t}{2} + \frac{1}{\gamma}. \qquad [10]$$

Effect on Mode Density

The density of unguided modes will be essentially unchanged from that of a box filled with homogeneous semiconductor, without the heterojunctions. Thus[16]

$$\rho_u(\nu) = \frac{8\pi\nu^2 {n_2}^3}{c^3} \cdot L^3. \qquad [11]$$

For the guided modes, in the y-z plane parallel to the junction, the mode density is determined by the periodic boundary conditions on the cubical box, while the boundary conditions at the heterojunctions determine the number N of "mode types" in the x-direction perpendicular to the junction. N is given by[8]

$$N = 2 \cdot \text{largest integer in} \left[\frac{2t\sqrt{{n_1}^2 - {n_2}^2}}{\lambda_0} + 1 \right]. \qquad [12]$$

For these guided modes, the mode density is

$$\rho_g(\nu) = \sum^{N} \frac{1}{\pi} \beta \frac{d\beta}{d\nu} \cdot L^2. \qquad [13]$$

Under the conditions found in (AlGa)As double-heterojunction LED's used for fiber-optics light sources, only a few (generally well under a dozen) types of guided modes can exist.

Effect on Emission Rate

In the geometry of interest, there are thus two classes of modes, and the "Golden Rule" becomes

$$w = \frac{1}{\hbar^2} [|\langle f|H_1|i\rangle_u|^2 \cdot \rho_u(\nu) + \cdot \langle f|H_1|i\rangle_g|^2 \rho_g(\nu)], \qquad [14]$$

where the subscripts u and g refer to unguided and guided modes. This becomes

$$w = \frac{1}{\hbar^2}\left[\frac{B}{L^3}\cdot\frac{8\pi\nu^2 n_2{}^3}{c^3}L^3 + \sum^{N}\frac{B}{L^2 t_{eff}}\cdot\frac{1}{\pi}\beta\frac{d\beta}{d\nu}\cdot L^2\right]$$

$$= \frac{8\pi\nu^2 n_2{}^3 B}{\hbar^2 c^3}\left[1 + \frac{\lambda_0{}^2 c}{8\pi^2 n_2{}^3}\sum^{N}\frac{\beta}{t_{eff}}\cdot\frac{d\beta}{d\nu}\right] \qquad [15]$$

The first term corresponds to the normal spontaneous decay in a homogeneous slab of semiconductor; the second shows how the spontaneous radiation rate is increased by the presence of the wave-guiding, high-index slab.

Consider the case when the index differences at the heterojunctions and the slab thickness t are such that only the lowest order TE (and TM) modes can propagate. (Then, for "strong" heterojunctions where $\Delta n = 0.3$, the slab must be less than $t = 0.30$ μm in thickness; for "weaker" junctions where $\Delta n = 0.05$, $t < 0.74$ μm.) In the limit $t \to 0$,

$$\beta \to n_2 k_0$$

$$t_{eff} \to \frac{1}{\gamma} \to \frac{2}{(n_1{}^2 - n_2{}^2)k_0{}^2 t}, \qquad [16]$$

and, for the (two) fundamental guided modes,

$$w_{g0} \to \frac{8\pi\nu^2 n_2{}^3 B}{\hbar^2 c^3}\left[\frac{2\pi^2(n_1{}^2 - n_2{}^2)t}{n_2\gamma_0}\right]. \qquad [17]$$

Thus, in this limit, the effects of the modes vanish as $t \to 0$, as they must. In the limit of $t \to \infty$, other guided modes must of course be included; for the fundamental modes (and most of the other guided modes as well),

$$\beta \to n_1 k_0$$

$$t_{eff} \to \frac{t}{2} \qquad [18]$$

and, for the (two) fundamental modes,

$$w_{g0} \to \frac{8\pi\nu^2 n_2{}^3 B}{\hbar^2 c^3}\left[\frac{2n_1{}^2\lambda_0}{n_2{}^3 t}\right]. \qquad [19]$$

Thus, their effects also disappear as $t \to \infty$. In the $t \to 0$ limit, the effects vanish because the slab provides but weak guiding and the fundamental modes are essentially unguided; in the $t \to \infty$ limit, the heterojunctions are so far away from nearly all the recombining electrons that their effects are negligible.

Nevertheless, there is an important intermediate range of slab thicknesses where the radiation into the guided modes can exceed

that into the unguided modes. Moreover, it is possible that this can occur under conditions such that the resultant beam pattern radiated from the edge of the LED is much more directive than that of a Lambertian emitter. This is of great practical importance, for it means, not only that the 2% external emission efficiency as limited by total internal reflection at the (planar) air-semiconductor interface can be significantly exceeded, but also that the associated beam angle can match the (limited) acceptance cone on an optical fiber much better than would otherwise be expected. Moreover, the increased spontaneous radiation rate corresponds to shorter LED response times[17] although it is difficult to separate this effect experimentally from others that are apt to occur with thin double-heterojunction structures.

One particularly favorable structure is a double-heterojunction with a large index difference across the junctions and a very thin ($t < 0.5\ \mu m$) high-index slab. The far-field patterns of the guided modes for such systems have been discussed in the literature[18,19] for injection lasers (the mode patterns are, of course, the same). The calculations indicate that the far-field beam pattern decreases in angular width (perpendicular to the junction plane) as the slab width is decreased. Recent work by Ettenberg and Kressel[20] has shown that, in accordance with the above arguments, efficient *incoherent* radiation into a narrow fan (of 24° FWHM perpendicular to the junction plane) can be achieved using a "strong" double heterojunction structure with a slab width of $t \approx 0.065\ \mu m$. Their measured beam profile fits that predicted for this case by Dumke[19] for a slab thickness of 0.045, as shown in Fig. 2. The agreement is reasonable. (An "obliquity factor",[21] $1 + \cos\theta$, has been included in the calculated curve of Fig. 2.)

To illustrate the effects of the heterojunction structure on increasing the coupling of the recombining electrons to the radiation field, the enhancement term

$$\frac{\lambda_0{}^2 c}{8\pi^2 n_2{}^3} \cdot \frac{\beta}{t_{eff}} \cdot \frac{d\beta}{d\nu} \qquad [20]$$

has been plotted in Fig. 3 for the fundamental TE mode. "Strong" heterojunctions have been assumed. It is seen that the emission into this single type of guided mode can be more than 0.6 times as efficient as into *all* unguided modes. Moreover, there is a much greater transmission probability at the air-semiconductor interface for the guided than the unguided emission. Coupled with the fact that the very similar fundamental TM mode always coexists with this TE mode, it is clear that the observed far-field emission pattern from a

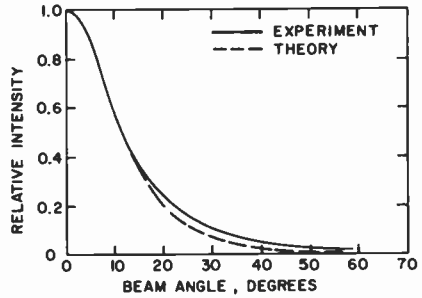

Figure 2—Experimental and theoretical far-field patterns for a double-heterojunction LED. $\Delta n = 0.3$ across the heterojunctions. The measured slab thickness was ~0.065 μm; the theory is for a slab thickness $t = 0.045$ μm.

thin "single-mode" double-heterojunction LED can be dominated by the enhanced radiation into these fundamental modes.

Lossless Single-Mode Microwave Guide

The effect of a field-confining structure is not always that of *increasing* the spontaneous emission rate; it can also depress it. To see this,

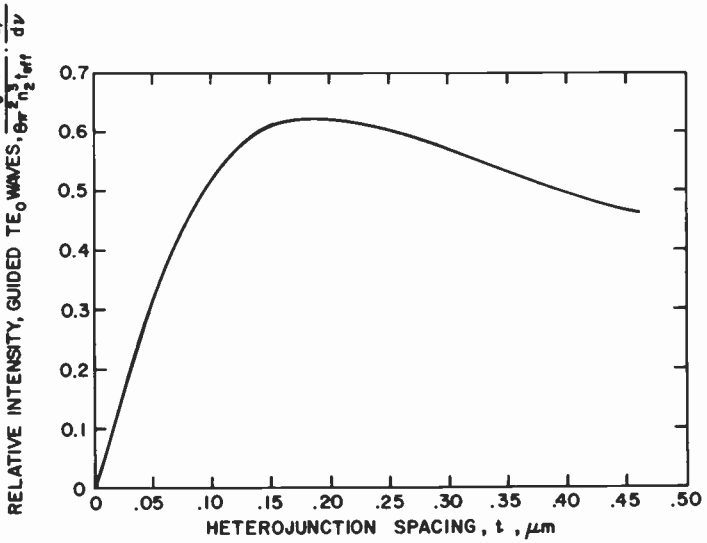

Fig. 3—Ratio of the spontaneous emission probability into the fundamental TE modes to that into all the unguided modes, for a double-heterojunction structure with $n_1 = 3.6$, $n_2 = 3.3$, and $\lambda = 890$ nm.

consider the radiation from an electron spin in a strong magnetic field at microwave frequencies. If the radiating electron is placed in a (lossless, infinite) fundamental-mode (TE_{10}) waveguide, the spontaneous emission rate can be computed as above, by considering the two factors $\langle f|H_1|i\rangle$ and $\rho(\nu)$. For the free-space case (cubical box with periodic boundary conditions), we again have

$$|\langle f|H_1|i\rangle|_{fs}^2 = \frac{B'}{L^3}$$

and

$$\rho_{fs}(\nu) = \frac{8\pi\nu^2}{c^3} \cdot L^3. \qquad [21]$$

For the case of the waveguide, of width a and height b, with periodic boundary conditions on a length L of guide, the corresponding terms are

$$|\langle f|H_1|i\rangle|_g^2 = \frac{2B'}{abL}$$

and

$$\rho_g(\nu) = \frac{2L}{c\sqrt{1 - \left(\frac{\lambda_0}{2a}\right)^2}}. \qquad [22]$$

This leads to a ratio of spontaneous emission rates, with and in the absence of the guide, of

$$\frac{w_g}{w_{fs}} = \frac{\lambda_0^2}{2\pi ab\sqrt{1 - \left(\frac{\lambda_0}{2a}\right)^2}}. \qquad [23]$$

For a "typical" set of parameters at X band, $\lambda_0 = 3$ cm, $a = 2.29$ cm, $b = 1.02$ cm, and $w_g/w_{fs} = 0.81$; the (lossless) waveguide has somewhat suppressed the spontaneous emission rate. Here, the enhanced coupling of the radiation field to the electron (the increased matrix element) is more than compensated by reducing (to two) the number of modes into which the electron can radiate. However, if the guide is operated closer to cut-off, by either decreasing its width a or by increasing the radiation wavelength (by increasing the magnetic field), or with a reduced mode volume, obtained by reducing b (or a), the spontaneous emission rate can be enhanced rather than suppressed.

Acknowledgment

I wish to thank J. Blanc for bringing the literature on chelate fluorescence in the presence of mirrors to my attention.

Appendix

The basic point being made can perhaps be clarified by a somewhat different approach. In calculating the absorption of radiation by an electron (in the absence of saturation), the absorbed power, and hence the induced absorption rate, is proportional to the incident energy density. By confining the field spatially to the vicinity of the electron, the absorption rate, for a given incident power level, can be enhanced. In the case of stimulated emission, the emission rate can be similarly increased. Indeed, the stimulated emission process is the exact dual of the absorption one.

If the radiation field is described quantum mechanically, the absorption rate (for an unexcited electron) is given by an expression of the form[16]

$$w_{abs} = A \cdot n_i, \qquad [24]$$

where n_i is the number of photons in the radiation field. Similarly, a calculation of the emission from the same electron when in its upper state is[22]

$$w_{em} = A(n_i + 1). \qquad [25]$$

Here n_i is again the number of photons in the radiation field, and the term "1" represents the effects of spontaneous emission. Thus, spontaneous emission can be thought of as a process equivalent in its effects to that of induced emission with only one photon in the field (mode).

The important point to note here is that the effect of a field-influencing structure manifests itself in the matrix element-containing term A, which is the *same* for both absorption and emission. The introduction of a structure that alters the absorption (or *stimulated* emission) rate not only can, but *must*, alter the spontaneous emission into the relevant field mode in *identically* the same way.

References:

[1] E. M. Purcell, "Spontaneous Emission Probabilities at Radio Frequencies," *Phys. Rev.*, **69**, p. 681 (1946).

[2] K. H. Drexhage, "Optische Untersuchungen an Neuartigen Monomolekularen Farbstoffschichten," (Habilitations-Schrift), Marburg, 1966 (unpublished).

[3] See, e.g., H. Morawitz, "Self-Coupling of a Two-Level System by a Mirror," *Phys. Rev.*, **187**, p. 1792 (1969); H. Kuhn, "Classical Aspects of Energy Transfer in Molecular Systems," *J. Chem. Phys.*, **53**, p. 101 (1970).

[4] P. Stehle, "Atomic Radiation in a Cavity," *Phys. Rev.*, **A2**, p. 102 (1970); M. R. Philpott, "Fluorescence from Molecules Between Mirrors," *Chem. Phys. Lett.*, **19**, p. 435 (1973); P. W. Milonni and P. L. Knight, "Spontaneous Emission Between Mirrors," *Opt. Comm.*, **9**, p. 119 (1973); R. R. Chance, A. H. Miller, A. Prock, and R. Silbey, "Fluorescence and Energy Transfer Near Interfaces: The Complete and Quantitative Description of the Eu^{+3}/Mirror Systems," *J. Chem. Phys.*, **63**, p. 1589 (1975).

[5] See, e.g., A. L. Schawlow and C. H. Townes, "Infrared and Optical Masers," *Phys. Rev.*, **112**, p. 1940 (1958); D. A. Kleinman, "The Maser Rate Equations and Spiking," *Bell Syst. Tech. J.*, **43**, p. 1505 (1964); D. E. McCumber, "Intensity Fluctuations in the Output of CW Laser Oscillators, I.," *Phys. Rev.*, **141**, p. 306 (1966).

[6] W. H. Louisell, *Radiation and Noise in Quantum Mechanics*, McGraw-Hill Book Co., N.Y., 1964, Sect. 5.3.

[7] H. Kressel and M. Ettenberg, "A New Edge-Emitting (AlGa)As Heterojunction LED for Fiber-Optic Communications," *Proc. IEEE*, **63**, p. 1360 (1975).

[8] R. E. Collin, *Field Theory of Guided Waves*," McGraw-Hill Book Co., N.Y., 1960, Sect. 11.5.

[9] See Ref. [6], Sect. 4.6.

[10] J. E. Goell and R. D. Standley, "Integrated Optical Circuits," *Proc. IEEE*, **58**, p. 1504 (1970).

[11] W. W. Anderson, "Mode Confinement and Gain in Junction Lasers," *IEEE J. Quant. Elect.*, **QE-1**, p. 228 (1965).

[12] G. Lasher and F. Stern, "Spontaneous and Stimulated Recombination Radiation in Semiconductors," *Phys. Rev.*, **133**, p. A553 (1964).

[13] See Ref. [6], Sect. 4.4.

[14] P. K. Tien, "Light Waves in Thin Films and Integrated Optics," *Appl. Opt.*, **10**, p. 2395 (1971).

[15] D. Marcuse, *Light Transmission Optics*, Van Nostrand Reinhold Co., N.Y., 1972, Sect. 8.3.

[16] See Ref. [6], Sect. 5.4.

[17] H. F. Lockwood, J. P. Wittke, and M. Ettenberg, "LED for High Data Rate Optical Communications," to be published.

[18] H. Kressel, J. K. Butler, F. Z. Hawrylo, H. F. Lockwood, and M. Ettenberg, "Mode Guiding in Symmetrical (AlGa)As-GaAs Heterojunction Lasers With Very Narrow Active Regions," *RCA Review*, **32**, p. 393 (1971).

[19] W. P. Dumke, "The Angular Beam Divergence in Double-Heterojunction Lasers with Very Thin Active Regions," *IEEE J. Quant. Elect.*, **QE-11**, p. 400 (1975).

[20] M. Ettenberg and H. Kressel, to be published.

[21] See Ref. [15], Sect. 2.2; L. Lewin, "Obliquity Factor for Radiation from Solid-State Laser," *Elect. Letters*, **10**, p. 134 (1974).

[22] See Ref. [6], Sect. 5.5.

The Physics of Electrical Charging and Discharging of Semiconductors

H. Kiess

Laboratories RCA Ltd., Zurich, Switzerland

Abstract—The technical applications that utilize the electrical energy stored in electrodeless thin insulating and/or photoconducting materials are quite numerous. The different applications make use of different properties of the materials. However, certain aspects of the electrical charging and discharging processes are common to all applications. These processes are reviewed; in particular, models are discussed for the charge storage and the dissipation of the charge in the dark and under illumination. These are then compared with experimental results obtained with different materials.

1. Introduction

Charge storage in dielectrics can be both desirable and undesirable. The accumulation of charge on highly insulating plastic materials can be undesirable in that it can present problems in production and in certain applications. On the other hand, if electrostatic charges can be stored permanently or for limited times on insulators and removed at will in a controlled manner, a variety of practical applications emerge. Such applications include electret microphones, prosthetic devices wherein electrified polymers prevent the clotting of blood, the vidicon pickup tube for television, and photoreceptors and toners used in the electrophotographic process.

The different applications place different requirements on the dielectric. This is reflected by the fact that the materials used for the different applications range from inorganic semiconductors and insu-

lators to organic photoconducting and highly insulating polymers. Certain common features of the charge storage and the discharge mechanism are discussed here, with emphasis on the behavior of semiconducting and photoconductive dielectrics. Due to their importance in technology, photoconductors have been extensively investigated, and our knowledge of these materials serves as the basis for this paper, namely, to review physical processes of the charging and discharging mechanisms and to illustrate the usefulness and the deficiency of these concepts when tested experimentally. The second section discusses the different charging methods. The stationary current–voltage characteristics of insulators and photoconductors are discussed in the third section, since they give useful insight into the physical processes occurring during the discharge. The discharge models and theoretical approaches to calculation of discharge curves are summarized in Section 4, where emphasis is placed more on elaborating the differences of the various approaches than in giving a complete account of all formally possible discharge curves. In Section 5, experimental results are discussed, and Section 6 is a status summary.

2. Charging Methods

In most technical applications the dielectric is supplied with a conducting contact on only one side; charge is deposited on the opposite side. In the charged state, this surface is at a potential V_S with respect to the usually grounded conducting contact. V_S is given by

$$V_S = \frac{Q_s}{C}, \qquad [1]$$

where Q_s is the charge and C is the capacitance. The capacitance is, in general, a function of the surface voltage, depending on where the charge is stored. In principle, three different situations for the location of the stored charge may arise. First, the charge may be located close to or at the surface; second, the charges may penetrate into the solid and form a space charge; and third, a polarization of the material or a displacement of the ions on a microscopic or macroscopic scale may occur, giving rise to the so-called heterocharges. However, the mode of charge storage is not solely a question of the property of the dielectric but also a function of the details of the charging process and of the methods used.

A number of methods for charging dielectric materials are described in the literature. These are (1) charging with an electron or ion beam, (2) the use of a corona or Townsend discharge, (3) applying

fields up to and exceeding the breakdown strength of the dielectric, and (4) touching or rubbing the dielectric with another dielectric material or a metal. While these techniques are all relatively easy to implement, the choice of technique depends on the control that is desired over the charge density, the lateral charge distribution, and the spatial charge depth.

2.1 Electron-Beam Charging

The simplest widely used charging process is probably charging the dielectric with a low-energy electron beam. Electrons impinging on a solid and having a kinetic energy of a few eV or only thermal energy in vacuum will acquire an additional energy in passing through the vacuum–solid interface. The difference in kinetic energy is

$$-\frac{1}{2} m v_{\text{vacuum}}^2 + \frac{1}{2} m_{\text{eff}} v_{\text{solid}}^2 = E_{\text{kin}} = (\varphi - \zeta), \qquad [2]$$

where φ is the work function of the solid, ζ is the separation of the Fermi level from the bottom of the conduction band (Fig. 1), m is the

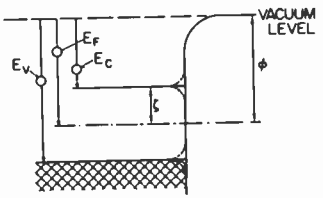

Fig. 1—Energy-band scheme.

electron mass, and v is the velocity of the electron. These electrons will thermalize in the solid, dissipating their energy by emission of phonons and impact ionization across the bandgap if the kinetic energy of the electrons is larger than the energy of the forbidden gap. How far they penetrate into the solid depends on the mean free path of hot electrons under the action of different dissipating processes. Assuming that the energy of the electrons is well above the threshold energy for pair production, it is to be expected that the mean free path length due to phonon emission is large compared to that due to impact ionization. An estimate for electrons having a kinetic energy of 5 eV in a semiconductor of 1 eV bandgap yields[1] a mean free path for phonon emission of the order several hundred Å, and for pair production only a few Å. We therefore conclude that the stopping power

for low-energy electrons is so strong that they can be considered to have thermalized within several hundred Å below the surface.

If the energy of the impinging electrons is higher, the electrons will also interact with deeper-lying bands (Fig. 2). If we denote the bands in the solid by A, B . . ., then a primary electron having lost the energy V_0 because of its interaction with an electron of the band D, will either be reflected back and leave the target (the less probable process) or undergo further such losses. The vacancy created in the D-band will be refilled by an electron from one of the higher bands. Usually the Auger process accounts for the dissipation of the energy.[2,3] The details of such a process are shown on the right side of Fig. 2. Two electrons take part in an Auger process. The first electron,

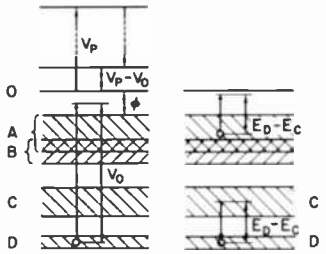

Fig. 2—Schematic energy-band scheme of a metal. On the left, a primary electron suffers a discrete energy loss. On the right, the vacancy in band D is refilled, and the energy released causes the excitation of an electron by Auger effect (After G. A. Harrower).

originally in band C, drops to fill the vacancy in band D. The energy $E_D - E_C$ released in this process is given to a second electron in band B, which is then excited into the conduction band. The penetration depth of primary electrons with energies of several hundred or thousand eV is, of course, greater than that of low-energy electrons, even though the energy dissipating processes are very efficient. Experimentally determined values of the penetration depth are of the order of 1 μm for 20 keV primary electrons in Teflon.[4] A general relationship between the energy of the impinging electrons and the density of the material is given by Bichsel.[5] Irrespective of the energy of the primary electrons, the effect of the electron beam is twofold: (1) the electron beam acts as an electron-injecting contact to the dielectric and (2) secondary processes increase the conductivity during the charging process within the range of the penetration depth of the primary electrons. In order to obtain permanent charge storage, the

electrons have to be immobilized by capture in traps located close to the surface or in the bulk.

2.2 Ion-Beam Charging

The phenomena occurring in ion interactions with metal surfaces have received a great deal of emphasis,[6] whereas the ion–insulator problem has been largely neglected. Only recently have studies of the ion bombardment of insulators been carried out, leading to some understanding of the interaction process. The neglect of the ion–insulator process can be attributed to experimental difficulties, especially to the accumulation of charge, which changes the conditions during the course of the experiment and causes difficulties in the interpretation of the results. To circumvent this problem, very thin samples and/or elevated temperatures were used to study the interaction.[7] Recently, Vance[8] published an investigation that did not allow a continuous discharge of a sample surface but rather allowed the accumulation of charge. His results obtained with amorphous Se can be explained within the framework of the existing model of positive ion–insulator interaction. He used also an analogous model to explain observations with negative ions.

Let us first consider positive ions and cases where the impinging ions have sufficiently low velocity that direct kinetic effects play a minor role, i.e., that the ions are neutralized before penetrating the solid. There are then three processes to consider: (1) radiative neutralization, (2) resonance neutralization with Auger de-excitation, and (3) Auger neutralization of the incoming ion. The initial state lifetime of the radiative process is of the order of 10^{-8} sec; that of the other two processes[9] is about 10^{-14} sec. For this reason the neutralization of the ion will take place either through resonance neutralization followed by Auger de-excitation or through Auger neutralization (Fig. 3). The resonance neutralization at a surface of a solid occurs by tunneling of an electron from the solid to the ion; the electron then populates an excited level. The neutralization of the ion is followed by an Auger de-excitation step; an electron of the solid goes to the vacant ground level and the released energy is imparted to an electron of the solid or to the electron in the excited level. In the Auger-neutralization process, it is assumed that the ion is directly neutralized by an electron transition from the solid to the ground state of the atom. The energy released excites an electron in the solid. The kinetic energy still inherent in the neutralized ion is dissipated in the solid by inelastic scattering, excitation of phonons and electrons, and, at sufficiently high energy, by displacement of atoms. According to their

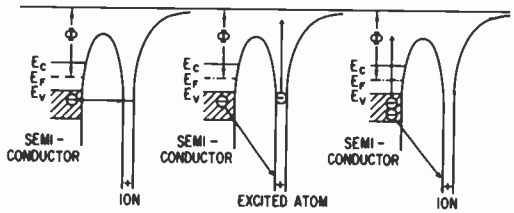

Fig. 3—Resonance neutralization, Auger de-excitation and Auger neutralization process in schematic representation (after Hagstrom).

lifetimes the Auger and resonance neutralization processes are competing in principle. In practice, however, it turns out that the Auger neutralization is more important.[10]

The gross features of the positive-ion-beam technique for charging a dielectric are similar to those of the electron-beam technique: electrons are injected into the solid with an electron beam, while holes are injected into the dielectric through the ion–solid interaction. The carrier density close to the surface is similarly increased due to secondary effects during irradiation with the ion beam. In order to obtain permanent charge, deep hole trapping centers must be assumed in which the holes can be trapped before being transported to the grounded electrode.

The interaction of solids with slow negative ions has been investigated even less than has the positive-ion–dielectric interaction. The only publication that gives experimental results is that of Vance,[8] who bombarded amorphous Se layers with O^- ions having a kinetic energy of 50 eV or more. The results were explained by a model similar to the one used to explain the positive-ion–solid interaction. The energy-level diagram is shown in Fig. 4. Any change of potential energy of the ion due to image force is neglected. The electron is bound to the incoming ion with an energy E_{EA}, the electron affinity. Upon approaching the surface the electron is transferred from the ion to the dielectric by resonance neutralization. The maximum energy released

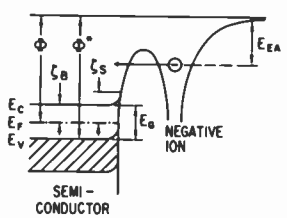

Fig. 4—Resonance neutralization for a negative ion (after Vance).

Table 1—Electron Affinities of Different Ions

Species	Electron affinity E_{EA}
O	1.5 eV
O_2	.45 eV
O_3	3.24 eV
CO_3	3–4 eV
NO_2	4 eV
NO	.025eV
Cl	3.82 eV
OH	1.83 eV

is given by

$$E_{max} = \varphi^* - (E_G - \zeta_s) - E_{EA} = \varphi - E_{EA}, \qquad [3]$$

where φ^* is the separation of the valence band from the vacuum level (the threshold energy for photoemission), E_G is the bandgap of the dielectric, ζ_s is the separation of the Fermi level from the conduction band at the surface, and E_{EA} is the electron affinity of the incoming atom or molecule. E_{max} is usually small compared to the energy released in the case of positive ions. For dielectrics with a large bandgap, this energy is often smaller than the forbidden gap (Tables 1 and 2). The cascading of the electron into the lowest state of energy will therefore be accompanied by phonon emission only, so that no additional temporary increase in conductivity by impact ionization across the bandgap is to be expected. Carrier generation by the neutralized ion penetrating the solid and dissipating its kinetic energy seems also to be negligible. In this case also, in order to retain the charge, the injected electron must be immobilized in a trap. In contrast to electron-beam and positive-ion-beam charging, secondary effects are not expected to give rise to a temporary increase of the conductivity during charging.

Table 2—Bandgaps, Workfunction, and ζ_s of Some II–VI Compounds in UHV[62] and of Se

Compound	Band gap E_G (eV)	Workfunction ϕ(eV)	ζ_s (eV)	ζ_{bulk} (eV)
ZnO	3.6	4.68	.11	.10
CdS	2.4	5.01	.22	.15
CdSe	1.74	5.22	.27	.15
ZnSe	2.6	4.84	.73	.15
Se	1.9	4.9		

2.3 Charging With a Corona Discharge or Townsend Discharge

These two techniques of charging dielectrics are closely related to the ion-beam charging. However, there are two differences: (1) they are used at high pressures of the ambient atmosphere so that gas–solid reactions may take place at the surface, and (2) the kinetic energy of the ions is close to thermal energy in front of the dielectric which is to be charged. The possibility of using corona or Townsend discharge at high gas pressure makes it a truly practical charging method.

The first question to be answered is which ionic species are generated in a corona discharge. Shahin[11–13] has performed mass spectrometric studies of positive and negative corona discharges in air, nitrogen, and oxygen at atmospheric and lower pressures. The ionic species he found in a positive corona discharge in air of 20% humidity at room temperature are mainly clusters of ions of the type $H^+(H_2O)_n$. Probably the mechanisms by which $H^+(H_2O)_n$ clusters are formed are either charge exchange reactions of the primary ion N_2^+ and O_2^+ etc. with water molecules such as

$$N_2^+ + H_2O \rightarrow H_2O^+ + N_2 \qquad [4]$$

and the subsequent reaction $H_2O^+ + H_2O \rightarrow H_3O^+ + OH$, or the production of hydride by a reaction

$$N_2^+ + H_2O \rightarrow N_2H^+ + OH. \qquad [5]$$

In a subsequent collision of the hydride with a water molecule, the cluster forms

$$N_2H^+ + H_2O \rightarrow H_3O^+ + N_2. \qquad [6]$$

It was found that the clusters are formed even if only traces of water are present in the ambient. A theory developed by Moran and Hamill[14,15] indicates that a partial pressure of the water of 10^{-6} Torr in a gas at atmospheric pressure is quite enough to form hydrate ions within 70 msec.

The ions produced in a negative corona discharge are not dominated by hydrated species. At one atmospheric pressure of air or oxygen, CO_3^- ions appear to give the main contribution to the ions formed in the discharge.[11] The primary ionic species are O^- ions generated by dissociative electron attachment. Subsequent reactions of the O^- ions with O_2 forms O_3^-,

$$O^- + O_2 + M \rightarrow O_3^- + M, \qquad [7]$$

and with CO_2 it forms CO_3^-,

$$O^- + CO_2 + M \rightarrow CO_3^- + M, \quad [8]$$

where M is a third body (N_2, O_2) necessary to stabilize the reaction product by removing the excess energy. A further reaction between O_3^- and CO_2 leads to an enhancement of the CO_3^- yield;

$$O_3^- + CO_2 \rightarrow CO_3^- + O_2. \quad [9]$$

Trace amounts of CO_2 seem also here to be sufficient to cause an over-whelming contribution of the CO_3^- ions to the ionic species formed. If the pressure is reduced to 100 Torr or lower, the CO_3^- ion is present only in traces, and the dominant ionic species found are now O_3^- ions.

The charging process of a dielectric with positive ions should occur in full analogy to the processes outlined in the previous section on ion-beam charging: injection of holes through Auger and/or resonance neutralization processes with subsequent capture of the holes in trapping centers.

The charging with negative ions for other materials may be different from the process outlined by Vance for Se in which resonance neutralization of the ion in front of the dielectric with simultaneous injection of electrons was postulated. That this process does not hold for all materials is evidenced in the case of ZnO single crystals; ZnO single crystals can be charged negatively by a corona discharge in air, oxygen, or carbon dioxide, but cannot be charged by a corona discharge in argon, where free electrons of thermal energy are produced, nor with an electron beam directly in vacuum. To account for the latter observation, we have to assume that no significant trapping of electrons occurs at the surface and that the injected electrons are transported easily through the material. To account for the chargeability in air, oxygen, or CO_2 atmosphere we must conclude that the ions do not lose their electron by resonance transfer process.

Neglecting other processes, resonance neutralization should not occur if the electron affinity of the involved molecular species is greater than the electron affinity of the solid, i.e., the energy separation between the bottom of the conduction band and the vacuum level (Fig. 4). Since the electron affinity of the ions produced in the corona discharge is at least 0.5 eV smaller than that of ZnO (see Tables 1 and 2), we must assume that other processes prevent a resonance transfer and hence an injection of the electrons into the conduction band of ZnO, so that it becomes electrically chargeable. It is to be expected that image force attraction causes a lowering of the energy level of the ion by about 0.5 eV at a distance of the order of 1 Å,[16,17] but this effect is not sufficient to explain the chargeability of

ZnO. This has been shown by charging experiments at low pressures; according to Shahin the predominant ionic species produced at low pressures is O_3^-, an ion having an electron affinity about 1 eV smaller than that of CO_3^-. If image force attraction were to account for the chargeability of ZnO with CO_3^- ions, charging with O_3^- would not be possible, since energy considerations show that then resonance transfer would be allowed and hence charging impossible. Experimentally the opposite is found; neither surface voltage nor the dark decay of the charge are affected.[18] These results indicate that the limitations to charging are of a different nature, e.g., that reactions of the ionic species take place at the surface of the ZnO,

$$O_3^- \rightarrow O_2 + O^-_{\text{adsorbed}} \text{ or } CO_3^- \rightarrow CO_2 + O^-_{\text{adsorbed}},$$

which give rise to the same surface states. No detailed investigations of this problem were made.

Aside from ionic species there is also ozone generated in a corona discharge in air or oxygen, especially in a negative corona discharge. Evidence was presented that O_3 reacts with the solid to form a charge-transfer complex of the type O_3^-·solid$^+$ with photoconducting organic solids such as poly-n-vinyl carbazole (PVK) or others.[19] The formation of this complex is equivalent to a transfer of a valence band electron of the solid to the adsorbed O_3; hence it is equivalent to the injection of a hole. This process was assumed to hold since exposure of positively charged surfaces to ozone discharged PVK layers in the same way that light does. The model for charging dielectrics positively assumes also the injection of a hole which is rapidly trapped. The question remains as to why a hole injected from O_3 should behave differently from holes injected from positive ions. It might be only an apparent contradiction insofar as the charging efficiency for these dielectrics may be low, i.e., that only a small fraction of the injected holes are trapped and contribute to the charge on or in the solid.

2.4 Contact and Triboelectrification

Contact or frictional electrification is not commonly used as a method to charge dielectrics, since there is virtually no control over the amount of the transferred charge. The physics involved is so complex that many mechanisms have been proposed to explain the charge transfer from a metal or from a dielectric to a dielectric. There are ion

migration,[20] electron transfer by tunneling,[21] mechanical transfer,[22] and transfer by thermal gradients. In comparing experimental results one must be careful because different experimental conditions often evoke different disturbing errors, such as breakdown of the air, badly defined contact areas, and surface conductivity, all of which influence the amount of transferred charge.

The concept of electron transfer by tunneling to explain contact electrification has been advanced by Bauser et al.[23] and by Davies.[24] The exchange of charge across the interface between a metal and a semiconductor is indeed a very well accepted concept in solid-state physics. The basic idea is that the Fermi levels of the metal and the semiconductor reach thermal equilibrium. For highly insulating materials the Fermi level is not very well defined, since nonequilibrium states may be frozen in. Therefore the exchange of charges between a metal and a dielectric certainly depends on the accidental occupation of the surface states and is only loosely connected with the bulk properties. It has been found that the amount and the sign of the charge transferred is closely related to the work function of the metal in contact with the dielectric. Nevertheless it is not appropriate to deduce a work function for the dielectric from such measurements.

The concept of work function was also used to explain the charge transfer from dielectric to dielectric. The transfer was assumed to be due to tunneling of electrons from one surface to the other, the direction of transfer being governed by the work functions of the different materials. Ruckdeschel,[25] however, claimed recently that his experimental data are only explicable if he assumes an ion exchange across the interface. His conclusions were corroborated by the fact that in vacuum and dry atmosphere no charge transfer was observed. This lead him to state that the ions transferred are most likely protons.

Similarly, the mechanism to explain frictional electrification is still a matter of controversy. Wählin et al.[26] claimed in a recent paper that for frictional electrification the electron-transfer model applies. Kornfeld[22] explained his results by mechanical transfer—the solids are assumed to have structural and chemical defects leading to electrical depletion or accummulation layers at the surface which are neutral to the outside world. Friction between one material and the other mixes the surface layers and redistributes the charges between the materials rubbed. Recent measurements by Pepper[27] have shown that, indeed, material transfer between metals and polymers is observed. The disturbance of the compensation of the "intrinsic" charges then gives rise to the electrification of the materials. It seems that at the present state of the art neither process can be excluded or made solely responsible for the frictional electrification.

3. Current–Voltage Characteristics

In order to separate the physical mechanisms governing the dissipation of the charge it is necessary to study the transport and trapping of the charge carriers in the dielectrics. These studies may be done using different techniques: first, by measuring the I-V characteristics during the charging process; second, by measuring the surface voltage with time at constant temperature or by increasing the temperature; and third, by simulating the charged state with blocking contacts and measuring the current as a function of time at different voltages.

The first method requires control of the surface voltage of the dielectric and measurement of the current through the dielectric during charging. The advantages are obvious—the models for I-V characteristics are rather well established and therefore the comparison of experimental results and theory is facilitated.

The second method usually implies a more difficult theoretical analysis, since time-dependent equations for the carrier transport must be solved. Since the surface voltage, rather than the dissipation of the surface charge itself, is measured as a function of time, problems do exist in obtaining the charge as a function of time, which is the quantity of interest.

The third method gives a means of investigating certain aspects of the carrier transport or trapping of charge carriers separately and of studying time-dependent phenomena under well-controlled conditions. Although it represents an important tool for obtaining relevant parameters governing the discharge of dielectrics, a detailed explanation would be too lengthy for the present discussion.

3.1 Models for the Carrier Transport in Dielectrics With Injecting Contacts

If charge storage is to occur in a homogeneous dielectric with injecting contacts, then the trap density and the trap depth must be such as to retain sufficient charge for a desired period of time.* The equations governing the carrier transport are the continuity equation for the free charge carriers and Poisson's equation. In the steady state, assuming a one-dimensional problem and that only electrons contribute to the current, we obtain from div $j = 0$,

$$j = e\mu_n n\mathbf{E} + eD\frac{dn}{dx}, \qquad [10]$$

where j is the current density, μ_n is the mobility of the electrons, n is

* An injecting contact is defined as a contact with an electron concentration greater than the electron density of the bulk material.

the electron density, **E** is the electric field, D is the diffusion constant, and e is the elementary charge. Poisson's equation gives

$$\frac{d\mathbf{E}}{dx} = \frac{1}{\epsilon\epsilon_0}\rho(x), \qquad [11]$$

where ρ is the space-charge density and ϵ is the dielectric constant.

In addition to Eqs. [10] and [11], a relationship between the space-charge density ρ and the free-electron density exists which depends on the details of the trap distribution in the forbidden gap and on the position of the Fermi level before applying a voltage. In principle ρ can be expressed as a function of the electron density so that

$$\rho = f(n). \qquad [12]$$

If the diffusion current in Eq. [10] is neglected,† Eqs. [10] through [12] can be solved. In the case of an electron-injecting contact the solutions have been discussed at length[28,29] and lead to the well-known space-charge-limited currents. The I-V characteristics of a solid with a trap of well-defined energy are shown schematically in Fig. 5, and analytical results for solids with different trap distributions are sum-

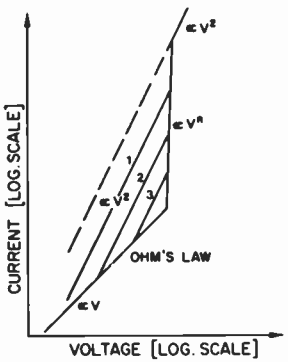

Fig. 5—Schematic representation of the I-V characteristics of an insulator with ohmic contacts. Density of traps is N_t, the trap depth increases from 1 to 3. The dotted line represents the trap-free case.

marized in Table 3. In essence the increase of current density with voltage with a power law equal or greater than two is due to an increase of the number of electrons in the solid, which is, for a given geometry, solely a function of voltage. Since only the free electrons enter the expression for the current density, j is smaller for a solid

† A detailed discussion of the conditions under which diffusion currents can be neglected and how diffusion changes the analytical form of the I-V characteristics is given by F. Stöckmann[28] and M. A. Lampert,[29] respectively.

Table 3—I-V Characteristics

Different current regimes ← increasing voltage →

	Shallow trap of energy E	Deep trap of energy E_d	Deep traps exponentially distributed in energy $N_t = N_{t_0} \exp\left\{-\frac{E}{kT_c}\right\}$
Ohms law	$j = e\mu n \frac{V}{L}$	$j = e\mu n \frac{V}{L}$	$j = e\mu n \frac{V}{L}$
Space charge limitation	$j = \frac{9}{8}\Theta\epsilon\epsilon_0\mu\frac{V^2}{L^3}$ $\Theta = \frac{n}{N_{tn}}$		$j = e\mu N_c\left(\frac{\epsilon\epsilon_0}{ekT_cN_t}\right)^{T/T_c}\cdot\frac{V(T_c/T)+1}{L(2T_c/T)+1}$
Trap filled limit	$j = \frac{2}{3}e\mu K\frac{V_H^2}{L(V_H - V)}$; $V < V_H$ $j = \frac{e\mu N_t}{L}\cdot\frac{V - V_H}{\ln\frac{2V_H}{V - V_H}}$; $V > V_H$ $K = N_c \exp\left\{\frac{E - E_c}{kT}\right\}$, N_t = trap density	$j = \frac{2}{3}e\mu K\frac{V_H^2}{L(V_H - V)}$ $j = \frac{e\mu N_t}{L}\cdot\frac{V - V_H}{\ln\frac{2V_H}{V - V_H}}$	
Space charge limitation no traps	$j = \frac{9}{8}\epsilon\epsilon_0\mu\frac{V^2}{L^3}$	$j = \frac{9}{8}\epsilon\epsilon_0\mu\frac{V^2}{L^3}$	

with traps where electrons get immobilized than for a trap-free solid. In fact, the position of the traps with respect to the Fermi level and the trap distribution determine the ratio of free carriers to total injected carriers giving rise to different voltage dependences of the current. (Eqs. [10] through [12] would have to be modified to include also the transport of holes whenever the anode injects holes. However, double-injection phenomena are irrelevant in this context.)

The considerations so far are valid for a homogeneous dielectric. In practice it is often found that the trap densities at or close to the surface are much higher than in the bulk so that the carriers injected by the charging process are strongly trapped close to the surface. This desirable feature of a dielectric is discussed in Section 2. The drift length of the charge carriers, i.e., the product $\mu\tau\mathbf{E}$, (μ is the mobility, τ is the lifetime, and $\mathbf{E}$ is the electric-field), is then much smaller in the surface region than in the bulk. This configuration is especially desired when the stored charge is to be modulated by light and, therefore, good transport properties of the bulk of the material are required such as in vidicons and in electrophotographic plates. There, the discharge by light should be fast and should not suffer from recombination losses or from the retention of charge carriers in traps. Under this condition, it is useful to describe the I-V characteristics in terms of a two-layer model, i.e., a thin surface layer (beam-blocking region) with high concentration of deep traps adjacent to the bulk of the photoconductor, which ideally would be trap free. An energy-band diagram for such a model proposed by Goodman[30] is shown in

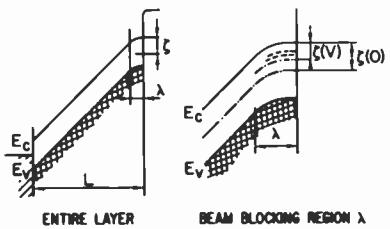

Fig. 6—Energy-band diagram with beam blocking region (after Goodman).

Fig. 6. The depth of the Fermi level in the surface layer is a function of voltage. When $V = 0$, the net charge in this layer is zero. For non-zero voltage, the surface layer becomes charged due to the filling of deep electron trap levels. In the steady state the incoming electrons are partially transmitted through this layer, partially thermalized, trapped, re-emitted thermally, and drifted through the layer.

If the current due to the drifting electrons through the beam-blocking regions (b.b.r.) is larger than that due to the transmitted electron, the b.b.r. acts as an injecting contact. In these conditions three voltage regimes of the I-V characteristic must be distinguished; at low voltages the current through the bulk is space-charge limited. The I-V characteristic is then given by

$$I = \frac{9}{8} \epsilon\epsilon_0 \mu\theta \frac{V^2}{L^3}, \qquad [13]$$

where V is the voltage across the bulk, and L is the thickness of the dielectric without b.b.r. At increasing voltage, the b.b.r. can no longer supply the current prescribed by the space-charge-limited current. Therefore the field will become practically uniform in the bulk and the I-V characteristic linear. This regime represents a transition region between the SCLC-regime and the high-voltage regime in which the current is limited by the supply of carriers from the b.b.r. Since the electron density in the b.b.r. and also at the interface between b.b.r. and the bulk is given by the position of the quasi Fermi level ζ_n, the electron concentration is

$$n \propto \exp\left\{-\frac{e\zeta_n(V)}{kT}\right\} \qquad [14]$$

The unilateral thermally generated current density into the bulk, representing the highest possible current, is then

$$I_s = \frac{env}{4} = eN_c \left(\frac{kT}{2\pi m_{eff}}\right)^{1/2} \exp\left\{-\frac{e\zeta_n(V)}{T}\right\} \qquad [15]$$

or, if $\zeta_n(V)$ is developed into a power series,

$$I_s = eN_c \left(\frac{kT}{2\pi m_{eff}}\right)^{1/2} \exp\left\{-\frac{e\zeta_n(0)}{kT}\right\} \exp\left\{\frac{e}{kT}\left(\frac{d\zeta_n}{dV}\right)_0 V\right\}.$$

$\zeta_n(V)$ depends on the detailed nature of the trap distribution in the forbidden gap of the b.b.r. With increasing voltage, the occupancy of the traps will be increased, shifting the Fermi level towards the conduction band and thus increasing the current. The I-V characteristic should therefore give information on the trap distribution in the forbidden gap of the b.b.r.

The same model can be applied to explain the photocurrent–voltage characteristics obtained with strongly absorbed light. Within the penetration depth of the light the carrier density is substantially increased over that in the non-illuminated region. Therefore, a surface region of high carrier concentration exists in contrast to the bulk

where the carrier density is low. It was shown[31] that the photocurrent in the low-voltage regime is space-charge limited and can be described by Eq. [13]. At intermediate voltages, the current is given by

$$I_{ph} = \frac{e\dot{N}\tau\mu V}{\lambda L}, \qquad [16]$$

where $\dot{N}$ is the number of incident photons per second per cm^2, λ is the penetration depth of the light, and τ is the recombination lifetime. At high voltages the current saturates;

$$I_{ph} = e\dot{N}. \qquad [17]$$

These formulas indicate that at low voltages in the regime of SCLC flow, the current should be independent of light intensity, whereas at high voltages a linear dependence on light intensity should be observed.

3.2 Models for the Carrier Transport in Dielectrics With Blocking Contacts

(a) General Considerations

Blocking contacts exist in many cases where semiconductors can be charged negatively in a corona discharge. The ions deposited on the free surface prevent the injection of electrons, and a region of carrier depletion forms underneath. The bulk itself forms the back contact and, since an n-type material was assumed, injection of holes from the bulk is prevented.

Though by definition an idealized blocking contact prevents a current flow due to charge carriers of one sign (since the carrier concentration at the contact is assumed to be zero), it allows nevertheless the extraction of internally generated charge carriers of the other sign. In particular, if a contact prevents the transport of electrons across the interface it nevertheless allows the extraction of holes generated, e.g., by light in the bulk. This behavior is illustrated in Fig. 7. Due to the large separation of the Fermi level from the conduction band, the electron concentration at the interface is much smaller than in the bulk. Therefore, the electron transport across the interface is negligible. Under illumination the Fermi level splits into the quasi Fermi levels E_{F_n} and E_{F_p} indicating an increase in carrier concentration in the bulk, but not at the interface due to an assumed infinitely fast recombination rate there. The electron transport across the interface is then still prevented under illumination, whereas the

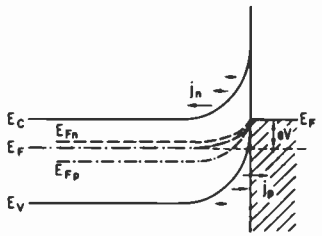

Fig. 7—Energy-band diagram of a blocking contact with applied voltage V. Under illumination, the Fermi level E_F splits into E_{Fn} and E_{Fp}. The arrows indicate the contribution of the electrons and holes to the current at different positions. At the interface the electron current is negligibly small, and the hole current is at its highest.

holes are easily transported across the contact area.* By similar reasoning a hole-blocking contact allows the extraction of internally generated electrons.

If only electrons were generated by the light, e.g., by impurity absorption, then an additional space charge would be formed increasing the field in front of the cathode and reducing it at the anode so that no stationary current would be observable, a result imposed by the current-continuity equation. If a steady-state current is to be observed, the holes must also be mobile. At the cathode the current is carried completely by holes, at the anode exclusively by electrons, whereas in the bulk of the material both carriers contribute to the current. The basic Eqs. [10], [11], and [12] must now include both electrons and holes. The continuity equation $\mathrm{div} j = \mathrm{div}\,(j_n + j_p) = 0$ then gives

$$\frac{dj_n}{dx} = g - R, \qquad [18]$$

$$\frac{dj_p}{dx} = -(g - R), \qquad [19]$$

where g is the generation rate, which includes both the thermal and optical rate of carrier generation and R is the recombination rate. R depends on the details of the recombination mechanism of electrons and holes. The space-charge density in Poisson's equation is now given by

* This consideration neglects photoexcited injection of electrons from the metal into the semiconductor,[32] so that injection currents should also be taken into account. The injection rate is usually small compared to the extraction rate, thereby allowing the simplification.

$$\frac{\epsilon\epsilon_0}{e}\frac{d\mathbf{E}}{dx} = (n + p_t) - (n + n_t) - (p_0 + p_{t0}) - (n_0 + n_{t0}). \quad [20]$$

The index t refers to the density of trapped electrons and holes, and the index 0 to the free and trapped electrons and holes in thermal equilibrium. In addition, equations are required to correlate the trapped and free charge carriers. From reaction kinetics one finds that (at least in principle) the trapped densities can be expressed as a function of the carrier densities if recombination through the trapping states is neglected.

$$n_t = f(n), \; p_t = f(p). \quad [21]$$

Solutions of these equations have been worked out under simplifying assumptions.[33] In the present context is seems preferable to use physical arguments to obtain the I-V characteristics.

(b) Photo-Induced Blocking Contacts

Goodman and Rose[34] considered a model of a photoconductor with blocking contacts. The carriers generated uniformly in the bulk of the photoconductor were due to weekly absorbed light. Initially, before the flow of photocurrent, the field was assumed to be uniform. This implies that in the dark the contacts are either neutral (i.e., the carrier concentrations in the bulk and at the interface are equal) or

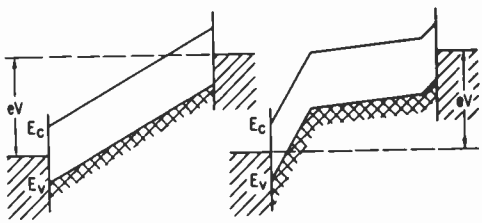

Fig. 8—Energy-band diagram. Diagram on the left is before illumination, on the right during illumination with weakly absorbed light. Zones of high field have formed in front of the contacts.

slightly injecting or blocking so that no distortion of the field occurs and the dark current obeys Ohm's law. Upon illumination the carrier concentration increases in the bulk but not at the contacts, which therefore become blocking. Zones of high fields form in front of the contacts (Fig. 8). The width of the high-field region at the cathode is

given by the electron drift length l_1;

$$l_1 = \mathbf{E}_1 \mu_n \tau_n, \qquad [22]$$

where τ_n is the mean free time before recombination. For ease of argument let us consider only one contact and the adjoining bulk. At low voltages such that the voltage drop across the region l_1 is small compared to that across the bulk, the resistivity of the bulk will determine the I-V characteristic; we expect to obtain Ohm's law;

$$I_{ph} = eg\mu_n \tau_n \frac{V}{L} \qquad [23]$$

where L is the total thickness of the layer. The contribution of the holes to the current is neglected here, because their mobility is assumed to be smaller than that of the electrons. At increasing voltage, the region l_1 will expand and if the voltage drop occurs mainly across l_1, $\mathbf{E}_1 \approx V/l_1$. Then with Eq. (22)

$$I_{ph} = egl_1 = eg(\mu_n \tau_n V)^{1/2} \qquad [24]$$

and the current is seen to follow a $V^{1/2}$ law. At still higher voltages l_1 will become comparable to or greater than L. Then the limiting current density obtained is

$$I_{ph} = egL. \qquad [25]$$

This argument neglects any space charges that might have formed in l_1. In principle, holes could be injected into region l_1 from the bulk, since there the hole concentration is greater than in the high-field region. Then a space-charge-limited current would flow and the relation to be satisfied is

$$I_p = \frac{9}{8} \epsilon\epsilon_0 \mu_p \theta \frac{V^2}{{l_1}^3}. \qquad [26]$$

If this current is smaller than that computed in Eq. [24], the smaller current will prevail. The electron current is still subject to $I_{ph} = egl_1$. From both equations one determines a self consistent l_1 and finds

$$I_{ph} = e \left(\frac{\epsilon\epsilon_0 \mu_p \theta}{e} \right)^{1/4} g^{3/4} V^{1/2}. \qquad [27]$$

The $V^{1/2}$ law was obtained in Eq. [24] by a completely different physical argument from that in Eq. [27]. The only way to differentiate the $V^{1/2}$ laws of Eq. [24] and [27] is through the dependence of the photocurrent on the light intensity.

(c) Schottky Contacts

A different situation arises if the blocking contacts already exist in the non-illuminated material. Then the contact is best described by a Schottky depletion layer whose energy-band scheme for an n-type material is given in Fig. 9. The negative surface charge is essentially compensated by the positive space charge of ionized donors. The width of the Schottky depletion layer is given by

$$d = \left(\frac{2\epsilon\epsilon_0}{\rho}\right)^{1/2} V^{1/2}. \qquad [28]$$

Thermal equilibrium is strongly disturbed and a Fermi level can no longer strictly be defined. However, the requirement that the rate of

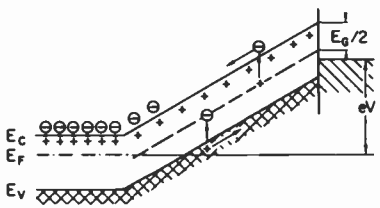

Fig. 9—Schottky depletion layer with voltage V applied. Thermal excitation of carriers to imperfections in the middle of the bandgap gives rise to a dark current.

thermal generation of electrons and holes be identically equal in order to satisfy steady-state conditions leads to a demarcation level near the middle of the forbidden gap such that states above this level are substantially empty and states below are substantially filled with electrons. (The departure of the demarcation level from the middle of the gap depends only logarithmically on the relative electron and hole capture cross sections.) A stationary current is due to the thermal generation of charge carriers.[35] Assuming an essentially homogeneous distribution of imperfection states in the forbidden zone, a two step process is responsible for the carrier generation in the dark—states at or near the middle of the forbidden gap are emptied by excitation of electrons to the conduction band and are refilled by electrons from the valence band at the same rate. This thermal generation process of free electrons and holes occurs at a much higher rate than the direct excitation across the bandgap when the bandgap exceeds about one-half volt. Carrier generation due to impurity states that are not located close to the middle of the forbidden gap can be neglected, since the generation rate of the electrons (or holes) falls off exponentially

with energy, approximately by a factor of 100 per 0.1-eV change in energy. The charge carriers are swept out of the high-field region, and if no transport limitations occur, the current is given by

$$I \approx N_D e \nu_{th} \sigma_n N_c \exp\left\{-\frac{E_g}{2kT}\right\} d, \qquad [29]$$

where N_D is the density of states filled with electrons at mid gap, N_c is the effective density of states, σ_n is the capture cross section for electrons, ν_{th} is the thermal velocity, and E_g is the width of the forbidden gap. From Eq. [28]

$$I = N_d e \nu_{th} \sigma_n N_c \exp\left\{-\frac{E_g}{2kT}\right\} \left(\frac{2\epsilon\epsilon_0}{\rho}\right)^{1/2} V^{1/2}. \qquad [30]$$

Similar arguments hold for carrier generation from surface states. If the blocking contact is formed by ions, (e.g., ions generated in a corona discharge) whose adsorption state is located in energy sufficiently above the top of the valence band, then by the same arguments as before, those surface states N_s must be considered that are filled with electrons and closest to the conduction band. If the deposited ions are the highest lying states occupied by electrons, we have

$$I = eN_c \nu_{th} \sigma_n \cdot N_{\text{ion}} \exp\left\{-\frac{E_{\text{ion}}}{kT}\right\} \propto (V)^{1/2} \exp\left\{-\frac{E_{\text{ion}}}{kT}\right\}, \qquad [31]$$

where E_{ion} is the energy of the ions with respect to the bottom of the conduction band. Since the number of ions N_{ion} in the case of a Schottky depletion layer is proportional to the square root of the voltage, the current density shows the same functional dependence on the voltage as given by Eq. [30]. A voltage-independent current density is obtained only if the carrier generation occurs from the valence to the conduction band via the surface states in the mid gap. Then

$$I = N_s e \sigma \nu_{th} N_c \exp\left\{-\frac{E_g}{2kT}\right\} \qquad [32]$$

Here N_s are now surface states per cm^2 located at mid gap.

If the free electrons and holes are generated by light whose penetration depth is greater than the width of the depletion layer, and if it is assumed that the trapping of the optically generated carriers is sufficiently small to leave the space-charge density unaffected and furthermore that the transit time of the charge carriers through the depletion layer is smaller than the recombination time, then the photocurrent is saturated;

$$I_{ph} = egd. \qquad [33]$$

Hence with Eq. [28]

$$I_{ph} = e\left(\frac{2\epsilon\epsilon_0}{\rho}\right)^{1/2} gV^{1/2}. \qquad [34]$$

With increasing voltage the penetration depth of the light becomes smaller than the width of the depletion layer d, and hence the photocurrent becomes independent of the voltage

$$I_{ph} = eG, \qquad [35]$$

where G is the total rate of generation of carriers by the light.

For illumination with penetrating light the voltage regimes below and above the $V^{1/2}$ law are obtained by similar arguments as before. At sufficiently low voltages the voltage drop across the depletion layer is smaller than that across the bulk of the material, and therefore Ohm's law holds.[36] At sufficiently high voltages, d becomes larger than the thickness of the photoconductor and then the current through the layer becomes independent of voltage.

The surprising feature of all of these considerations is that completely different physical arguments lead to the same voltage dependence of the current.

(d) High-Field Conditions

Up to now it has been assumed that the blocking properties of the contact are maintained even at high field strengths. This is not the case, since it is known that tunneling of charge carriers or Schottky emission from the interface or surface into the bulk of the material occurs. Then an additional contribution to the current density appears which is, in the case of tunneling,[37]

$$I_T = \frac{e^3}{8\pi h E_i} \cdot \mathbf{E}^2 \exp\left(-\frac{8\pi(2m)^{1/2}E_i^{3/2}}{3he\mathbf{E}}\right), \qquad [36]$$

where E_i is the separation of the occupied surface states from the conduction band and is equivalent to a work function. A further contribution may be due to the Schottky effect. The Schottky effect is caused by lowering of the work function due to the image force. One finds for the change ΔE_i of the work function

$$\Delta E_i = -\left(\frac{e^3\mathbf{E}}{4\pi\epsilon\epsilon_0}\right)^{1/2} \qquad [37]$$

giving rise to an increased thermal generation rate from states at en-

ergy E_i. The current density is then, using Eq. [31],

$$I \propto V^{1/2} \exp\left\{-\frac{E_i}{2kT}\right\} \exp\left\{\left(\frac{e^3\mathbf{E}}{4\pi\epsilon\epsilon_0}\right)^{1/2}\right\} \qquad [38]$$

The Schottky effect will be significant whenever ΔE_i is greater than kT, which implies that at room temperature the electric field strength is of the order of 10^4 V/cm.

(e) Field-Dependent Photogeneration and Mobility

The considerations in Section 3 have been based on the assumption that the generation rate of the carriers and their drift mobility μ_D is independent of the electric field. It has been clearly established, however, that in certain photoconductors the applied field modulates the geminate recombination of the electron–hole pair created by the absorbed photon so that the generation rate becomes field dependent.

The analysis of this photogeneration mechanism is generally carried out in the framework of the Onsager formulation.[38–40] Onsager carried out a detailed analysis of the charge separation using the theory of Brownian motion of one particle under the action of the

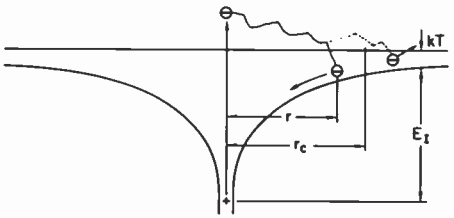

Fig. 10—After excitation the electron has excess energy compared to the thermal energy in the solid. If its thermalization path ends within r_c it will recombine with the hole, otherwise a free electron is created by the photon.

Coulomb attraction of the other particle and of the applied field. The parameters that enter Onsager's theory are the initial thermalization distance r between the oppositely charged carriers and the fraction θ of the absorbed photons that result in thermalized pairs of electrons and holes. The efficiency with which free carriers are generated having no field applied is given by θ, whereas the field-dependence of the generation process is determined by the initial distance r. The field reduces the ionization distance $(r_c - r)$ by reducing the ionization energy and therefore increases the fraction of free carriers generated by the light (Fig. 10). Usually it is assumed that the carrier generation

efficiency can be expressed by a power law;

$$\eta = K \cdot \mathbf{E}^m, \text{ with } m \geq 0.$$

The field dependence of the drift mobility is encountered in amorphous films of organic polymers. The origin of this field dependence has been attributed to the carrier transport via widely separated dimeric sites. But rather than by describing this phenomenon by a field dependence of the drift mobility due to a Poole–Frenkel effect it seems to be appropriate to apply a theory of stochastic processes for the hopping of the carriers from one site to the other.[41] The hopping transport will depend critically on the local separation and local energy fluctuations of the sites and therefore will depend also on the applied field. Many authors[42,43] describe for computational purposes the field dependence of the mobility by a power law,

$$\mu = \mu_0 \cdot \mathbf{E}^n \text{ (with } n \geq 0),$$

without going into the details why the power law should describe the field dependence correctly.

4. Discharge Models

4.1 Quasi-Steady-State Analysis for the Dissipation of the Charge

The calculation of the discharge of a photoconducting dielectric in the dark or under illumination is a rather difficult problem since, for exact solutions, a system of partial differential equations must be solved under the appropriate boundary conditions. The approach that is often used to solve the problem is to assume that the quasi-steady-state holds.[44–47] The continuity equation states that in the configuration of a solid with a free charged surface, the sum of the electron and hole current j_p and of the displacement current are zero during the discharge;

$$j_p(x, t) + \epsilon\epsilon_0 \frac{\partial E(x, t)}{\partial t} = 0. \qquad [39]$$

Integration with respect to x gives

$$\int_0^L j_p(x, t)dx = -\epsilon\epsilon_0 \frac{\partial}{\partial t} \int_0^L \mathbf{E}(x, t)dx = \epsilon\epsilon_0 \frac{dV}{dt} \qquad [40]$$

Quasi steady state means that j_p is, within a good approximation, independent of x so that the integration gives

$$j_p(t, V) = \frac{\epsilon\epsilon_0}{L}\frac{dV}{dt} \qquad [41]$$

In order to illustrate the meaning and the limitations of this assumption the problem of the relaxation of the charge is specified more clearly in the following example.

Let us assume a trap-free solid that, at $t < 0$, is charged with a surface charge Q_s (corresponding to N_s elementary charges/cm^2) to a voltage V_s. The electric field is uniform throughout the dielectric. At $t = 0$ illumination is switched on. The light is strongly absorbed and the penetration depth of the light is assumed to be small compared to the thickness of the sample. For ease of argument let us make the further simplifications that all the light is homogeneously and without reflection losses absorbed within the penetration depth λ, and that no light penetrates beyond λ. Since the solid is assumed to be trap free, the rise time of the photocurrent is given by the recombination, or extraction rate, of the carriers out of the region λ. It is assumed to be negligible.*

In these conditions the discharge is characterized by two extremes: The light intensity is so low that within a time comparable to the transit time the number of carriers per cm^2 generated by the light in the region λ is small compared to the density of the surface charge Q_s/e. Then for a time interval still to be specified the field will not be distorted by the space charge of the injected carriers and the voltage drop in a time $t < T_r$ (T_r = transition time) can be neglected. This implies that for the calculation of $V_s(t)$, $j_p(x, t)$ can be assumed to be independent of x, because after a time of the order of the transit time, the space-charge distribution which maintains constant current density in the solid will have formed. Then, if the optically generated carriers are extracted from λ without recombination losses, one finds

$$\int_0^L j_p(x, t)dx = eg\lambda \cdot L = \epsilon\epsilon_0 \frac{dV}{dt}. \qquad [42]$$

Hence

$$V = V_s - \frac{L}{\epsilon\epsilon_0} eg\lambda \cdot t. \qquad [43]$$

This solution is only valid down to a voltage V_c at which either the assumption of a saturated photocurrent in the region λ can no longer be maintained or the number of carriers generated within a transit

* The rise time of photocurrents has never been taken into account in literature except in a qualitative way.[48]

time (at V_c) becomes comparable to the density of elementary charges on the surface* at V_c. In the latter case, the current becomes space-charge limited and the region λ acts only as an ohmic contact to the region $(L - \lambda)$. Therefore

$$-\frac{9}{8}\epsilon\epsilon_0\mu\frac{V^2}{L^3} = \frac{\epsilon\epsilon_0}{L}\frac{dV}{dt}, \qquad [44]$$

and by integration,

$$V = \frac{V_c}{1 + V_c \cdot \frac{9}{8}\frac{\mu}{L^2} \cdot t}, \qquad [45]$$

or

$$V = \frac{8}{9}\frac{L^2}{\mu}\cdot\frac{1}{t}, \text{ for } t > T_r = \frac{L^2}{\mu V_c}.$$

The whole discharge has been described as a quasi-steady-state discharge. The other extreme is the case of high light intensities, which is encountered when the number of carriers generated within a transit time is large compared to the surface-charge density Q_s/e. Then the region λ acts as a carrier supplying reservoir to region $(L - \lambda)$ right after the light is switched on and obviously the voltage as a function of time cannot be described by the assumption of a quasi-steady state for $t \leq T_r$, since clearly j_p is a function of x in this time interval. Nevertheless we know that after $t = T_r$ the voltage will have dropped by a factor of two because the sheath charge at the surface has transformed into a space charge due to the injection of the carriers into $(L - \lambda)$. For $t > T_r$ quasi steady state will apply, the current through $(L - \lambda)$ being space-charge limited. Then Eq. [41] can be used again. It is worth mentioning that any increase in light intensity does not accelerate the decay of the charge in this mode of discharge. To reiterate, in this case, the assumption of quasi-steady-state discharge is only applicable after the surface voltage drops to half its initial value.

The effect of traps can be visualized qualitatively. Shallow traps (in the region $L - \lambda$) can be taken into account by a reduced drift mobility. The afore-mentioned considerations remain unchanged. The effect of deep traps is more complicated. If the capture rate of free carriers is low compared to the arrival rate of carriers at the back

* In the first case the current through the sample will be limited by the photoconductive processes in the region λ. Limitations of this sort are not considered here.

electrode, then the build up of space charge at the relevant voltage is negligible. This, of course, is not true for all voltages. With decreasing voltage the rate of capture may become larger than the extraction rate. Then a space charge will form in region $(L - \lambda)$ and the current will drop to virtually zero, giving rise to a residual voltage. Strictly speaking the case of deep traps cannot be treated in the quasi-steady-state approach since then $j = j(x, t)$. However, attempts have been made to take trapping into account assuming that the space charge is homogeneously building up during the discharge and by considering only the integral quantities without going into the details of the carrier transport.[49]

All this indicates that the question of whether the discharge of a dielectric can be described by a quasi-steady-state dissipation of the charge depends on materials parameters as well as on the light intensity used for the discharge, the initial surface voltage, and the initial space-charge distribution. These dependences imply that the experimental conditions can be chosen such as to obtain the regime of a quasi-steady-state discharge provided that deep trapping is negligible.

In materials with "high" drift mobilities the conditions for quasi-steady-state discharge are easily fulfilled. The charge density on a photoconductor is usually of the order of a few 10^{12} el. charges/cm^2, the thickness of about 30 μm. With a mobility of ≥ 1 cm^2/Vsec, the transit time is $\leq 10^{-8}$ sec. Therefore in order to generate within 10^{-8} sec 10^{12} charge carriers/cm^2, a light intensity of 10^{20} photons/cm^2 sec would be required, which is indeed very high. Similarly a density of 10^{15} deep traps per cm^3 with a capture cross section of 10^{-15} cm^{-2} can then be neglected, since the mean free time before deep trapping is 10^{-7} sec, i.e., one order of magnitude larger than the transit time.

At the low drift mobilities found in many organic photoconductors, the conditions for quasi steady state may already be violated at normal light intensities of $\sim 10^{13}$ photons/cm^2 sec. At this light level and with a mobility of 10^{-7} cm^2/Vsec, for example, the number of carriers generated within a transit time already equals the number of surface charges.

Summarizing the above ideas, the discussion of the different models for the dissipation of the charge under quasi-steady-state conditions is traced back to the discussion of the various models of Section 3.1. In comparing the results obtained for the decay curves and summarized in Table 4 with experimental curves, one should keep in mind the limitations to which the calculations were subject—no rise-time effects of the photocurrent, no strong trapping by deep traps, and no high light intensities are taken into account. However, the ex-

perimental conditions can be sometimes chosen as to produce quasi-steady-state discharge.

4.2 Exact Analysis

The problem of an exact analysis of the discharge has been attacked by a number of authors.[50–52] The approach is illustrated here by presenting the analysis of the trap-free photoconductor under conditions of high light intensity. Since this case has been also discussed in Section 4.1 in terms of the quasi-steady-state approach, the additional features of the decay curve obtained solely by using the exact analysis can be elaborated.

In the absence of trapping and diffusion, the equations governing the flow of carriers in the photoconductor for a one-dimensional planar geometry are

$$\epsilon\epsilon_0 \frac{\partial \mathbf{E}(x, t)}{\partial t} = -e\mu n(x, t)\mathbf{E}(x, t), \qquad [46]$$

and

$$\frac{\partial \mathbf{E}(x, t)}{\partial x} = \frac{e}{\epsilon\epsilon_0} n(x, t). \qquad [47]$$

Eq. [46] is the continuity equation stating that the total current density is zero and Eq. [47] is Poisson's equation. In order to define the problem completely, the light for discharging the photoconductor is assumed to be strongly absorbed such that its penetration depth is small compared to the thickness of the photoconductor. Furthermore, it is assumed that the free surface of the photoconductor at $x = 0$ is exposed to the light. Then the following boundary conditions are obtained:

(*a*) $E(0, t) = 0$ *for* $t \geq 0$: This condition takes care of the high excitation level at the surface, which increases the carrier density instantaneously to a very high value, thereby reducing the field strength to zero.

(*b*) $E(L, 0) = V_0/L$ *and* $n(x, 0) = 0$: These conditions state that before the illumination, the field is constant and that no charge carriers are present in the photoconductor. The surface is $V(t = 0) = V_0$ and the sample length L.

The complete solution of Eqs. [46] and [47] can be found easily, the complete integral being some arbitrary function $\varphi(x - \mu \mathbf{E}t, \mathbf{E}) = 0$. Rather than looking for particular integrals of this solution, a more physical approach will be used to obtain the solutions in different time intervals.

Table 4—Discharge Characteristics with Quasi Steady State Approach

		Energy band diagram according to the Goodman-du Chatenier model 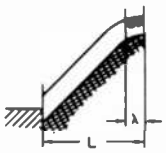	
		I-V Characteristic	Discharge Characteristic
Dark	high voltage	$j = A^* \cdot e^{\alpha V}$ $A^* = eN_c \left(\frac{kT}{2\pi m_{eff}}\right)^{1/2} \cdot e^{-\frac{e\xi(0)}{kT}}$ $\alpha = e/kT \cdot (d\xi/dV)$	$V = V_0 - K \cdot \ln(1 + t/\tau)$ $K = \frac{1}{\alpha}$ $\tau^{-1} = A^* \alpha e^{\alpha V}$
	medium voltages		
	low voltage	$j = \frac{9}{8} \epsilon\epsilon_0 \mu \frac{V^2}{L^3}$	$V = \frac{V_c}{1 + [9\mu V_c/(8L^2)] \cdot t}$
Illum. strongly absorbed light	high voltages	$j = eG$	$V = V_0 - \frac{eL}{\epsilon\epsilon_0} Gt$
	low voltages	$j = \frac{9}{8} \epsilon\epsilon_0 \mu \frac{V^2}{L^3}$	$V = \frac{V_c}{1 + [9\mu V_c/(8L^2)] \cdot t}$
Illum. weakly absorbed light both charge carriers mobile	high voltages	$j = eG$	$V = V_0 - (eL/\epsilon\epsilon_0)Gt$
	medium voltages	$j = eg(\mu_n \tau_n)^{1/2} V^{1/2}$ or $j = eg^{3/4} \left(\frac{\epsilon\epsilon_0 \mu_p}{e}\right)^{1/4} V^{1/2}$	$V^{1/2} = V_0^{1/2} - Bt$ with $B = \frac{1}{2} \frac{egL}{\epsilon\epsilon_0} (\mu_n \tau_n)$ or $B = \frac{L}{\epsilon\epsilon_0} eg^{3/4} \left(\frac{\epsilon\epsilon_0 \mu_p}{e}\right)^{1/4}$
	low voltages	$j = eg\mu_n \tau_n \frac{V}{L}$	$V = V_0 \cdot e^{-t/\tau_{rel}}$ $\tau_{rel} = \epsilon\epsilon_0/(eg\mu_n \tau_n)$

Energy band diagram: Schottky depletion layer	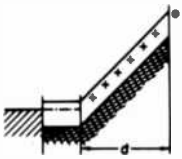

I-V Characteristic	Discharge Characteristic
$j = AV \cdot e^{-\beta/V^{1/2}}$ (tunneling)	$V^{1/2} = e\left(\frac{\epsilon\epsilon_0}{2\rho}\right)^{1/2}[I_0' - \gamma \ln(1 + t/\tau)]$
$j = A'V^{1/2} \cdot e^{\beta' V^{1/4}}$ (Schottky-effect)	$V^{1/2} = e^{1/4}\left(\frac{\epsilon\epsilon_0}{2\rho}\right)^{1/4}[I_0'^{1/2} - \delta \ln(1 + t/\tau)]$
$j = BV^{1/2}$	$V = V_0 \cdot e^{-t/\tau}$
$j = eG(d >> \text{penetration depth of light})$ $j = egd = eg\left(\frac{2\epsilon\epsilon_0}{\rho}\right)^{1/2} V^{1/2}$ (d << penetration depth of light)	$V^{1/2} = V_0^{1/2} - eG(2\epsilon\epsilon_0\rho)^{-1/2} \cdot t$ $V = V_0 \cdot e^{-t/\tau}; \tau = \frac{\rho}{2eg}$
$j = eG$	$V = V_0 - (eL/\epsilon\epsilon_0)Gt$
$j = egd = eg\left(\frac{2\epsilon\epsilon_0}{\rho}\right)^{1/2} V^{1/2}$	$V = V_0 \cdot e^{-t/\tau}; \tau = \frac{\rho}{2eg}$
$j = eg\mu_n \tau_n \frac{V}{L}$	$V = V_0 \cdot e^{-t/\tau_{rel}}; \tau_{rel} = \frac{\epsilon\epsilon_0}{e\mu_n \tau_n g}$

From the continuity Eq. [46], Poisson's Eq. [47], and boundary condition (a), one obtains by integrating with respect to x,

$$\frac{dV}{dt} = -\frac{\mu}{2}\mathbf{E}^2(L, t). \qquad [48]$$

For $t < T_r$, the leading front of the charge carriers has not yet arrived at the cathode, therefore $n(L, t) = 0$. The continuity equation gives then by restricting the consideration to $x = L$;

$$\mathbf{E}(L, t) = \mathbf{E}(L, 0) = \frac{V_0}{L} \; (t \leq T_r). \qquad [49]$$

Inserting Eq. [49] into Eq. [48] the following relations are obtained;

$$\frac{dV}{dt} = -\frac{\mu}{2}\left(\frac{V_0}{L}\right)^2 \qquad [50]$$

and

$$V(t) = V_0 - \frac{\mu}{2} \cdot \left(\frac{V_0}{L}\right)^2 \cdot t, \text{ for } 0 < t = T_r. \qquad [51]$$

The decay rate is, according to this equation, constant and proportional to V_0^2. The voltage decays after a transit time to half of its initial value. It is impossible, in principle, to calculate the decay law using the quasi-steady-state approach in the voltage range between V_0 and $V_0/2$.

After $t \geq T_r$, $n(L, t)$ is no longer zero. It can be shown that $n(L, t) = \epsilon\epsilon_0/(e\mu t)$. Substituting this expression into Eq. [46], integrating, and imposing that $\mathbf{E}(L, t)$ must be continuous at $t = T_r$,

$$\mathbf{E}(L, t) = \frac{L}{\mu} \cdot \frac{1}{t}; \qquad [52]$$

hence with Eq. [48],

$$\frac{dV}{dt} = -\frac{L^2}{2\mu} \cdot \frac{1}{t^2}, \qquad [53]$$

and

$$V = \frac{L^2}{2\mu} \cdot \frac{1}{t}, \text{ for } t > T_r \qquad [54]$$

For $t > T_r$ the hyperbolic time law obtained with the exact analysis corresponds to that of the approximate quasi-steady-state solution.

The influence of deep traps has been considered in particular by K. Keiji Kanazawa and I. P. Batra.[51] They assumed for their calculation that detrapping from the deep traps is negligible, and that the light is

strongly absorbed. Then the charge carriers are injected into the bulk from the free surface. In contrast to the trap-free model above, the light intensity was assumed to be moderate, so that the carrier density at the surface stays sufficiently low to have $\mathbf{E}(0, t)$ virtually undisturbed from its initial value for a short time. The result these authors obtained was that trapping slows down the decay rate and the voltage does not necessarily decay to zero, since the carriers do not travel the entire thickness of the layer. This relationship is illustrated in Fig. 11. Due to the fact that detrapping is neglected, the residual voltage

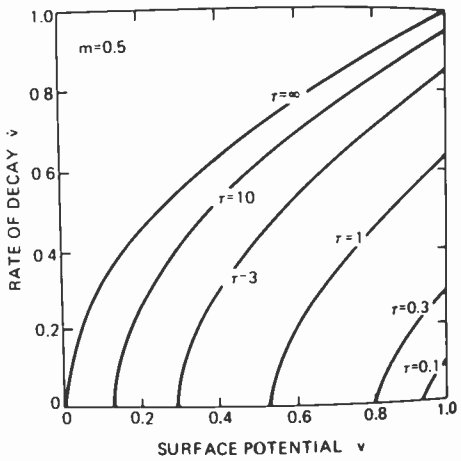

Fig. 11— $\dot{V}/V$ curves for various values of τ. The injection-limited case is represented by the curve labeled $\tau = \infty$. Increasing τ is identical with smaller trapping rate. (After K. K. Kanazawa and I. P. Batra.)

was found to be independent of the light intensity and of the injection process from the illuminated region. The residual voltage V_r is then a function of the $\mu\tau$ product alone, and V_r can therefore be used to determine the lifetime of the carriers. The space-charge distribution is found to be inhomogeneous, indicating the inaccuracy due to taking only the integral space charge into account for calculating discharge curves by the quasi-steady-state approach (Fig. 12). Chen[52] assumed in his calculations an exponential decay of the light intensity going from the surface into the bulk. He also generalized the calculation of the discharge of a trap-free photoconductor using a field-dependent generation rate and field-dependent mobility. Both these effects slow the discharge rate down and give rise to a variety of slightly modified discharge curves, depending on the power laws as-

sumed for the generation rate and mobility. However, there remains the question as to how the photoconductive processes not included in the exact analysis, influence the discharge curves. More sophisticated calculations will have to be done.

5. Examples of Real Materials

Here, selected experimental results on the properties and discharging behavior of photoconducting solids are given. The results are present-

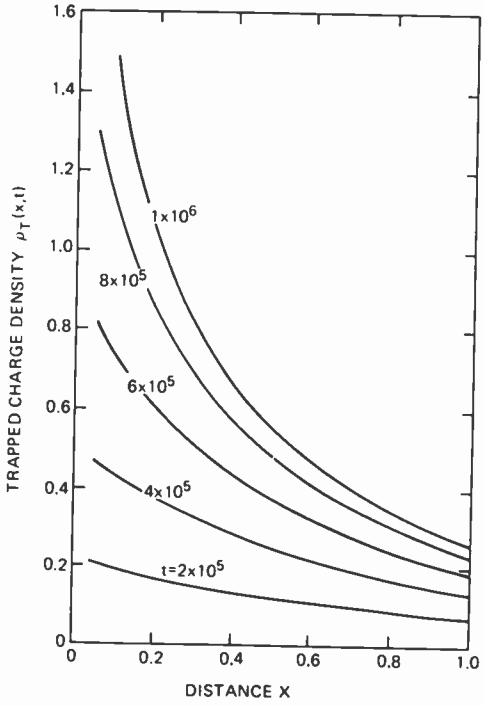

Fig. 12—Buildup of trapped-charge density during the decay of a photoinsulator having $\tau = 1$. The photoinjection rate is assumed constant. $\tau = 1$ means that transit time and trapping time are equal. Time t is expressed in units of the transit time for the leading carrier front. (After K. K. Kanazawa and I. P. Batra.)

ed for inorganic crystalline materials, amorphous inorganic materials, and amorphous organic materials. This sequence reflects changes in the processes of the generation of the charge carriers and in their mobility by many orders of magnitude, properties which should also show up in changes of the discharge behaviour.

5.1 High-Mobility Materials

(a) ZnO single crystals

ZnO single crystals have been investigated by stationary current measurements[53] and by evaluation of the dark decay and light-induced decay of the surface charge.[54,55] The mobility of the electrons in ZnO at room temperature is 200 cm^2/V sec. The I-V characteristics have been measured with conducting crystals of approximately one ohm-cm resistivity. The blocking contact on the free surface was formed by negative ions from a corona discharge, and the current through the samples were measured during the charging process. The results (Fig. 13) indicate that the photocurrent does not obey the laws of Eq. [34]

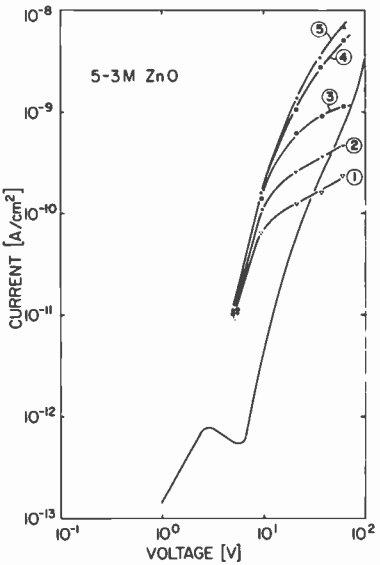

Fig. 13—I-V characteristic of ZnO single crystal with blocking contacts.

and [35] of Section 3.2. It was proposed that this is because hole trapping increases the space-charge density and, therefore, the field at the surface to a value such that tunneling of electrons from the surface into the bulk occurs. At higher voltages a competition between the extraction rate and trapping rate of the holes restores in part the blocking properties of the contact so that the photocurrent flattens off. The dark current also deviates from the expected voltage depen-

dence of Eq. [30]. Detrapping of electrons from deep traps in the depletion layer may make the observation of a stationary current at low voltages very difficult. At high voltages the current is caused by tunneling of electrons from surface states into the bulk, a behavior that was found in measurements of I-V characteristics using liquid contacts.[55]

The discharge curves $V(t)$ of ZnO single crystals are strictly exponential with time (Fig. 14). This has been explained by assuming that the photocurrent is independent of the voltage and that the penetration depth of the light is comparable to the thickness of the depletion layer. Furthermore, trapping of charge carriers need not be taken into

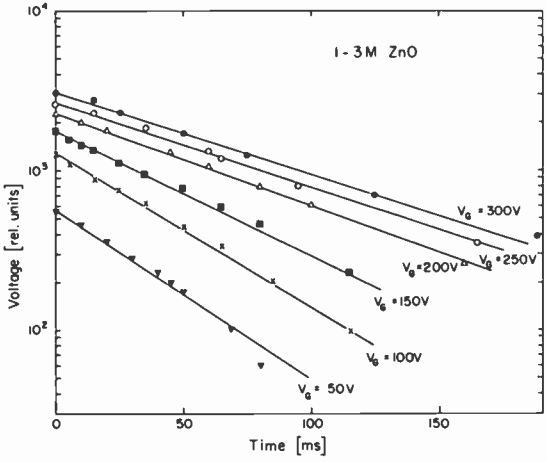

Fig. 14—Discharge curves of ZnO single crystals illuminated at $\lambda = 3700$ Å; $V_G \propto$ surface voltage.

account, in contrast to the stationary photocurrent measurements, because the trapping rate is much smaller than the discharge rate. Therefore the evaluation of the results can be made with the quasi-steady-state model.

The dark decay of corona-charged single crystals can be described by a logarithmic decay law (Fig. 15). Since a photocurrent flows during the charging, the discharge was traced back to an incompletely decayed photocurrent. To obtain a logarithmic decay law, a continuum of traps must be assumed that is filled with photoexcited carriers. There remains the question of whether an explanation on the basis of impurity conduction would result in a similar decay law.

(b) PbO Layers

The properties of polycrystalline PbO layers formed by evaporation have been investigated by Goodman and by du Chatenier. Such layers have a hole mobility of 2.5 cm^2/V sec. In his measurements, du Chatenier used sandwich cells with a transparent SnO_2 layer and an Ag layer as contacts. Goodman had a vidicon structure, i.e., the con-

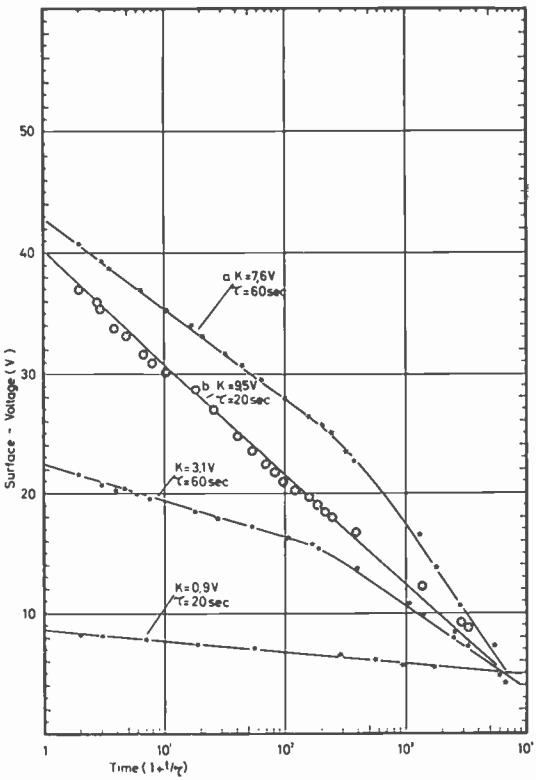

Fig. 15—The dark decay of the surface voltage of conducting ZnO crystals. The time laws are logarithmic and given by $V = V_i - K \log [1 + (t/\tau)] - K \log [1 + (t/\tau)\cdot(\tau/\tau_K)]$. K and τ are indicated at each individual curve. Curves a and b, respectively, are measured before and after exposure of the crystal to light.

tact to the free surface was made with an electron beam, the back contact being an SnO_2 layer also. The following conclusions are based exclusively on measurements of I-V characteristics.

Goodman described his results in terms of the two-layer model outlined in Section 3.1. The I-V characteristic in the dark shows the predicted behaviour—at low voltages a space-charge-limited current and

at high voltages the relation given by Eq. [15]. Evaluation of the results gives an electron trap density of 2×10^{13} $(cm^2\ eV)^{-1}$ at the surface and the Fermi level 0.95 eV below the conduction band. In du Chatenier's photoconduction experiments the relevant charge carriers are the holes. The PbO was illuminated through the transparent electrode, the radiation being sufficiently intense to form a hole injecting contact. The photocurrent shows the V^2 law of SCLC and the saturation expected for the photocurrent at high voltages (Fig. 16). In contrast to the theoretical prediction, the current in the SCLC regime

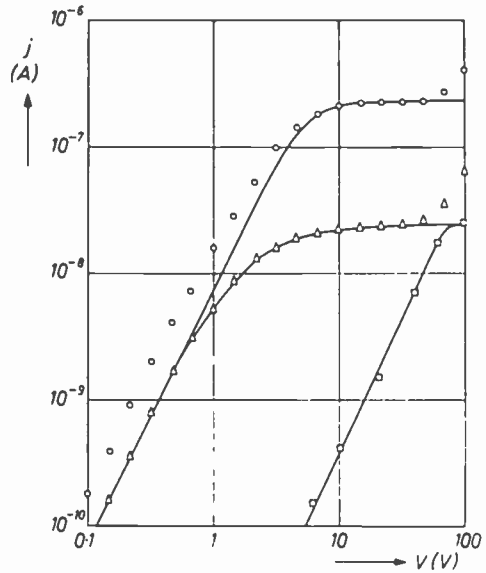

Fig. 16—Measured photocurrent versus voltage for light of 4200 Å. △ and ○ PbO layer No. 1 for light intensities of 1.5×10^{11} and 1.5×10^{12} photons/cm^2 s, □ PbO layer No. 2 for 1.5×10^{11} photons/cm^2. (After F. J. du Chatenier.)

was sensitive to the light intensity. This is probably due to an expansion of the carrier reservoir into the layer as the light intensity increases, resulting in an effectively smaller value of the layer thickness, which enters the current equation in the third power.

5.2 Low-Mobility Materials

(a) Amorphous Se

Amorphous Se has a hole mobility of 0.15 cm^2/V sec and an electron mobility of about 10^{-5} cm^2/V sec. The influence of recombination

and trapping on the discharge curves of positively charged amorphous Se have been discussed.[47] Tabak and Warter[57] pointed out that the range limitations used to describe the light-induced decay curves was inconsistent with the ability to fully discharge Se layers with strongly absorbed radiation. Transient photocurrent measurements with blocking contacts revealed that a field-controlled photogeneration process takes place in Se. Recent measurements of the relative photogeneration efficiency by two-photon generation showed that the field dependence of the generation process can also be completely described with the Onsager theory at low fields.[58] At low fields the Onsager theory predicts a field-independent value due to thermal dissociation of the electron–hole pairs. This field-independent value of the carrier generation has not been found before, since strongly absorbed light had been used so that surface recombination and trapping caused deviations from Onsager's theory.

The light-induced discharge curves must be divided into two categories, according to the light intensity used. At low light intensities the discharge is emission limited, and therefore the field-dependent photogeneration process determines the shape of $V(t)$ curve. Experimental decay curves could be fitted quantitatively in the voltage range of interest by inserting the measured field dependence of carrier generation into the theoretical expressions for the decay curves (Fig. 17). The generation rate in amorphous Se was assumed here to vary as $E^{1/2}$.

Whenever the light level is chosen so high that the number of carriers that are photoexcited within one transit time is equal or larger than the number of elementary charges at the surface, transport limitation due to space charges is observed. This mode of discharge[50] has been achieved with high-intensity light pulses from a Xenon flash lamp. The light intensity was greater than 10^{17} photons/cm^2 sec, in contrast to the previously discussed emission-limited case where the light intensity was 5×10^{10} photons/cm^2 sec. The curves shown in Fig. 18, which give a discharge rate that is initially constant in time, are good evidence for the model developed in Section 4.2. The real proof for the model lies, however, in being able to explain the discharge rate beyond this constant value. According to theory (Eq. [53]) the decay rate should be inversely proportional to the second power of t. The inverse square dependence is indeed satisfied over several decades in discharge rates and transit times (Fig. 19).

(b) Amorphous Polyvinylcarbazole

Amorphous polyvinylcarbazole is characterized by the fact that both

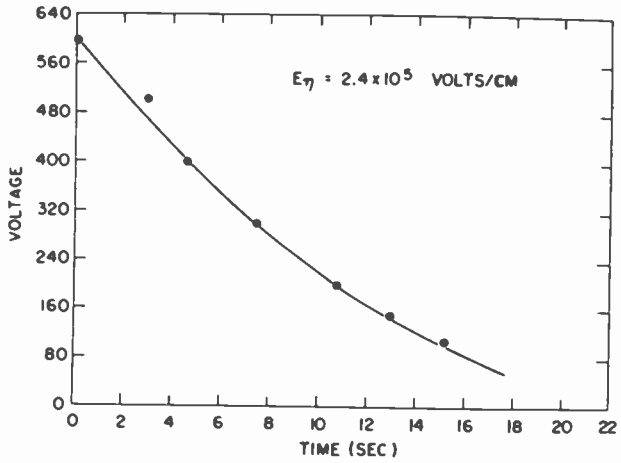

Fig. 17—Discharge data (circles) of amorphous Se compared with that calculated with $G = 5 \times 10^{10}$ photons/cm^2 sec, $\epsilon = 6.3$, $L = 41.6$ μm, $\mathbf{E} = V/L = 2.4 \times 10^5$ V/cm (after I. Chen and J. Mort).

the generation of photocarriers and the mobility of both types of carriers are field dependent.[59–61]

The photogeneration process can be envisaged here as the autoionization of an exciton to a possible intermediate charge-transfer state in which the electron and the hole are thermalized, but in which still significant coulomb attraction exists. Hence in the absence of field, the quantum yield for free carriers is very low. The generation rate can be increased by a separation step due to the applied field. The Onsager formalism can also be applied.

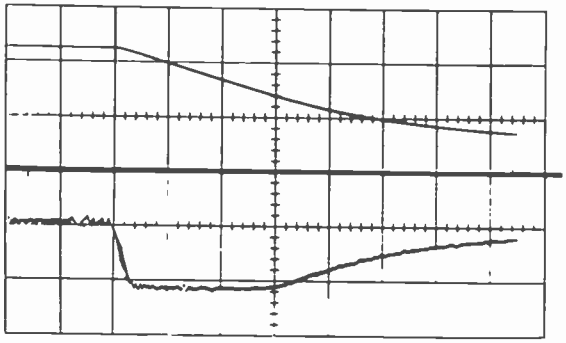

Fig. 18—Photograph showing $V(t)$ (upper trace) and $\dot{V}(t)$ (lower trace). The sweep speed is 0.5 μsec per division. The vertical sensitivities are: upper trace, 50 V per division; lower trace, 2.5×10^7 V/sec per division (after I. P. Batra et al.).

The field-dependent mobility in this material was experimentally found to be

$$\mu_D = \mu_D^0 \left(\frac{\mathbf{E}}{E_0}\right)^2,$$

with $\mu_D{}^0 = 4{\cdot}10^{-7}$ cm^2/V sec and $\mathbf{E}_0 = 10^5$ V/cm. The field dependence of the mobility is not due to field-assisted detrapping of the carriers in the sense of a Poole–Frenkel effect, but must be described rather by a hopping process as mentioned in Section 3.

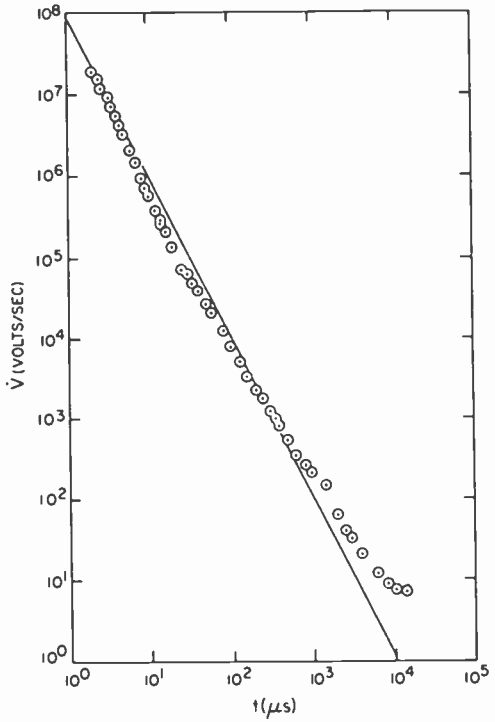

Fig. 19—A log-log plot showing the time dependence of $\dot{V}$. The straight line represents the theoretical fit using a value of $\mu = 0.13$ cm^2/V sec (after I. P. Batra et al.).

The discharge curves should be characterized by both types of field dependences. Decay curves measured by Comizzoli et al.[62] were interpreted solely on the basis of a field-dependent generation rate. In fact a comparison of the theoretical curves calculated by Chen, which include a field-dependent generation rate and mobility, indicates that if $\mu_0 \propto E^2$ would hold down to the lowest fields, a residual voltage of

the order of 10% to 20% of the initial voltage should be observed. Assuming only a field-dependent generation rate, the residual voltage according to Chen's calculation is negligibly small, which is indeed observed. The discrepancy between the transport and the discharge measurements remains to be explained.

6. Conclusions

Though significant progress has been made in recent years, it seems fair to assert that the physics of the electrical charging and discharging of solids is still a fruitful area of research. Progress has been achieved, especially in the understanding of the discharge of photoconductors by light, whereas the relaxation of charge in the dark has been barely investigated. Similarly, the questions of the interaction of ions with semiconductor and insulator surfaces, the questions of frictional and of contact charging are still poorly understood. Modern experimental techniques of surface physics applied to these problems should help to clarify many of the still open problems.

Acknowledgments

It is a pleasure to thank W. J. Merz, A. Rose, and W. C. Stewart for careful reading of the manuscript and for suggestions to improve it.

References:

[1] A. Rose, "The Acoustoelectric Effects and the Energy Losses by Hot Electrons—Part I," *RCA Review*, **27**, p. 98 (1966).

[2] G. A. Harrower, "Auger Electron Emission in the Energy Spectra of Secondary Electrons from Mo and W," *Phys. Rev.*, **102**, p. 340 (1956).

[3] E. H. S. Burhop, *The Auger Effect and other Radiationless Transitions*, University Press, Cambridge (1952).

[4] G. A. Sessler and J. E. West, *Electrets, Charge Storage, and Transport in Dielectrics*, Ed. by M. M. Perlman, Electrochem. Soc. (1973).

[5] E. Bichsel, *American Institute of Physics Handbook*, McGraw-Hill, Third Edition, p. 8–142 (1972).

[6] M. Kaminsky, "Atomic and Ionic Impact Phenomena on Metal Surfaces," in *Struktur und Eigenschaften der Materie*, Vol. XXV, Springer Verlag (1965).

[7] I. A. Abroyan, M. A. Eremeev and N. N. Petrov, "Excitation of Electrons in Solids by Relatively Slow Atomic Particles," *Sov. Phys. USPEKHI*, **10**, p. 332 (1967).

[8] D. W. Vance, "Surface Charging of Insulators by Ion Irradiation," *J.A.P.*, **42**, p. 5430 (1971).

[9] H. D. Hagstrum, "Theory of Auger Injection of Electrons from Metals by Ions," *Phys. Rev.*, **96**, p. 336 (1954).

[10] H. D. Hagstrum, Plenarvorträge der 37. Physikertagung 1973, Physikverlag.

[11] M. M. Shahin, "Use of Corona Discharges for the Study of Ion-Molecule Reactions," *J. Chem. Phys.*, **47**, p. 4392 (1967).

[12] M. M. Shahin, "Mass-Spectrometric Studies of Corona Discharges in Air at Atmospheric Pressures," *J. Chem. Phys.*, **45**, p. 2600 (1967).

[13] M. M. Shahin, "Nature of Charge Carriers in Negative Coronas," *Appl. Optics*, Suppl. 3: Electrophotograph, p. 106 (1969).

[14] T. F. Moran and W. H. Hamill, "Cross Sections of Ion-Permanent-Dipole Reactions by Mass Spectrometry," *J. Chem. Phys.*, **39**, p. 1413 (1963).

[15] M. Takebe, "Positive Ion Species and Their Mobilities in Air," *Japan. J.A.P.*, **13**, p. 207 (1974).

[16] G. P. Harwell, *Principles of Electricity and Magnetism*, McGraw Hill, New York (1938).

[17] R. G. Sachs and D. L. Dexter, "Quantum Limits of the Electrostatic Image Force Theory," *J.A.P.*, **21**, p. 1304 (1950).

[18] H. Kiess, unpublished results.

[19] H. Kiess and T. Freund, "Charge Transfer of Adsorbed Ozone," *J. Phys. Chem.*, 77, p. 556 (1973).

[20] P. E. Wagner, "Electrostatic Charge Separation at Metal-Insulator Contacts," *J.A.P.*, **27**, p. 1300 (1956).

[21] W. R. Harper, "Surfaces Showing No Electrification after Light Contact with Metals," *Proc. Roy. Soc. A*, **218**, p. 111 (1953).

[22] M. I. Kornfeld, "Nature of Frictional Electrification," *Sov. Phys. Sol. State*, **11**, p. 1306 (1969).

[23] H. Bauser, W. Klöpfer and H. Rabenhorst, "Adv. in Static Electricity," Vol. 1, *Proc. of the 1st. Int. Conf. on Static Electricity*, Vienna (1970).

[24] D. K. Davies, "Advances in Static Electricity," Vol. 1, *Proc. of the 1st Int. Conf. on Static Electricity*, Vienna (1970).

[25] F. R. Ruckdeschl, Thesis 1973, University of Rochester, Rochester, N.Y. (Univ. Microfilms, Ann Arbor, Mich.).

[26] A. Wählin and G. Bäckstöm, "Sliding Electrification of Teflon by Crystals," *J.A.P.*, **45**, p. 2058 (1974).

[27] S. V. Pepper, "Auger Analysis of Films Formed on Metals in Sliding Contact with Halogenated Polymers," *J.A.P.*, **45**, p. 2947 (1974).

[28] F. Stöckmann, *Halbleiterprobleme*, 6, p. 279 (1961).

[29] M. A. Lampert, "Volume-Controlled Current Injection in Insulators," *Reports on Progress in Physics*, Vol. XXVII, p. 329 (1964).

[30] A. M. Goodman, internal communication and "An Approximate Model of the Beam-Blocking Contant in a PbO Vidicon," *RCA Review*, **36**, p. 408, Sept. 1975.

[31] F. J. du Chatenier, "Space-Charge-Limited Photocurrent in Vapour-Deposited Layers of Red Lead Monoxide," *Philips Res. Rep.*, **23**, p. 142 (1968).

[32] R. Williams, "Photoemissions of Electrons from Silicon into Silicon Dioxide," *Phys. Rev.*, **140**, p. 569 (1965).

[33] H. Kiess, unpublished results.

[34] A. M. Goodman and A. Rose, "Double Extraction of Uniformly Generated Electron–Hole Pairs from Insulators with Noninjecting Contacts," *J.A.P.*, **42**, p. 2823 (1971).

[35] See, e.g., A Grove, *Physics and Technology of Semiconductor Devices*, J. Wiley and Sons, Inc., N.Y. (1967).

[36] F. W. Schmidlin, G. G. Robert, A. I. Lakatos, "Resistance Limited Currents in Solids with Blocking Contacts," *Appl. Phys. Letters*, **13**, p. 353 (1968).

[37] See, e.g., S. Flügge and H. Marschall, "Rechenmethoden der Quantentheorie," 2. Auflage, Springer Verlag, p. 252 (1952).

[38] L. Onsager, "Initial Recombination of Ions," *Phys. Rev.*, **54**, p. 554 (1938).

[39] J. C. Knights and E. A. Davies, "Photogeneration of Charge Carriers in Amorphous Selenium," *J. Phys. Chem. Sol.*, **35**, p. 543 (1974).

[40] R. C. Enck, "Two-Photon Photogeneration in Amorphous Selenium," *Phys. Rev. Lett.*, **31**, p. 220 (1973).

[41] H. Scher and M. Lax, "Stochastic Transport in a Disordered Solid. I. Theory," *Phys. Rev.*, 7, p. 4491 (1973).

[42] H. J. Wintle, "Surface-Charge Decay in Insulator with Nonconstant Mobility and with Deep Trapping," *J.A.P.*, **43**, p. 2927 (1972).

[43] I. Chen, "Xerographic Discharge Characteristics of Photoreceptors II," *J.A.P.*, **43**, p. 1137 (1972).

[44] H. Seki, I. P. Batra, W. D. Gill, K. K. Kanazawa, and B. H. Schechtman, "A Quasi-Steady-State Analysis for the Electrophotographic Discharge Process," *IBM J. Res. and Development*, **15**, p. 213 (1971).

[45] I. Chen and J. Mort, "Xerographic Discharge Characteristics of Photoreceptors," *J.A.P.*, **43**, p. 1164 (1972).

[46] W. Jaenicke and B. Lorenz, "Halbtonverfahren und Schwärzungskurve der Elektrophotographie," *Z. Elektrochemic*, **65**, p. 493 (1961).

[47] H. Tung Li and P. J. Regensburger, "Photoinduced Discharge Characteristics of Amorphous Selenium Plates," *J.A.P.*, **34**, p. 1730 (1963).

[48] H. J. Gerritsen, W. Ruppel, and A. Rose, "Photoproperties of Zinc Oxide with Ohmic and Blocking Contacts," *Helv. Phys. Acta*, **30**, p. 504 (1957).

[49] H. Kiess, "Note on the Discharge of Electrophotographic Material by Light," *J.A.P.*, **40**, p. 4054 (1969).

[50] I. P. Batra, K. K. Kanazawa, and H. Seki, "Discharge Characteristics of Photoconducting Insulators," *J.A.P.*, **41**, p. 3416 (1970).

[51] K. Keiji Kanazawa and I. P. Batra, "Deep-Trapping Kinematics," *J.A.P.*, **43**, p. 1845 (1972).

[52] H. Kiess, *Physik. Verhandlungen der DPG*, Munster (1973).

[53] H. Kiess, *Current Problems in Electrophotography*, ed. by W. F. Berg and K. Hauffe, Walter de Gruyter (1972).

[54] H. Kiess, *Appl. Optics, Supplement on Electrophotography*, "Investigation of the Electrophotographic Properties of ZnO Single Crystals," p. 100 (1969).

[55] H. Kiess, "High Field Behaviour of ZnO: I Investigation of the Dark Current," *J. Phys. Chem. Sol*, **31**, p. 2379 (1970).

[56] M. J. Tabak and P. J. Warter, "Field Controlled Photogeneration and Free-Carrier Transport in Amourphous Selenium-Films," *Phys. Rev.*, **173**, p. 899 (1968).

[57] R. C. Enck, D. M. Pai, and M. R. Scharfe, *1974 Summer Symp., Photoconductor Image Technology, Theory and Practice*, North Randall, Ohio (Publ. by SPSE).

[58] B. J. Regensburger, "Optical Sensitization of Charge Carrier Transport in Poly (n-Vinyl Carbazole)," *Photochem. Photobiol. J.*, **8**, p. 429 (1968).

[59] R. M. Schaffert, "A New High-Sensitivity Organic Photoconductor for Electrophotography," *IBM J. of Research and Dev.*, **15**, p. 75 (1971).

[60] J. Mort, "Transient Photoinjection of Holes from Amorphous Se into Poly (N-Vinyl Carbazole)," *Phys. Rev.*, **5B**, p. 3329 (1972).

[61] R. B. Comizzoli and H. Kiess in *Current Problems in Electrophotography*, ed. by W. F. Berg and K. Hauffe, Walter de Gruyter (1972).

[62] R. K. Swank, "Surface Properties of II–VI Compounds," *Phys. Rev.*, **153**, p. 844 (1967).

Measurement of the Effective Photoelectron Emission Energy

L. A. Ezard*

RCA Solid State Division, Lancaster, Pennsylvania

Abstract—A novel technique is introduced and demonstrated to measure the effective photoelectron emission energy in an image tube with a uniform electric field by comparing the measured modulation transfer function (MTF) to the theoretical MTF expected for monoenergetic electron emission obeying Lambert's Law. Measurements of MTF in an image tube with a uniform electric field are presented. The results indicate that for a multi-alkali photocathode and for incident photons with energies less than 2.5 eV, the electron emission energies are relatively low, less than 0.2 eV.

Introduction

This paper describes a novel technique for measuring the effective emission energy of electrons emitted by a photocathode. The effective electron emission energy, φ_e, is a weighted average energy that characterizes a polyenergetic electron emission distribution such that the measured MTF curve with polyenergetic electron emission corresponds to the theoretical MTF curve calculated for monoenergetic electron emission having an energy φ_e. The evaluation of the effective emission energy is achieved in two steps. First, the modulation transfer function (MTF)[1,2] is measured in a bi-planar image tube.[3] The tube is operated at a voltage V, with a spacing d between the photocathode and the phosphor screen to obtain a uniform electric field be-

* Presently Assistant Professor, Pennsylvania State University, Middletown, Pa.

tween the photocathode and the phosphor screen. Second, the measured MTF is compared with the theoretically calculated MTF based on monoenergetic electrons emitted from the photocathode. The electron emission is assumed to follow Lambert's Law.

The theoretical MTF for a uniform-electric-field image tube with monoenergetic photoemission obeying Lambert's Law is given by (see Appendix)

$$\mathrm{MTF} = \left| \frac{2J_1\,(4\pi f d\,\sqrt{\varphi/V})}{4\pi f d\,\sqrt{\varphi/V}} \right| \qquad [1]$$

where J_1 is the first-order Bessel function, f is spatial frequency in cycles per millimeter; $e\varphi$ is the electron emission energy in joules; and e is the charge of the electron, 1.6×10^{-19} coulomb. The MTF is plotted as a function of the argument $fd\sqrt{\varphi/V}$ in Fig. 1.

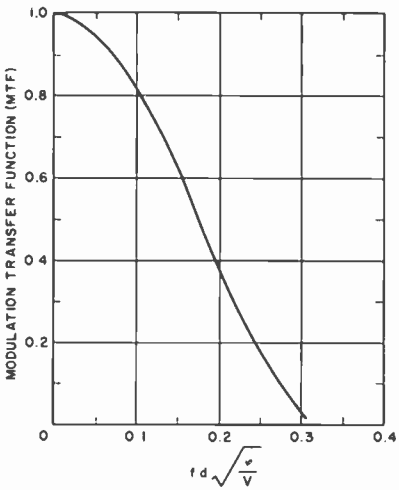

Fig. 1—Calculated MTF versus the quantity $fd\sqrt{\varphi/V}$ for an image tube with monoenergetic electron emission and the condition $\varphi \gg V$. The spacing is d in mm, electron emission energy $e\varphi$ in eV, applied potential V in volts and the spatial frequency f in cycles/mm.

Technique for Measuring MTF of an Image Tube

The modulation transfer function of an image tube having an S20 photocathode was measured with an applied potential of 28 kV. The distance between the photocathode and phosphor screen was 56 mm. This distance limits the resolution to about five or six cycles/mm at

MTF values greater than five percent for the range of applied voltages and input photon energies considered. However, this limitation is an advantage in evaluating the electron optics. The MTF of the electron optics that we seek to evaluate must be obtained by measuring the MTF of the image tube. Furthermore, the optical system composed of the equipment, the electron lens, and the phosphor screen is linear and spatially invariant.[4,5] Therefore, the measured MTF of the image tube is the product of the MTF of the electron lens, the MTF of the phosphor screen, and the MTF of the equipment. Thus,

$$\mathrm{MTF}_{\text{electron lens}} = \frac{\mathrm{MTF}_{\text{tube}}}{(\mathrm{MTF}_{\text{equipment}})(\mathrm{MTF}_{\text{phosphor}})} . \qquad [2]$$

Although the MTF of phosphor screens varies somewhat, at spatial frequencies less than 5 to 10 cycles/mm, the variation is in the range of a few percent while the MTF is usually greater than 90%. The MTF of the equipment is also greater than 90% for spatial frequencies less than 5 cycles/mm. Thus, the sources of variation and cumulative errors in the measurements are reduced.

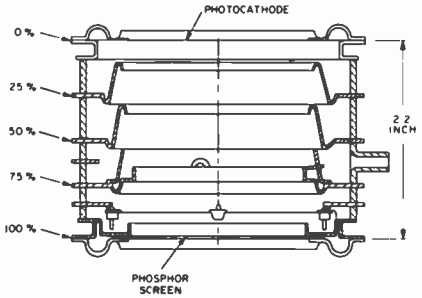

Fig. 2—Cross-section view of the C70021A image tube used to evaluate MTF of an image tube. The first, second and third intermediate electrodes were operated respectively at 25%, 50%, and 75% of the total applied voltage between the photocathode and the phosphor screen to obtain a uniform electric field.

The RCA C70021A image tube was used to evaluate the MTF of a uniform electric field image tube. This tube, a cross-section of which is shown in Fig. 2, is designed to be operated with a uniform electric and magnetic field parallel to the tube axis. The internal electrodes are connected to a power supply to achieve a uniform electric field, and an external solenoid is used to achieve a uniform magnetic field. For these experiments, the magnetic solenoid was not used. The S20 multialkali photocathode in this tube had a sensitivity of 165 uA/lm.

A block diagram of the apparatus used for measuring the MTF of this tube is shown in Fig. 3. In this setup, a test-object pattern consisting of alternate black and white bars is projected onto the image-tube photocathode by a lens. A second lens then focuses the image at the phosphor screen onto the slit. The phototube converts the light falling on the slit to an electrical signal which is amplified and displayed on the recorder. The test pattern is moved slowly to place the various spatial frequencies into the object space of the lens. The filter can be used to limit the photon energies incident on the photocathode.

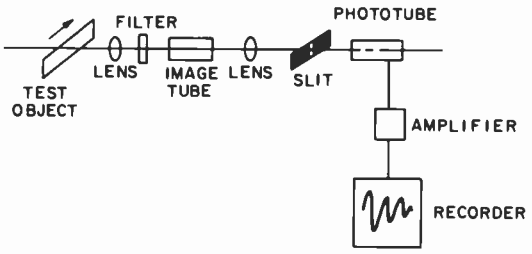

Fig. 3—Schematic of the equipment for measuring the MTF of an image tube.

Because the test pattern consists of black and white bars, rather than a sinusoidal transmittance, the square-wave response $r(n)$ is measured. The sine-wave response $R(n)$ (or MTF) is easily obtained by applying the Fourier conversion formula developed by Coltman[6] as follows:

$$R(n) = \frac{\pi}{4}\left[r(n) + \frac{r(3n)}{3} - \frac{r(5n)}{5} + \frac{r(7n)}{7} + \ldots\right] \qquad [3]$$

where n represents a particular spatial frequency.

To evaluate the MTF of the electron optics of the image tube, first, the square-wave equipment response is measured and converted to MTF with Eq. [3]. Then, a separate evaluation of the phosphor MTF is made. The image-tube square-wave response is measured, as in Fig. 3, and converted to MTF with Eq. [3]. Finally, the electron optics MTF is obtained by dividing the tube MTF by the product of the equipment MTF and the phosphor MTF, as outlined in Eq. [2].

The MTF as a function of spatial frequency was measured with various narrow-bandpass filters placed adjacent to the photocathode. The filters had a nominal pass-band of 1.5% of the peak wavelength at one-half the peak transmission. Because of equipment limitations,

the wavelength variation was confined to between 500 and 850 nanometers. Below 500 nm the radiant energy from the tungsten lamp falls off, and above 850 nm the photocathode response decreases rapidly. At either extreme, the energy into the phototube was low enough so that a signal-to-noise problem limited the measurements on the recorder.

Fig. 4 shows the MTF as a function of the spatial frequency for incident photocathode radiation at 500, 600, 700, 800, and 850 nm. As expected from the theory, the MTF at a specified frequency decreases for a decrease in the wavelength of the incident radiation, which corresponds to an increase of photoemitted electron energy.

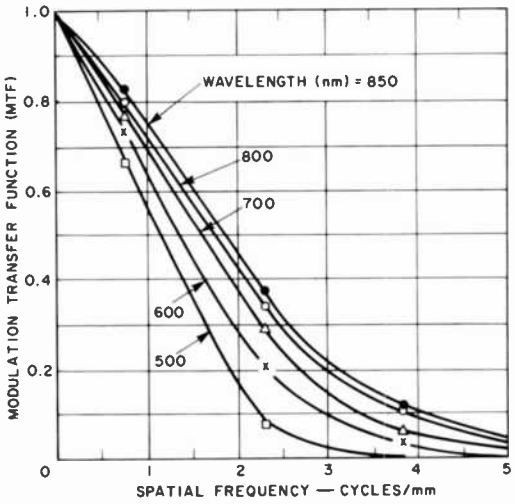

Fig. 4—MTF versus spatial frequency for the C70021A image tube as a function of incident radiant energy at various wavelengths. The operating potential was 28 kV.

Evaluation of the Effective Electron-Emission Energy

At this point the effective photoemitted electron energy will be estimated by comparing the theoretical MTF of monoenergetic electron emission with the MTF measurements. An example will demonstrate the technique. The MTF curves for the C70021A image tube operated at 28 kV and various input radiations are given in Fig. 4. Johnson[12] has shown that a plot of ln(MTF) versus spatial frequency on log–log graph paper can transform many measured MTF curves to straight lines over a large range of spatial frequencies. This technique

was used to transform the curves of Fig. 4 to the straight lines in Fig. 5. In addition, a theoretical MTF curve is given for Lambertian monoenergetic emission in Fig. 5. This theoretical MTF curve was plotted using Eq. [1] with d, φ, and V equal to unity. This curve can be used to predict the MTF of a uniform-electric-field image tube. Each value of MTF corresponds to a spatial frequency f_t on the theoretical MTF curve of Fig. 5. For example an MTF of 0.4 corresponds to $f_t = 0.2$. For an image tube with spacing d and applied potential V between the photocathode and phosphor screen and with effective

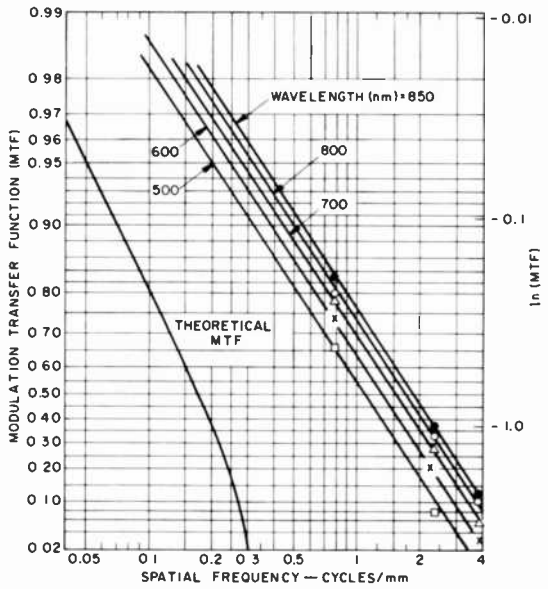

Fig. 5—MTF versus spatial frequency for the C70021A as a function of incident radiant energy at various wavelengths. The theoretical MTF curve is used to evaluate φ_e, the effective electron emission energy.

electron emission energy φ_e, the predicted spatial frequency f is

$$f = (1/d)(V/\varphi_e)^{1/2} f_t \qquad [4]$$

The C70021A image tube was operated at 28 kV and the spacing was 56 mm. For an MTF of 0.3, the spatial frequency (measured value) on the curve for 500 nm radiation was 1.68. Then solving Eq. [4] for the effective electron emission energy φ_e yields

$$\varphi_e = (V/d^2)(f_t/f)^2 = \frac{28000}{56^2}(0.225/1.68)^2 = 0.163. \qquad [5]$$

The ratios f_t/f were determined for each wavelength and the corresponding values of φ_e were calculated. Fig. 6 shows the calculated value of φ_e as a function of the input photon energy. A curve was drawn through the points to facilitate the estimation of φ_e for various incident photon energies. Apparently, the effective electron emission energy does not vary directly with the input radiation, but the distributions are probably skewed toward low emission energies. It is noted that, as the incident photon energy approaches the threshold energy of the multi-alkali photocathode, the electron emission energy must approach zero.

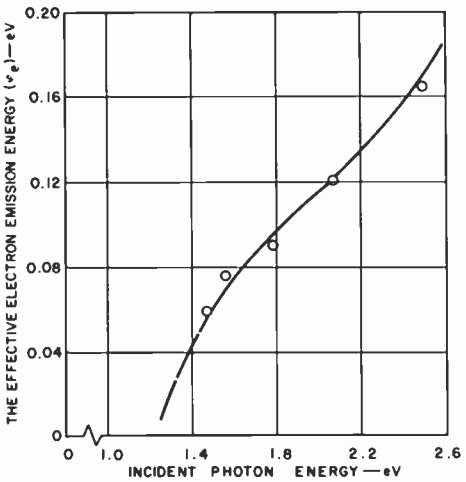

Fig. 6—The incident photon energy versus the calculated effective electron emission energy. As the incident photon energy approaches the photoemission threshold energy of the photocathode, the effective electron emission energy approaches zero.

Finally, we discuss the fact that the value of φ_e calculated depends upon the value of MTF chosen to compare the measured MTF with the theoretical MTF. This is because the slopes of the measured curves do not correspond to the slope of the theoretical MTF curve. This difference is probably due to the fact that the actual photoemission is polyenergetic instead of monoenergetic. For a given spatial frequency, low-energy electron emission leads to high values of MTF, while high-energy electrons result in lower values of MTF. The slope of the theoretical MTF curve for monoenergetic emission, as shown in Fig. 5, is approximately two. An electron energy distribution that is

skewed toward low emission energies can result in an MTF curve with a slope of less than two.

Conclusions

A technique has been demonstrated to characterize the photoemission energy from a polyenergetic source in terms of an effective electron emission energy, φ_e, by comparing the measured MTF in a uniform electric field image tube with the theoretical MTF expected from a monoenergetic source with Lambertian emission. The measurements for the S20 multi-alkali photocathode indicate that for incident photon energies less than 2.5 eV at 500 nm the effective electron emission energies are relatively low, less than 0.2 eV.

The effective electron emission energy of a photocathode is a valuable piece of information, because it is necessary in any attempt to predict the performance of electron optical imaging devices. Furthermore, the measurement of photoemission energy from photocathodes is very difficult to achieve using other techniques.[7,8]

Acknowledgments

The author would like to express his appreciation to Professor Showers for advice and encouragement during the course of this work as his dissertation supervisor at the University of Pennsylvania. Also the author is grateful to his immediate supervisors at RCA, R. W. Engstrom and R. E. Simon for their encouragement, advice, and support to complete this study. Finally, the author wishes to thank E. G. Ramberg for his advice, constructive criticism, and suggestions.

Appendix—Calculation of the Modulation Transfer Function of a Uniform-Electric-Field Image Tube

The bi-planar image tube[3] is the simplest kind of image tube, consisting of a plane photocathode and a plane phosphor screen spaced a small distance from each other in an evacuated envelope. A potential of several kilovolts is applied between the photocathode and phosphor screen. Under this potential, the photoelectrons emitted from the photocathode are accelerated toward the phosphor screen. A point source of electrons at the cathode results in a small circular luminous spot on the screen.

The modulation transfer function is the absolute value of the optical transfer function. The optical transfer function (OTF) can be defined[4,5] as the ratio of the Fourier transform of the image to the Fou-

rier transform of the object. The Fourier transforms are normalized to unity at zero spatial frequency. If the object is a point whose Fourier transform is unity, then the OTF is simply the Fourier transform of the image of the point object. The image of a point object is called a point spread function (PSF). For a circular symmetric PSF, the OTF can be written in terms of the Fourier–Bessel transform:

$$\mathrm{OTF} = \frac{\int_0^\infty r\,P(r)\,J_0(2\pi f r)\,dr}{\int_0^\infty r\,P(r)\,dr}. \qquad [6]$$

In this equation, $P(r)$ represents the amplitude of the PSF at the radius r, J_0 is the zero-order Bessel function, and f is the spatial frequency.

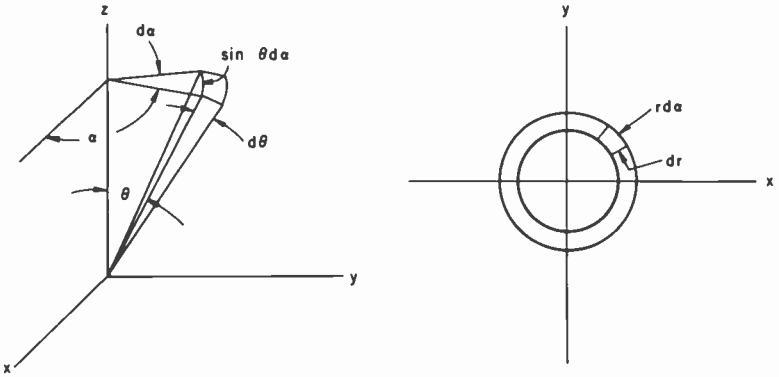

Fig. 7—(a) Lambertian emission current *di* into a differential solid angle and (b) differential area da_i in the image.

For an image tube with spacing d between the photocathode and screen and an applied voltage V, an electron emitted from the axis at the angle θ from the normal with initial energy $e\varphi$ (where $\varphi \ll V$) will strike the screen at distance r from the axis, as follows[9]:

$$r = 2d \sin\theta \sqrt{\frac{\varphi}{V}}. \qquad [7]$$

To calculate $P(r)$ an infinitesimal area in the object plane is considered, as shown in Fig. 7, which has an emission current i_0. Assuming Lambertian emission,[10] the emission current di from an infinitesimal area into a differential solid angle between θ and $\theta + d\theta$ and α and $\alpha + d\alpha$ is given by

$$di = (i_0/\pi) \cos\theta \sin\theta \, d\theta \, d\alpha \, . \qquad [8]$$

This current falls on a differential area da at the image plane given by the expression

$$da_i = rdrd\alpha \, . \qquad [9]$$

The current density dj at the image is given by the ratio of di and da_i and is equal to $P(r)$, which by use of Eqs. [8] and [9] is expressed by

$$P(r) = \frac{(i_0/\pi) \sin\theta \cos\theta \, d\theta \, d\alpha}{rdrd\alpha} . \qquad [10]$$

The radius corresponding to the differential image area is given by Eq. [7].

Substitution of the relations for r and $P(r)$ given in Eqs. [7] and [10], respectively, into the expression for OTF in Eq. [6] produces

$$\text{OTF} = \frac{\int_0^\infty r\left[\frac{i_0 \sin\theta \cos\theta \, d\theta \, d\alpha}{\pi rdrd\alpha}\right] J_0 (4\pi fd \sin\theta \sqrt{\varphi/V}) \, dr}{\int_0^\infty r \left[\frac{i_0 \sin\theta \cos\theta \, d\theta \, d\alpha}{\pi rdrd\alpha}\right] dr} \qquad [11]$$

After simplifying and with a change in the integration variable,

$$\text{OTF} = \frac{\int_0^{\pi/2} [\sin\theta \cos\theta] \, J_0(4\pi fd \sqrt{\varphi/V} \sin\theta) \, d\theta}{\int_0^{\pi/2} \sin\theta \cos\theta \, d\theta} . \qquad [12]$$

This expression can be integrated directly in terms of a first-order Bessel function[11] as follows:

$$\text{MTF} = \left| \frac{2J_1 (4\pi fd \sqrt{\varphi/V})}{4\pi fd \sqrt{\varphi/V}} \right| . \qquad [13]$$

It is apparent from the argument in Eq. [13] that for a specific value of MTF the following relationship is expected

$$f \propto (1/d)(V/\varphi)^{1/2} . \qquad [14]$$

References

[1] R. L. Lamberts, "Application of Sine-Wave Techniques to Image-Forming Systems," *J.SMPTE*, 71, p. 635 (Sept. 1962).

[2] R. L. Lamberts, "Measurement of Sine-Wave Response of a Photographic Emulsion," *J. Opt. Soc. Amer.*, **49**, p. 425 (1959).

[3] P. Grivet, *Electron Optics*, pp. 360–383, Pergamon Press, New York, N.Y. (1965).

[4] J. W. Goodman, *Introduction to Fourier Optics*, McGraw-Hill Book Co., Inc., New York, N.Y. (1968).

[5] E. L. O'Neill, *Introduction to Statistical Optics*, Addisson-Wesley Pub. Co., Inc., Reading, Mass. (1963).

[6] J. W. Coltman, "The Specification of Imaging Properties by Response to a Sine-Wave Input," *J. Opt. Soc. Amer.*, **44**, p. 468 (1954).

[7] A. H. Sommer, *Photoemissive Materials*, John Wiley & Sons, Inc., New York, N.Y. (1968).

[8] W. E. Spicer, "The Production of Pairs in Semiconductors by Low-Energy Electrons," *J. Phys. Chem. Solids*, **22**, p. 265 (1961).

[9] V. K. Zworykin and E. G. Ramberg, *Photoelectricity*, John Wiley & Sons, Inc., New York, N.Y. (1949).

[10] V. K. Zworykin, G. A. Morton, E. G. Ramberg, J. Hillier, and A. W. Vance, *Electron Optics and the Electron Microscope*, John Wiley & Sons, Inc., New York, N.Y. (1945).

[11] M. Abramowith and L. Stegun, *Handbook of Mathematical Functions*, Dover Publications, Inc., New York, N.Y. (1965).

[12] C. B. Johnson, "A Method for Characterizing Electro-optical Device Modulation Transfer Functions," *Photogr. Sci. Eng.*, **14**, p. 413 (Nov.-Dec. 1970).

MTF Measurements of an Image Tube Electron Lens

L. A. Ezard*

RCA Solid State Division, Lancaster, Pennsylvania

Abstract—A technique is presented for evaluating the MTF of the phosphor screen and the electron lens of an image tube. The technique incorporates a slit adjacent to the phosphor screen. MTF measurements are also presented for a fiber-optic faceplate. The measurements indicate that, for a fixed value of MTF, the spatial frequency is directly proportional to the applied voltage and is inversely proportional to the initial emission energy of photoelectrons.

Introduction

In recent years, it has become standard practice to specify the imaging properties of image tubes in terms of the modulation transfer function (MTF).[1–5] The MTF measurement of the image tube usually includes the characteristics of the input and output faceplates (often fiber optics), the electron lens, and the phosphor screen. MTF measurements have been presented in the literature for phosphor screens and fiber-optic faceplates, but only occasionally for the electron lens. It is desirable to know how the MTF of the electron lens varies with the tube operating voltage, because the gain of an image tube is often controlled by varying this voltage. It can be shown[1] that for a fixed value of MTF, the spatial frequency f is directly proportional to the applied voltage and is inversely proportional to the initial emission energy of photoelectrons.

* Presently Assistant Professor, Pennsylvania State University, Middletown, Pa.

An experimental image tube with a multi-alkali photocathode was produced to evaluate the modulation transfer function of the electrostatic electron-optical system. In this tube, it was also possible to evaluate the MTF of the phosphor screen. A cross-section of the tube is given in Fig. 1. The image tube is a triode, consisting of a photocathode, a focus electrode, and the anode. A fiber-optic faceplate is used for the photocathode window, and a glass faceplate is used at the phosphor screen. The phosphor screen is a conventional P20 phosphor with a screen weight of 0.8 to 1.0 mg/cm^2 with a 1000 Å thick evaporated aluminum film.

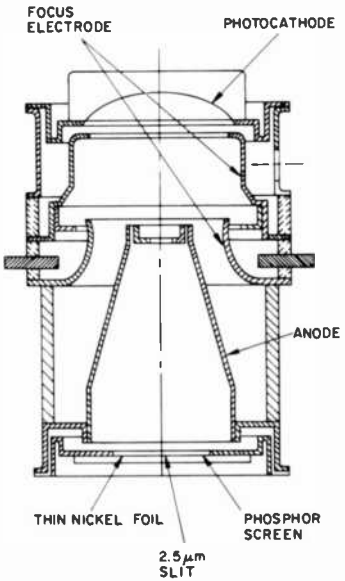

Fig. 1—Cross-sectional view of the modified C21135 image tube.

A thin nickel film, about 8 μm thick, with a 2.5 μm slit, and a 0.05 × 0.05 inch open area was placed adjacent to the aluminized phosphor screen. The 0.05-inch-square open area permits visual observation of the image on the phosphor screen to make necessary light, optical, and electronic-focus adjustments. The 2.5 μm slit is used as an analyzing slit to measure the MTF of the phosphor screen and the electron-optical system on the tube axis.

Phosphor-Screen MTF Measurements

The modulation transfer function of the phosphor screen was mea-

sured using the technique shown in Fig. 2. The image tube was focused, and a collimated light source was used to illuminate the photocathode in an area corresponding to the 2.5 μm slit. The electrons approach the slit at very small angles and can be considered to be a collimated source of electrons flooding the 2.5 μm slit. The line spread function (i.e., the image of a line object) emanating from the phosphor screen was analyzed by an MTF Analyzer.* The line spread function was relayed by the microscope lens and focused on a trans-

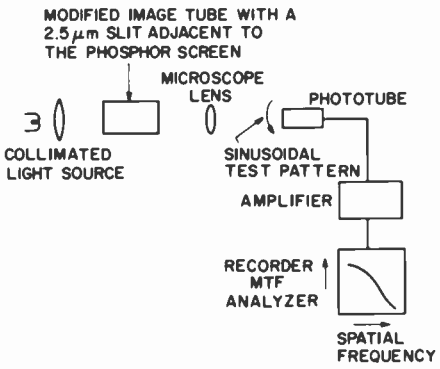

Fig. 2—Technique for measuring MTF of the phosphor screen in an image tube.

parent test pattern of variable density. The test pattern is fixed to a rotating drum. The sinusoidal test pattern varied continuously in a logarithmic manner from 0.4 to 10 cycles/mm. The light passing through the test pattern was detected by a photomultiplier tube, amplified, and displayed on a recorder. A suitable circuit was used to synchronize the x deflection of the recorder with the spatial frequency of the test pattern. The 10× microscope relay lens results in a measurement over the frequency range of 4 to 100 cycles/mm.

A separate MTF measurement was made of the equipment response with a 2.5 μm slit and also of the MTF of a similar fiber-optic faceplate. A correction was then applied to obtain the MTF of the phosphor screen where

$$\mathrm{MTF}_{\mathrm{phosphor}} = \frac{\mathrm{MTF}_{\mathrm{measured}}}{\mathrm{MTF}_{\mathrm{equipment}}} \qquad [1]$$

The MTF of the phosphor screen is shown in Fig. 3 for several voltages over the range of 4 to 12 kV. As expected, the MTF is lower at low voltages. This reduction is probably due to increased scattering of

* Model KIb, Optics Technology, Inc.

the electrons in the aluminum film and in the phosphor screen at the lower voltages.

The MTF's of the fiber-optic faceplate* and of the MTF analyzer are also shown in Fig. 3. The fiber-optic faceplate performance exceeds the performance of the phosphor screen.

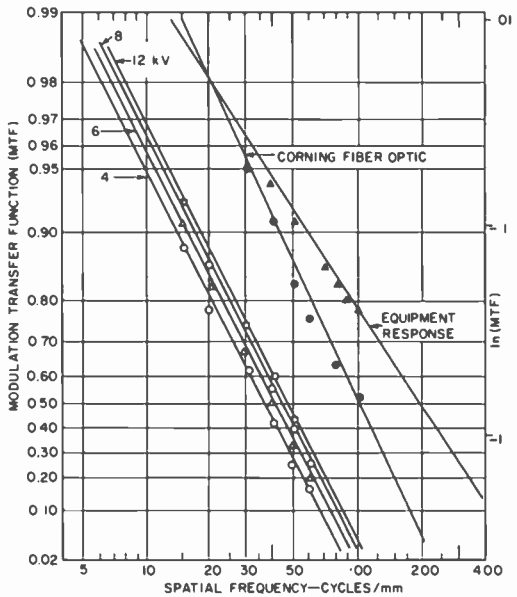

Fig. 3—MTF of a phosphor screen, fiber-optic faceplate, and the MTF equipment.

MTF Measurement and Discussion of Results

This study evaluates the manner in which MTF varies with operating voltage and initial electron emission energy. Theoretical analysis[1,6–8] predicts that, for an electrostatically-focused image tube and for a given MTF, the spatial frequency varies directly with the electric field at the photocathode and inversely with the electron emission energy, $e\varphi$. Because, for a given tube geometry, the electric field at the photocathode varies directly with applied potential V, the relation $f \propto V/\varphi$ is expected for a given value of MTF for the image inverter tube.

Fig. 4 shows the technique used to measure the MTF of the electron-optical system of the image tube. A test pattern with four dis-

* Corning Glass Works Co.

crete known spatial frequencies in the form of black and white bars was illuminated by a light source and imaged on the photocathode by the projection lens. The bar image on the photocathode was focused on the 2.5 μm slit adjacent to the phosphor screen by the electron lens of the image tube. The phosphor screen did not degrade the MTF but served only as a transducer to change the electron energy, incident on the slit, to light. The light on the phosphor screen was relayed by a microscope lens to a photomultiplier tube. The phototube signal was amplified and displayed as the y-axis signal on a recorder. The pen was driven in the x-axis direction by an internal sweep circuit. When a white bar was focused on the photocathode, a signal was

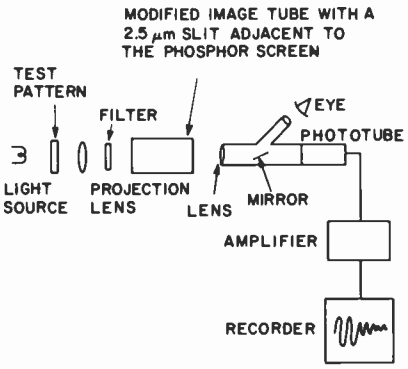

Fig. 4—Technique for measuring MTF of the electron optical system of an image tube.

received by the phototube and displayed on the recorder; a black bar resulted in a minimum signal on the recorder. The test pattern was moved in a direction perpendicular to the bars to generate the variation of signal. The adjustment of the light optical focus of the pattern on the photocathode, the alignment of the bar pattern with the slit, and the adjustment of the tube electronic focus are quite critical. Because the precision of the MTF measurements is limited by the focus and alignment, the measured MTF represents a minimum value to be expected. The actual MTF may be somewhat higher.

The square-wave response measurements were converted to MTF measurements by use of a Fourier series analysis technique.[9] The equipment response was also measured. Corrections were then applied to the tube measurements for the equipment response and the fiber-optic faceplate to obtain the MTF of the electron lens of the image tube.

To evaluate the electron-optical system response as a function of electric field at the photocathode, the MTF measurements were

made at several tube-operating voltages over the range of 4 to 18 kV.* These measurements are shown in Fig. 5. As expected, the MTF increases when the applied potential is increased.

The points in Fig. 6 show the variation of spatial frequency with operating voltage for a fixed value of MTF = 0.3. A straight line with a slope of unity was drawn on Fig. 6 corresponding to the theoretical relationship that, for a given MTF, the spatial frequency varies directly with the tube operating potential. The fit of the points to the straight line is reasonable considering the critical focus adjustments mentioned above.

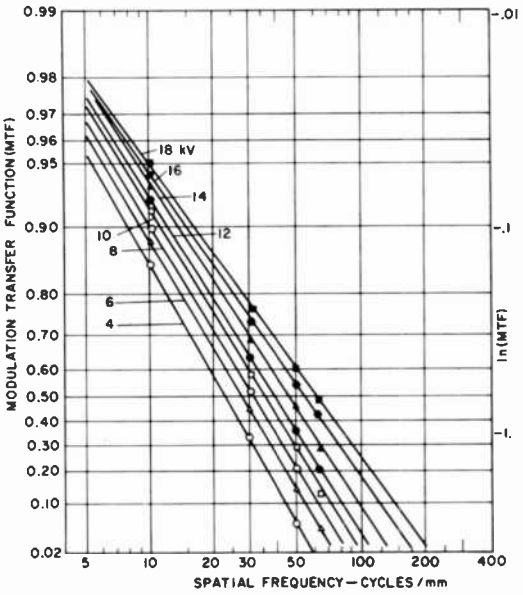

Fig. 5—MTF of the electron optical system of the C21135 image tube for several operating voltages over the range 4 to 18 kV.

To study the MTF of the electron lens of the image tube as a function of initial electron energy, the tube was operated at 6 kV and the test pattern was imaged on the photocathode through several narrow band-pass filters. The measurements for input radiation of 466, 533, 600, and 700 nm are shown in Fig. 7. As expected from theory, the

* From data collected using the RCA electron optics computer program, it was established that an operating potential of 10 kV corresponds to an electric field at the photocathode of 555 V/cm. This information permits the MTF measurements given in this paper to be translated to other similar image tubes, provided the electric field at the photocathode is known.

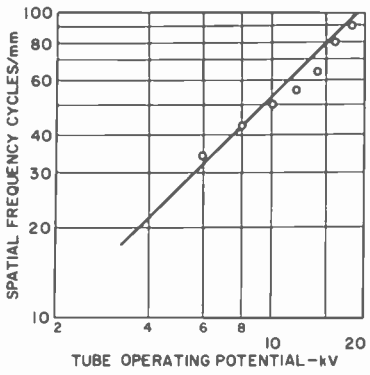

Fig. 6—The variation of spatial frequency with tube operating potential for a fixed value of MTF = 0.3.

MTF is significantly higher for radiation at 700 nm than for radiation at 466 nm.

To translate from monochromatic-input photon energy to electron-emission energy, it is convenient to use the concept of effective elec-

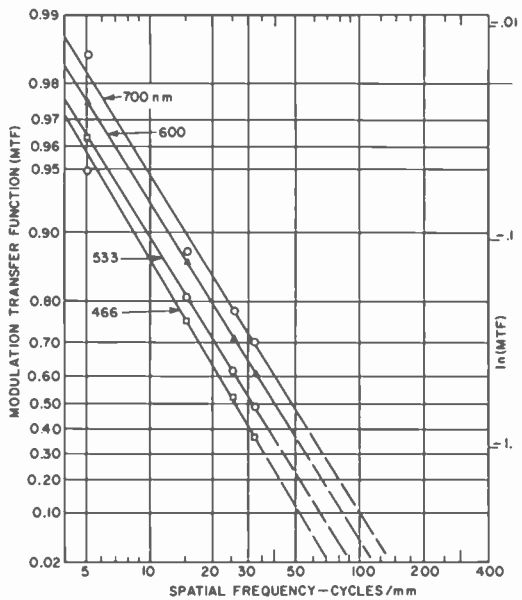

Fig. 7—The MTF of the electron lens versus wavelength of the light image on the photocathode of C21135 image tube operated at 6 kV.

tron-emission energy. The effective electron-emission energy[1] is a weighted average emission energy that characterizes a polyenergetic electron-emission distribution such that the measured MTF curve with polyenergetic electron emission corresponds to the theoretical MTF curve calculated on the basis of monoenergetic electron emission that obeys Lambert's Law.[10] The effective electron-emission energy for a multi-alkali photocathode was measured in an image tube with a uniform electric field. The results are given in a companion paper.[11] Using the results it is possible to transform the MTF response as a function of incident radiant energy to a function of effective electron-emission energy.

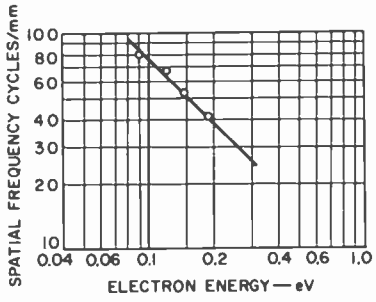

Fig. 8—The variation of spatial frequency versus the effective electron emission energy for a fixed value of MTF = 0.2. The slope is −1.

The variation of spatial frequency as a function of initial effective electron-emission energy for a fixed value of MTF = 0.2 is shown in Fig. 8. This curve with a slope of −1.0 forms the experimental basis for establishing the relationship that, for a fixed value of MTF, the spatial frequency varies inversely with electron emission energy in an image-inverter tube.

Acknowledgments

The author would like to express his appreciation to Professor Showers for advice and encouragement during the course of this work as his dissertation supervisor at the University of Pennsylvania. Also the author is grateful to his immediate supervisors at RCA, R. W. Engstrom and R. E. Simon, for their encouragement, advice, and support to complete this study. Finally, the author wishes to thank E. G. Ramberg for his advice, constructive criticism, and suggestions.

References

[1] L. A. Ezard, *The Modulation Transfer Function Applied to Electrostatic Electron Optical Systems of Image Tubes*, University Microfilms, Ann Arbor, Mich. (1970).

[2] J. W. Goodman, *Introduction to Fourier Optics*, McGraw-Hill Book Co., Inc., New York, N.Y. (1968).

[3] R. L. Lamberts, "Application of Sine-Wave Techniques to Image-Forming Systems," *J.SMPTE*, **71**, p. 635 (Sept. 1962).

[4] R. L. Lamberts, "Measurement of Sine-Wave Response of a Photographic Emulsion," *J. Opt. Soc. Amer.*, **49**, p. 425 (1959).

[5] E. L. O'Neill, *Introduction to Statistical Optics*, Addison-Wesley Pub. Co., Inc., Reading, Mass. (1963).

[6] I. Csorba, "Resolution Limitations of Electromagnetically Focused Image Intensifier Tubes," *RCA Rev.*, **30**, p. 36 (March 1969).

[7] P. Schagen, H. Bruining, and J. C. Francken, "A Simple Electrostatic Electron-Optical System with Only One Voltage," *Phillips Res. Reports*, **7**, p. 119, 1952.

[8] V. K. Zworykin, G. A. Morton, E. G. Ramberg, J. Hillier, and A. W. Vance, *Electron Optics and the Electron Microscope*, John Wiley & Sons, New York, N.Y. (1945).

[9] J. W. Coltman, "The Specification of Imaging Properties by Response to a Sine Wave Input," *J. Opt. Soc. Amer.*, **44**, p. 468 (1954).

[10] V. K. Zworykin and E. G. Ramberg, *Photoelectricity*, John Wiley & Sons, Inc., New York, N.Y. (1949).

[11] L. A. Ezard, "Measurement of Effective Photoelectron Emission Energy," *RCA Rev.*, **36**, p. 000, Dec. 1975 (this issue).

Ultra-Thin RF Silicon Transistors With a Copper-Plated Heat Sink

H. S. Veloric, A. Presser, and F. J. Wozniak

RCA Laboratories, Princeton, N.J. 08540

Abstract—A new procedure has been developed for fabricating ultra-thin silicon transistors equipped with a plated-copper heat sink. The process replaces most of the thermally lossy silicon collector with copper, thus reducing the thermal resistance by as much as 50%. 12–13 μm thick silicon transistor wafers are routinely processed directly on copper. Individual transistors are separated by wire sawing through the silicon and copper. Multi-cell devices are stress-relieved by the process of sawing through the silicon to define each cell. Transistors fabricated with this technology show thermal resistance and rf performance superior to that of conventional structures when operated in amplifiers in the 3 to 5 GHz range. Amplifiers with standard three-cell TA-8407 transistors deliver typically a cw power output of 5.5 watts at 3.5 GHz; an amplifier with the plated-heat-sink transistor delivers more than 7 watts for the same power input.

1. Introduction

Because microwave power transistors operate at high power densities, careful thermal management is required to minimize the pellet operating temperature and to optimize the performance of the transistors. The operating temperature is a function of the pellet geometry, the amplifier circuit, and the thermal path between the collector junction and the heat sink. One design modification that improves thermal resistance is to increase the number of thermally isolated collector cells while holding the collector–base junction area constant. This approach, given equal emitter edge and base area, results in longer pel-

lets, additional bond-wire interconnections, and larger packages. The approach described here reduces the thermal resistance to the heat sink by replacing most of the collector silicon with copper.

For mechanical reasons, a practical silicon transistor chip is at least 75 μm thick. The thermal resistance in this silicon is approximately $\frac{2}{3}$ of the total for a eutectic-mounted transistor on a BeO heat sink. By use of plated copper as a "handle," the silicon thickness can be reduced to 13 μm. This technique has been applied to an rf power transistor, the TA-8407, resulting in improved thermal and electrical performance when compared to that of the conventional structure.

Copper-heat-sink technology has been used for many years to improve the performance of various microwave diodes. Impatt diodes, for example, made by this process operate as amplifiers and oscillators at frequencies up to 60 GHz.[1–3] The technique consists of epitaxially growing a multilayer silicon structure in which the silicon "handle" can be accurately etched off after a copper heat sink is plated on the wafer face. In addition, the diode contact areas can be grown with sufficient doping to ensure low-resistance contacts. This technology is not directly applicable to bipolar transistors because of the complexity of transistor processing. For example, the multilayer epitaxial wafer cannot be used for transistor processing, because the surface of the grown layer is not sufficiently flat and free of imperfections to permit fine-line definition. In addition, a Cu "handle" on the top surface is not possible since numerous bond-wire interconnects are required for the emitter and base contacts.

Copper-heat-sink technology, as applied to rf transistors, requires precise etch-thinning of the completed transistor wafer, adherent ohmic contacts to the etched collector layer, adherent plating to the metalized collector, separation of the individual transistors, and stress relief for the Si–Cu interface. A chemical–mechanical etch procedure controls the silicon thickness within 2.5 μm over the entire wafer. A low-temperature metalization and copper-plating process give good adhesion and a satisfactory ohmic contact. The individual transistors are separated and stress relieved with a wire saw.

The metalization system is Cr–Pd–Cu–Au. The Cr adheres to silicon and makes a satisfactory contact, Pd is a barrier to keep Cu from diffusing into silicon. Cu has excellent thermal and electrical conductivity and is easy to plate; gold prevents the Cu from oxidizing and facilitates soldering the transistor into packages.

In the next section, the process for fabricating ultra-thin silicon transistors on copper is described. Contact resistance problems are then discussed briefly and finally the performance of the resulting copper-backed TA-8407 transistor is described.

2. Copper Heat-Sink Fabrication Procedure

The heat-sink fabrication proceeds as illustrated in Figs. 1a and 1b. In the first operation, a completed transistor wafer, preferably with gold metalization, is mounted face down on a sapphire disk with quartz wax. This wax is strong enough to hold the wafer during precision back grinding to a thickness of 75 μm while maintaining the wafer faces parallel within 2.5 μm. Since the quartz wax is not compatible with subsequent processing, it is removed after grinding and the wafer is remounted with a soft wax.

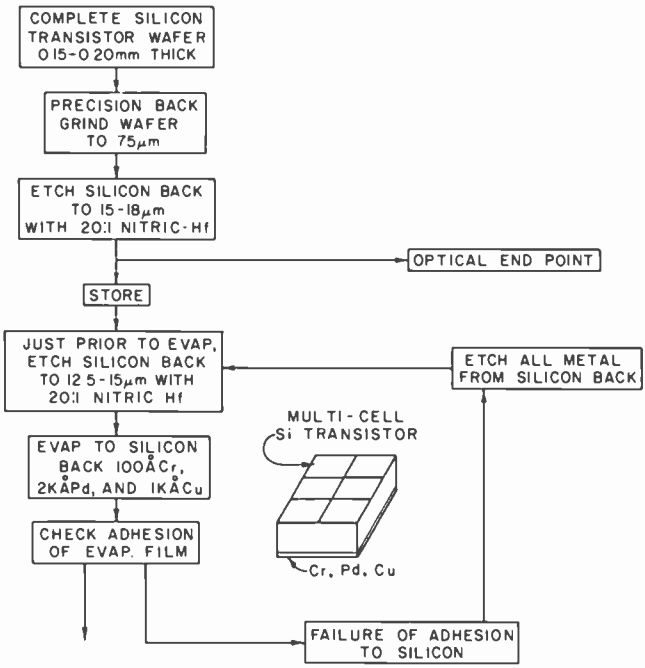

Fig. 1(a)—Process flow chart for preparation of wafer for copper-heat-sink transistors.

The 75 μm wafer is now etch thinned to a final thickness of 12.7 to 14 μm using the process developed by Stoller.[4] This process utilizes nitrogen bubbled from the bottom of the etching chamber to impinge on the float-mounted wafer to ensure uniform, smooth, blemish-free surfaces. The apparatus permits observation of the color of transmitted light through the wafer during the etching process. With care and experience, the final thickness can be controlled within 2.5 μm, al-

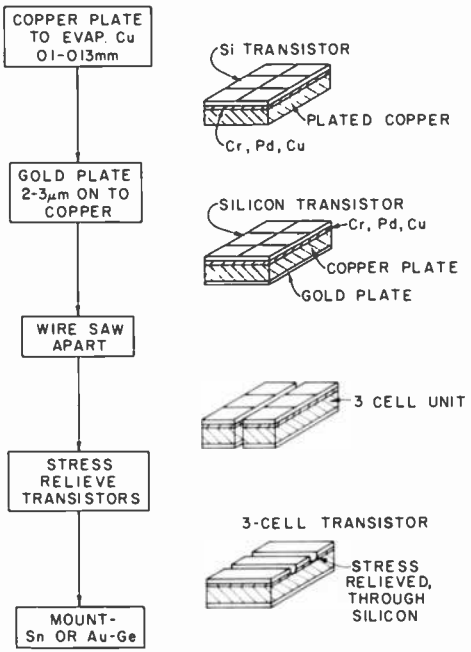

Fig. 1(b)—Process flow chart for copper-heat-sink transistors.

though within 100 μm of the edge the silicon is thinner by 5–7.6 μm. Fig. 2 shows a thinned TA-8407 transistor wafer illuminated by light transmitted through the silicon. The uniform thickness results in uniform light transmission. The light variation at the edges of the figure are caused by the difficulty of photographing the transmitted red light.

The thin wafer, still wax mounted to the sapphire disk, is etch-cleaned with 20:1 nitric HF prior to Cr–Pd–Cu metalization. Careful control of the substrate temperature is required during metalization since the wax melts at 75°C. The metals are electron-gun evaporated in several short charges to minimize substrate heating. The thickness is continuously monitored during the deposition with an quartz crystal oscillator. The film is checked for adhesion; a satisfactory film does not peel, but breaks at the check point.

The metalized wax-mounted wafer is now ready for back plating with 100 μm of copper and 3 μm of gold. At current density of 30 mA/cm^2, the copper deposits at a rate of 30 μm/hour. After copper plating, 3 μm of gold are deposited in 15 minutes with a current density

of 3 mA/cm^2. The pellets can now be separated from the demounted wafer with a wire saw using a diamond slurry as the cutting medium.

A wire saw is used to define pellet arrays in laboratory use because of its flexibility; however, it is a slow and thus a poor production process. We have developed a batch separation procedure that consists of selective plating of the Au–Cu heat sink to define pellet areas. The batch separation procedure utilizes Riston "roll on" resist as a plating stop in the separation grids. The individual copper islands are aligned to the transistor pattern on the top surface, defined by the 20-μm-thick resist, and plated up with the previously described pro-

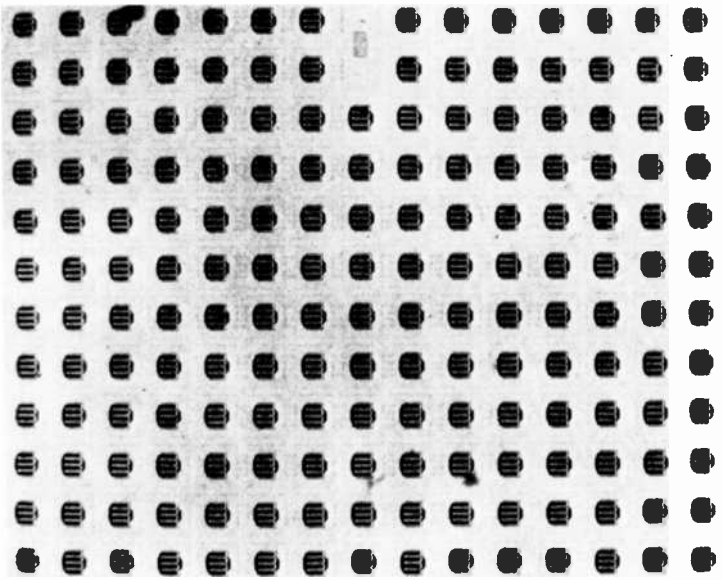

Fig. 2.—Thinned TA-8407 transistor wafer illuminated by transmitted light.

cess. By use of the defined Cu–Au islands as the acid resist, the Cu–Pd–Cr–Si–SiO_2 layer in the grid can be sequentially etched to define the individual transistors. Fig. 3 shows an array of Cu–Au heat sinks defined with a TA-8407 grid mask. The 10-μm-thick islands are on 0.4 mm centers with 50 μm grid spacing.

Because there is a large thermal mismatch between Cu and silicon, it is desirable to keep the silicon–copper chip small. This minimizes stress induced during the high-temperature assembly process. Fig. 4 shows a 3-cell TA-8407, stress relieved by cutting through the silicon

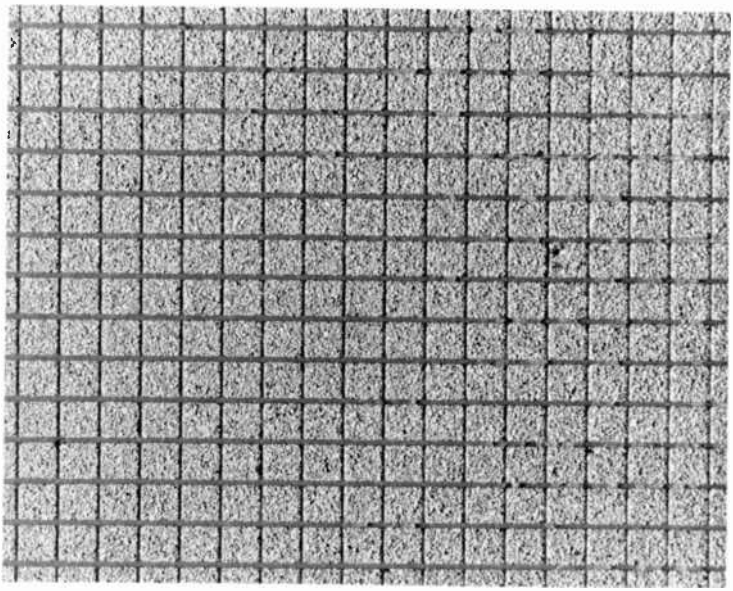

Fig. 3.—An array of Cu–Au heat sinks on 0.4 mm center.

at each cell site and ready for soldering into an assembly. The transistors are soldered into packages with Sn at 220°C. If higher temperature capability is required, Au–Ge eutectic solder can be used at 360°C.

3. Silicon Metal Adhesion and Contact Resistance

Two important requirements for the metal–silicon interface are sufficient adhesion for reliable mechanical strength and a low contact resistance. Because of process constraints, conventional transistor low-resistance alloy contacts such as Au–Sb–Si eutectic or Pd–Si cannot be fabricated. The wax-mounted silicon wafer can only be heated to 75°C, thus restricting the metalization to non-alloy contact systems such as Ti or Cr–Cu. Since initial tests with the substrate tempera-

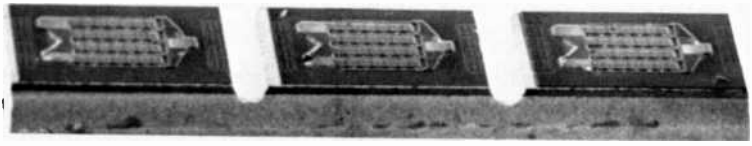

Fig. 4.—A stress-relieved copper-heat-sink three-cell TA-8407 transistor.

ture at 50°C show Cr adhesion superior to Ti, Cr is selected for complete evaluation.

Forty Cr–Pd–Cu-backed transistors have been assembled in HF-46 microwave packages with Au–Ge eutectic. These devices have been temperature-cycled from −65°C to 150°C over 100 times without any failures. In addition, Cr–Pd–Cu-backed transistors that are tested to destruction fail in the silicon, not at the Cu–Si interface.

Several investigators have evaluated the contact resistance of Ti and Cr to low-resistivity epitaxial silicon substrates. Terry[5] reports a specific contact resistance of 300 to 400 $\times 10^{-6}$ ohm-cm^2 for Cr or Ti on 0.01 ohm-cm silicon and 10×10^{-6} ohm-cm^2 for Pt–Si on the same substrate. The contact resistance for the three metals is reduced to 2–3 $\times 10^{-6}$ ohm-cm^2 when the Si resistivity is decreased to 10^{-3} ohm-cm. These values are comparable to those achieved at microwave frequencies by Chiang[6] and Denlinger for contacts to 10^{-3} ohm-cm silicon for Pd–Si, Ti, and Cr contacts.

We have measured the series resistance of several 2.5×10^{-2} mm^2 TA-8407 collector–base diodes fabricated on 0.01 and 0.002 ohm-cm substrates. With one ampere of forward current, the total voltage drop for a standard eutectic-mounted collector–base diode is one volt. With this voltage as a reference, an additional voltage drop is equal to the product of series resistance and current. The measured series resistance is 1 to 2 ohms for a single cell TA-8407 with Cr contacts to 0.02 ohm-cm collector substrate. For the identical contact, if the collector resistivity is decreased to 0.002 ohm-cm, the series resistance is reduced to under 0.1 ohm.

Two-point probe spreading-resistance measurements have been made on several Cr-contact transistors to evaluate the resistance-doping profile and thus establish the high-resistance region. This tool is used routinely to evaluate doping profiles and P–N junctions.[7] In addition, we have used the probe to detect a resistance increase at the contact, which confirms the rectifying characteristic of the Cr–Si interface.

Since the two-point probe reads the resistance of a small volume; with an appropriate cross section, the resistance profile can be accurately defined. Fig. 5 shows two cross sections of the boundary between the Cr–Cu and silicon. For the cross section where the probe interrogates the copper first, a low resistivity is measured when the probes are on the copper. Even if there is a rectifying boundary at the interface, the resistivity increases rapidly and smoothly when the probes are moved onto the silicon. When the probe moves from Si onto Cu, the resistance change at the interface is determined by the contact resistance. Case 2 in Fig. 5 shows the resistance change with

no contact resistance, a smooth decrease as the resistivity of Cu is detected by the probes. If the interface is rectifying, as the probes approach the interface, the mobile carriers are depleted and the resistance increases until the probes move onto the copper. This resistance profile is Case 3 in Fig. 5.

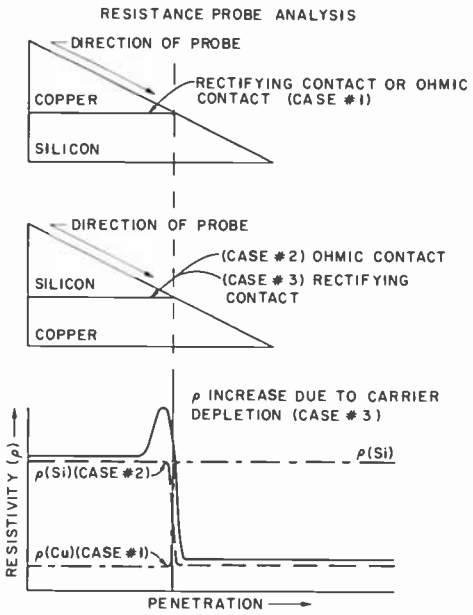

Fig. 5.—Resistance probe profile of a metal-silicon interface.

All three cases were investigated using an 8-μm diameter probe with 100-μm spacing. Fig. 6 shows the spreading resistance data for the probe moving from 0.01 ohm-cm Si to Cu, Cu to 0.01 ohm-cm Si, and 0.002 ohm-cm Si to Cu. A high resistance region is measured only for the 0.01 ohm-cm Si to Cu probe, consistent with our previous analysis. Thus, the rectifying contact at the Cr to 0.01 ohm-cm Si interface and the ohmic contact at the Cr to 0.002 ohm-cm Si boundary is directly observed. Because of the fragile nature of the small sample, however, larger sections should be evaluated to assess the full capabilities of the technique.

Since it is desirable to apply copper heat sinks to standard transistors with 0.01 ohm-cm substrates directly from the production line, several sintered contacts have been evaluated to reduce the contact resistance. The contact resistance on a thin transistor wafer is difficult to reduce since any alloy procedure must be done below the Al-Si

eutectic temperature of 577°C. This constraint eliminates ohmic contacts, such as Pt–Si where sintering is done at 600°C or ion beam doping of Si where anneal-activation occurs in excess of 700°C.

Ohmic contacts to diffused emitter and base regions have been reported by J. Banfield[8] with Pd–Si sintered at 350°C. Several complete transistor wafers were thinned to 13 μm, and Pd was deposited on the collector and sintered at 300°C. Because of thermal stress, only one-quarter wafers are used. The collector contact resistance for transistors separated from these wafers is comparable to that measured for non-sintered Cr–Si contacts.

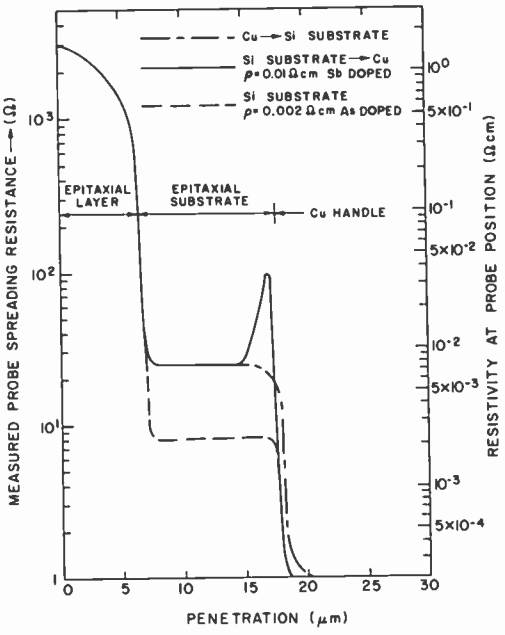

Fig. 6.—Resistance probe measurements of copper-heat-sink TA-8407.

All of the Cu-backed transistors evaluated at high frequency are processed from conventional 0.01 ohm-cm substrates; hence each cell has a contact resistance of 1–2 ohms. This resistance does not introduce appreciable loss up to frequencies of 5 GHz in the 28-volt amplifiers used to evaluate these devices. Additional work is required to establish the significance of the contact resistance at rf frequencies.

4. Performance of Copper-Backed RF Transistors

The plated-heat-sink process has been used to copper-back several

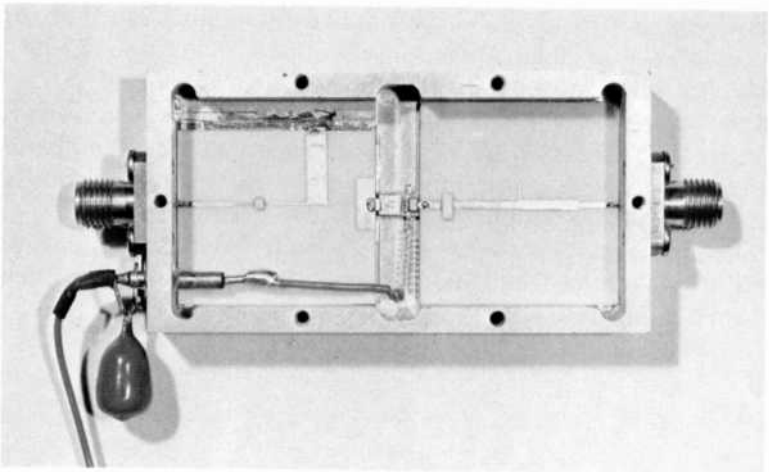

Fig. 7.—3–3.5 GHz test amplifier.

TA-8407 transistor wafers. The specific wafer runs are optimized for class-C operation in the 3-to 4-GHz frequency range.

The performance of a conventional thickness three-cell pellet and a similar 13-μm-thick pellet from the same run backed with a 75-μm plated copper heat sink are evaluated in separate but identical common-base class-C amplifiers. Fig. 7 is a photograph of one of the test amplifiers. The microstrip circuitry is fabricated on alumina boards

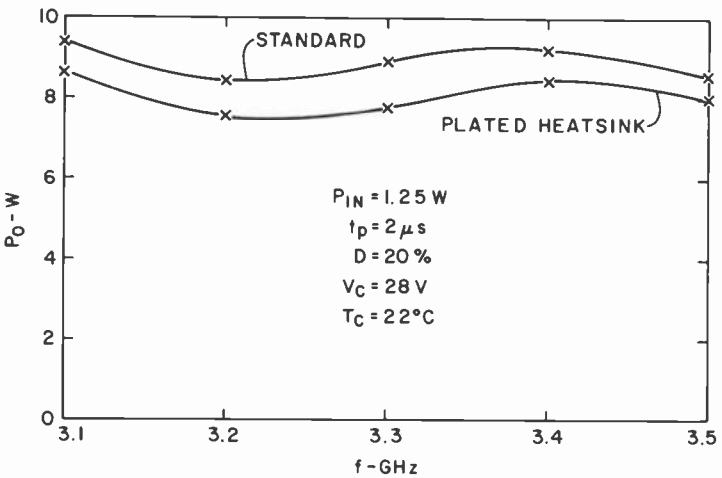

Fig. 8.—Output power for copper heat sink and conventional three-cell TA-8407 amplifiers with $t_p = 2\mu s$.

and the transistor pellets are mounted on tuned BeO carriers. The two amplifiers are first tuned for uniform gain over the 3.1-to 3.5-GHz frequency range when driven with a 2-μs pulsed signal at 20% duty cycle and a peak power of 1.25 watts. The measured peak power outputs of the two amplifiers at this operating condition are similar and are plotted in Fig. 8. Heating effects are absent and the gains track within 0.4 dB at any frequency in the band. When operated with a 1.5-ms-long pulse at 20% duty cycle and a 1.25-watt peak-power input, the observed average power output is lower when compared to the power output at 2-μs operation. This power drop is caused by thermal effects and is significantly smaller for the plated heat-sink amplifier. The average power output ratios P_0 (1.5 ms)/P_0 (2 μs) are plotted in Fig. 9 for both amplifiers. For the standard am-

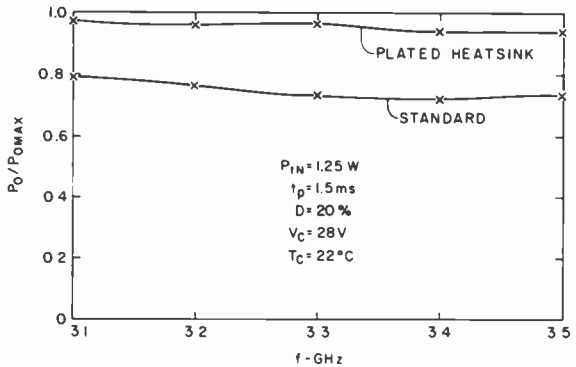

Fig. 9.—Output power ratio P_0 (1.5 ms)/P_0 (2 μs) for copper-heat-sink and conventional three-cell TA-8407 amplifier with t_p = 1.5 ms.

plifier, this ratio varies between 0.72 and 0.79 (corresponding to a 1.0 to 1.4 dB power drop) over the frequency range. In contrast, for the copper-backed pellet amplifier, the power drop is only 0.1 to 0.3 dB.

For pulsed operation, the output-power drop and the phase variations during the on time are important in many applications. Table 1 shows the comparative results obtained at 3.3 GHz from the two test amplifiers for three operating conditions; 2-μs pulsed (reference), 1.5-ms pulsed, and cw. Listed are the peak-power output P_0 at the end of the pulse, the power drop Δ in dB (the leading edge to trailing edge power ratio), and the phase settling ϕ in degrees (the difference of phase during the pulse).

The comparative tests show clearly the advantages of the plated-heat-sink transistor. With a 2-μs pulse, the amplifiers have compara-

ble gain and output power; as the pulse length increases to 1.5 ms, the gain and output power for the Cu-heat-sink amplifier is almost 20% higher than the conventional one. Under cw conditions, the Cu-heat-sink amplifier has over 25% more gain and power than the conventional structure. In addition to higher output power and gain, the hot-spot thermal resistance for the copper-backed TA-8407 is 1/3 less, resulting in lower junction temperature for identical operating conditions and thus improved power-density capability.

Table I—Comparison of Three-Cell Amplifiers Using Standard and Plated-Heat-Sink Transistors (TA-8407) for Pulsed (20% Duty Cycle) and CW Operation (P_o = Output Power, Δ = Pulse Droop, and ϕ = Pulse Settling)

	T_p = 2μs			T_p = 1.5 ms			CW		Thermal Resistance
Transistors	P_o (W)	ϕ (°)	Δ (dB)	P_o (W)	ϕ (°)	Δ (dB)	P_o (W)	Δ (dB)	(°C/W)
Standard	8.3	0.5	0	5.6	14	1.7	5.2	2.0	6.0
Plated-Heat-Sink	8.3	0.5	0	7.4	9	0.4	7.2	0.6	4.2

5. Conclusions

This new fabrication procedure permits the processing of 13-μm-thick silicon transistors with an integral copper heat sink. The procedure has been applied to one- and three-cell TA-8407 transistor chips and is generally applicable to any size array. Amplifiers made with these transistors show less pulse droop and higher output power than amplifiers made with conventional structures. The improved thermal resistance extends the power density capability of a given rf transistor design, thus resulting in lower operating temperature and improved reliability.

A direct comparison is made for TA-8407 transistors from an identical lot but different wafers. The hot spot thermal resistance is 50 % less for a single cell and 30% less for a three-cell Cu-heat-sink transistor when compared to the conventional structure. Even though the performance is comparable for 2-μs pulsed signals, the devices with the lower thermal resistance show superior performance when evaluated for 1.5 ms pulse and cw performance.

In a cw class C amplifier at 3 GHz, a three-cell copper-backed TA-8407 transistor delivers over 25% more power and gain than a conventional transistor structure.

Acknowledgments

The authors are grateful to R. D'Aiello for numerous discussions and the two-point probe results. F. Duigon gave excellent technical support in applying diode processing to silicon transistors. The transistors and amplifiers were assembled by E. Mykietyn and J. Brown. The authors are glad to acknowledge valuable discussions with E. F. Belohoubek and F. N. Sechi.

References:

[1] C. P. Wen, K. P. Weller, and A. F. Young, "Multilayer Vapor-Phase Epitaxial Silicon Millimeter-Wave IMPATT Diodes," *IEEE Trans. Electron Devices*, **ED-19**, p. 890, July 1972.

[2] K. P. Weller, C. P. Wen, A. F. Young, and A. B. Dreeben, "Millimeter-Wave GaAs Avalanche Oscillator," *Proc. High Frequency Generation and Amplification Conf.*, Cornell University, 1971, pp. 191–198.

[3] G. A. Swartz, Y. S. Chiang, C. P. Wen, and A. Gonzales, "Performance of P-Type Epitaxial Silicon Millimeter-Wave IMPATT Diodes," *IEEE Trans. Electron Devices*, Feb. 1974.

[4] A. I. Stoller, R. F. Speers, and S. Opresko, "A New Technique for Etch Thinning Silicon Wafers," *RCA Review*, **31**, p. 265, 1970.

[5] L. E. Terry and R. W. Wilson, "Metalization Systems for Silicon Integrated Circuits," *Proc. IEEE*, **57**, No. 9, p. 1380, Sept. 1969.

[6] Y. S. Chiang, E. J. Denlinger, and C. P. Wen, "Contact Resistance of Metal-Silicon System at Microwave Frequencies," to be published in *RCA Review*.

[7] N. Goldsmith, R. V. D'Aiello, and R. A. Sunshine, "Two Point Probe Spreading Resistance," NBS Publication 400-10.

[8] J. Banfield, private communication.

Wideband Signal Recording on Film Using (AlGa)As CW Injection Lasers

J. E. Roddy

RCA Advanced Technology Laboratories, Camden, N. J.

Abstract—CW injection lasers have demonstrated excellent performance when used in a wideband film recorder to replace a gas laser and its external light modulator. The injection lasers have been internally modulated from 1 to 200 MHz (±2 dB) and film recordings of signal frequencies up to 100 MHz (160 cycles/mm) have been made. The lasers are double-heterojunction, (AlGa)As devices emitting up to 10 mW at 710 nm when operated at 77°K. Comparisons are made between injection laser performance and data taken previously on an argon laser recorder.

1. Introduction

Present wideband film recorders use gas lasers and external light modulators. While impressive performance has been achieved, these components are bulky, mechanically elaborate, expensive, and require considerable power. If laser recording is to be used for other than a few highly specialized data-capture applications, the component costs must be reduced and reliance upon high-precision parts must be minimized. Semiconductor lasers have recently become an attractive record-signal source because they can be internally modulated at very high rates and are potentially inexpensive. These lasers are small, rugged, reliable, and require only a few watts at a few volts for operation.

Two developments have made the use of injection lasers in wideband recording particularly worth considering at this time. First, laser diodes that emit continuously at wavelengths below 720 nm in excess of 5 mW have been fabricated.[1] Second, extended-red-sensitive holographic films that can be exposed by wavelengths as long as 720 nm have been developed by Kodak and Agfa-Gevaert. Dry silver film sensitive to 700 nm has also become available.*

This paper describes wideband modulation and film-recording experiments made with semiconductor injection lasers. Comparisons

* 3M Company.

are made to data taken previously on an argon laser recorder that was modified to accept the semiconductor laser source.

The laser diodes used for the experiments are stripe contact, double heterojunction (AlGa)As.† Five to ten mW at 710 nm was achieved when the diodes were operated at 77°K.

Cryogenic cooling was required to obtain sufficient light power at a wavelength to which presently available high-resolution films are sensitive. The quantum efficiency at room temperature drops significantly in (AlGa)As diodes for emission wavelengths shorter than about 800 nm.[2] However, for these shorter wavelengths, the quantum efficiency can be greatly improved by decreasing the diode temperature. For a 710-nm wavelength, cw lasing at adequate power levels is attainable with liquid nitrogen as a coolant (77°K).

2. Component and System Requirements

2.1 Gas Laser Recorder

The original argon laser recorder, which has since been modified to accommodate the laser-diode source, is shown in Fig. 1. The output of an argon laser (approximately 1 W, all lines) is passed through an electro-optic light modulator where the beam intensity is modulated by the input-signal information. The modulated beam is expanded to fill the imaging lens and focused to a diffraction-limited spot on the film. A polygon rotating mirror, located within the focus of the imaging lens, deflects the modulated spot in an arc at a rate of 63,500 cm/sec. Silver halide film is transported past the scanning laser beam and is exposed by it along transverse tracks in a format similar to that of rotary-head video-tape recording. After the film is developed, it is transported past the scanning beam, which once again becomes intensity modulated, this time by the transmittance variations of the film. The light is collected using appropriate optics and is photodetected, yielding a reproduction of the original signal.

For injection-laser recording, the gas laser and external light modulator were replaced by an injection laser and its cooling structure. The beam expander was removed and an $f/2$ collection lens was installed to collimate the output of the laser diode.

2.2 Laser-Diode Source

A diagram of the double-heterojunction (AlGa)As diode used is shown in Fig. 2. A 13-μm-wide stripe contact, which runs the length

† Supplied by RCA Laboratories, Princeton, N. J.

of the cavity (320 μm), restricts the current flow to a small volume. The actual emitting region on the output facet is approximately 20 μm wide by 0.5 μm high. The stripe contact keeps the threshold current low and improves cooling, allowing a high continuous output for a given emitting facet length. The data reported here was taken using a diode that appeared to be particularly suited for wideband signal recording application. The characteristic curve of this diode is shown in Fig. 3. As can be seen from the figure, the threshold current is about 420 mA, above which the light output increases linearly with

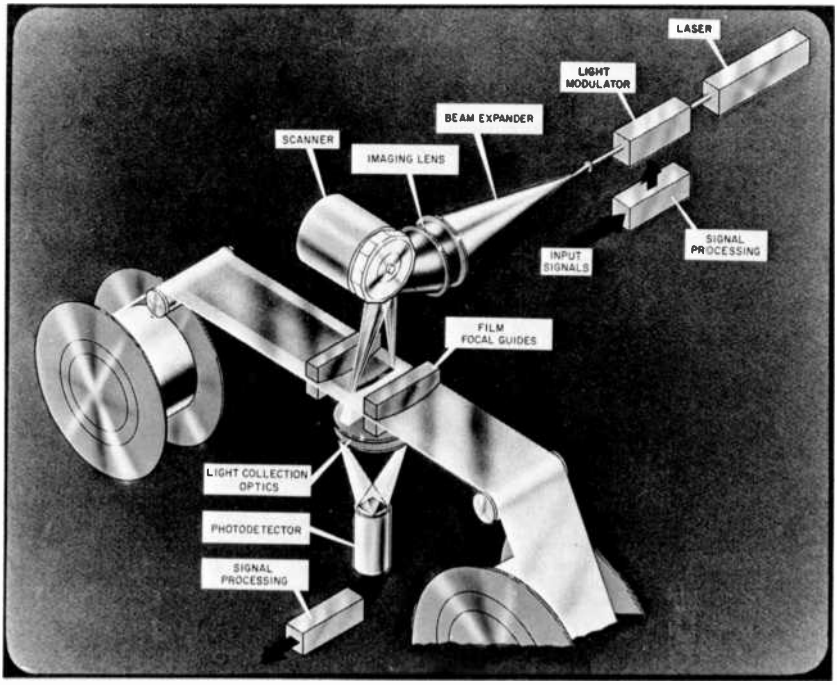

Fig. 1—Wideband laser recorder.

input current. The diode light output can be directly modulated by controlling its forward bias current. For a continuous analog recorder, it is desirable to bias the diode into the lasing region with direct current and vary the light about this bias value by applying a high-frequency signal current. For this diode, acceptable recordings were obtained using a 450-mA bias and a 75-mA p-p signal current. The resultant contrast ratio measured in the record spot was 25:1. The percent modulation was 92%.

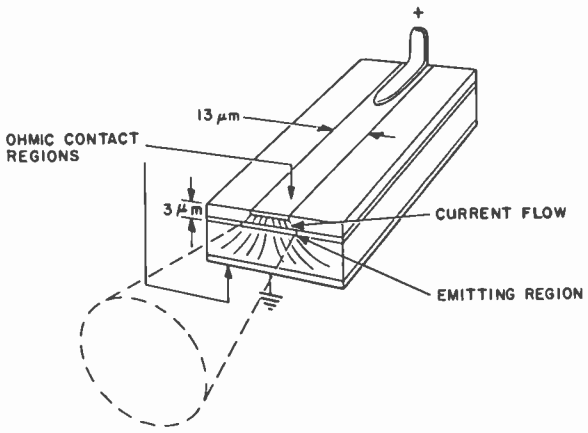

Fig. 2—Stripe contact diode.

The diodes were supplied on individual mounts that were installed in a vacuum dewar for testing as shown in Fig. 4. Fig. 5 is a view of the diode mount through the dewar window. A broadband electrical drive signal and bias network was fabricated on a hybrid board and installed in the dewar close to the diode mount.

2.3 Light Power Requirements

The spectral sensitivity curve for AGFA 10E75 film is shown in Fig. 6. To expose this film with a 710-nm source to a density of 1.0 re-

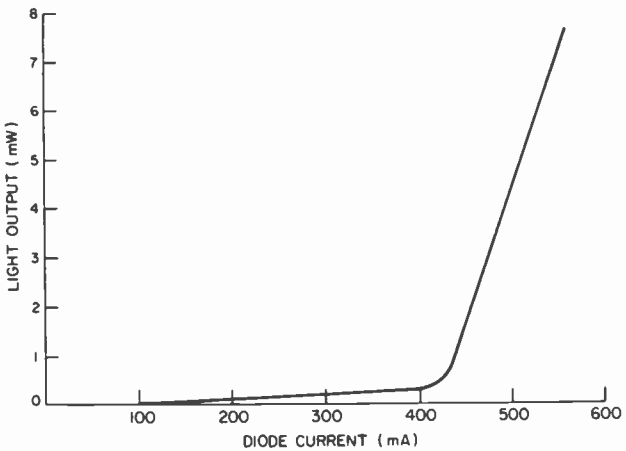

Fig. 3—Power output versus current.

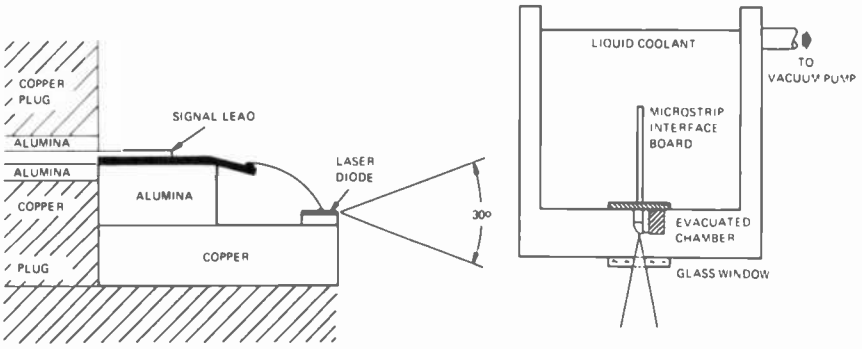

Fig. 4—Cooling and mounting structure.

quires an energy density of 50 ergs/cm.^{2} The laser power required in the record spot is given by

$$P = KWV,$$

where K is the film sensitivity (50 ergs/cm^2), W is the track width, and V is the scan velocity.

For a track width of 25 μm and a scan velocity of 63,500 cm/sec, a record spot power of 0.8 mW is required. The transmission and aperturing losses of the recorder are about 5:1. Therefore, a 4-mW peak output from the diode is sufficient to produce the required maximum density of 1.

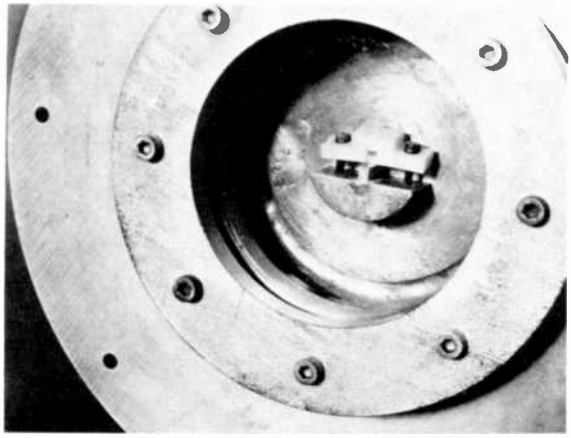

Fig. 5—Diode mounted in dewar.

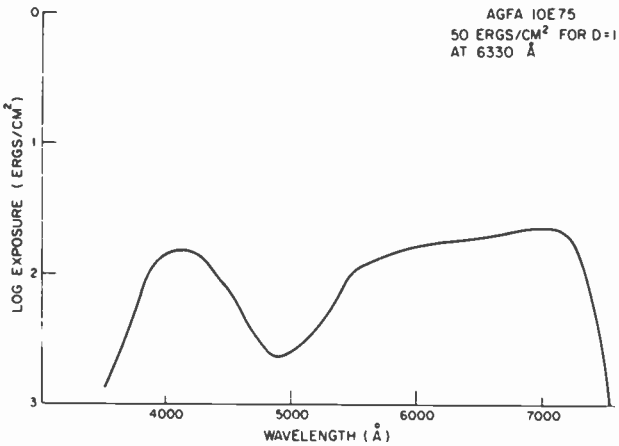

Fig. 6—Sensitivity curve for AGFA 10E75 film (exposure of 50 ergs/cm for $D = 1$ and 6300 Å).

2.4 Optical System

The basic optical system is shown in Fig. 7. The design is dependent upon the emitted beam pattern which, due to multimoding effects, can be quite different for diodes of the same type. A reasonably fast spherical lens is needed to collect and collimate the divergent fan-shaped diode beam into a rectangular beam of suitable aspect ratio. If necessary, cylindrical lenses in the form of a beam expander or reducer can be used to modify the aspect ratio. This collimated rectangular beam is then focused onto the film by an imaging lens with the scanning mirror forming the limiting aperture. The rectangular format of

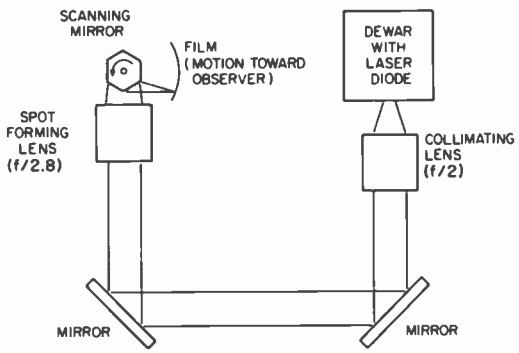

Fig. 7—Laser-diode recorder optics.

the laser diode beam has proved to be particularly efficient in illuminating polygon scanners. A summary of system parameters is as follows:

Collection lens—$f/2$, 10 cm focal length, collects 72% of the diode emission.
Imaging lens—$f/2.8$, 15 cm focal length.
Scanning mirror—hexagon.
Spot velocity—63,500 cm/s
Film AGFA 10E75, K = 50 erg/cm^2 for D = 1 at 710 nm
Across-track spot size (track width)—25 μm.
Along-track spot size—8 μm.
Required laser power (peak) = 4 mW (for continuous recording, twice this power (8 mW) is required, since two hexagon mirrors must be illuminated.)
Electrical drive requirements—450 mA dc, 75 mA p-p ac.
Calculated record MTF at 710 nm—250 lp/mm limiting, 100 lp/mm at 50% MTF.
Electrical Bandwidth—63.5 MHz at the 50% record MTF point.

The size of the record spot is determined by the combination of the imaging lens and the scanner mirror facet. Both the record spot velocity and the emission wavelength affect the signal bandwidth at 50% MTF.[3]

3. Experimental Results

3.1 Beam Patterns and Spot Size versus Current

The beam divergence of the laser diode used in these tests measured 32° to the half-intensity points in the plane perpendicular to the lasing junction (along track direction). The divergence in the plane of the lasing junction (across track direction) varies from 5° to 15° (full width to the nulls) with drive current. When imaged through the recorder optical system, the spot size in the track width (across track direction) varies with this beam divergence. Fig. 8 shows the beam pattern at three current levels 5 cm from the diode. Fig. 9 shows the record spot at approximately the same current levels. A 2.5 × 1.0 cm aperture was placed before the imaging lens to simulate one facet of the scanning mirror. The data in these photographs is summarized in Table 1.

The actual track widths recorded on AGFA film were included for

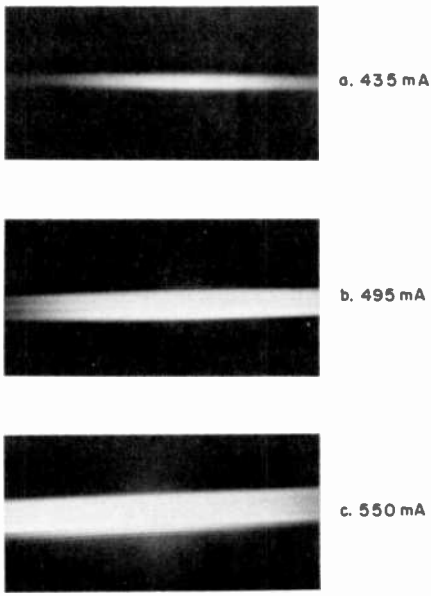

Fig. 8—Laser-diode beam pattern at various current levels.

comparison. Basically this data, along with the diode characteristic shown in Fig. 3, indicates that over the drive current range extending from 435 to 550 mA, the diode output power increases 10 to 1 and the track width increases by 3 to 1. Therefore, the gain in useful record spot power for a constant spot width is about 3.3 to 1 instead of 10 to 1 as might be expected from the characteristic curve. Slightly above threshold, the laser appears to be in single-mode operation. The effect of multimoding on the beam pattern at higher drive current levels is apparent in Fig. 8. The variations in intensity in the beam pattern at 495 mA are noted in Fig. 10. At this current level, the laser beam is linearly polarized greater than 100:1, with the optical E-vector in the plane of the junction. Fig. 11 demonstrates the diffraction-

Table 1

Current (mA)	Across-Track Beam Divergence	Spot Size on Polaroid Film (μm)	Recorded Track Width at 63,500 cm/s On AGFA 10E75 Film (μm)
435	5.4°	8.8 x 25	18
495	10.7°	8.8 x 46	38
550	14.3°	11 x 62	50 (estimated)

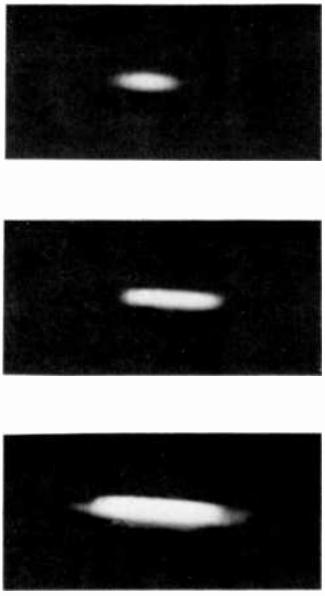

Fig. 9—Simulated record spot at various current levels.

limited spot quality obtainable. The $[(\sin x)/x]^2$ intensity pattern characteristic of a uniformly illuminated rectangular aperture is distinctly visible.

The track width variations noted above are not expected to be a serious problem in a signal recorder. However, aperturing would be required to more closely control spot growth in direct image recorders,

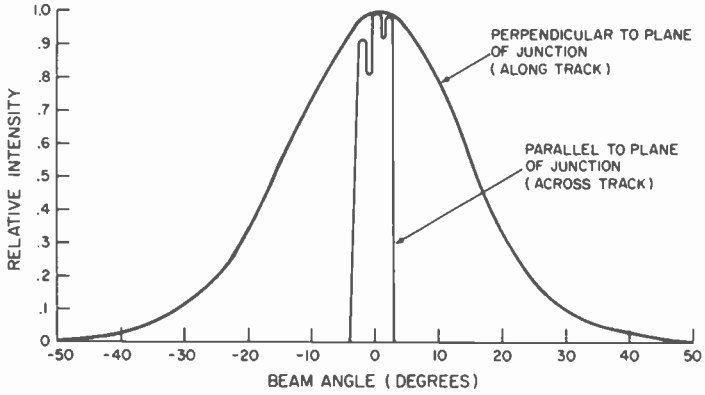

Fig. 10—Beam profiles at 495 mA.

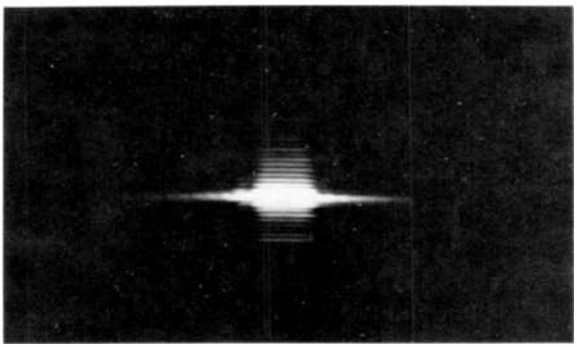

Fig. 11—Diffraction-limited record spot.

since it is generally desirable to have the same MTF in both the along-track and across-track directions.

3.2 Frequency Response, Distortion, and Noise

The test setup for frequency response, distortion, and noise data is shown in Fig. 12. The modulated output of the injection laser is shown in Fig. 13a as detected over a frequency range extending from 1 to 200 MHz. For comparison, the wideband sweep from 1 to 200 MHz of an externally modulated argon laser is shown in Fig. 13b. An electro-optic light modulator developed by RCA in 1969 was used,

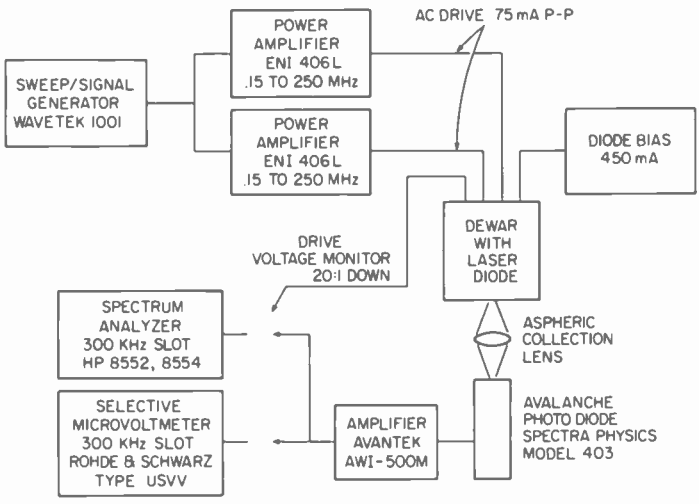

Fig. 12—Frequency response, noise, and distortion test setup.

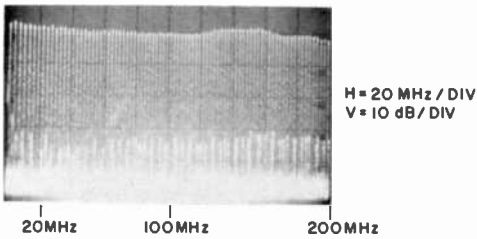

a. LASER DIODE SWEEP RESPONSE

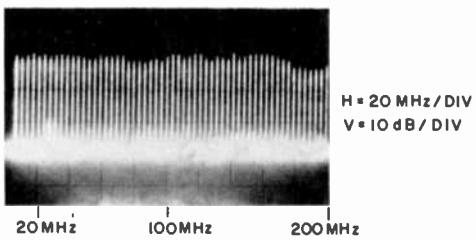

b. ARGON LASER / LIGHT MODULATOR SWEEP RESPONSE

Fig. 13—Sweep response comparison.

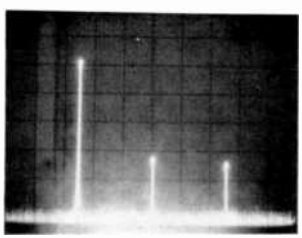

a. 50MHz DRIVE SIGNAL

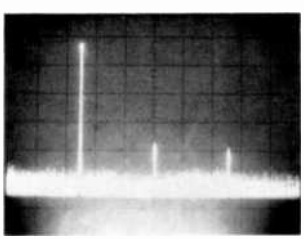

b. 50 MHz DETECTED SIGNAL

Fig. 14—Harmonic distortion test.

achieving a contrast ratio of 5-to-1 for a drive-signal amplitude of 44 V p-p, across a 27-ohm impedance.[5]

The harmonic distortion was quite sensitive to bias current for the diode sample used. However, other diodes did not exhibit this sensitivity. Figs. 14a and b show a 50-MHz drive signal and the detected signal, respectively, for 450-mA bias current and 75 mA p-p drive. For the detected signal, the second harmonic was 35 dB below the fundamental and the third harmonic was 37 dB down.

Signal-to-noise ratio was measured using a selective microvoltmeter with a 300-kHz slot. When converted to the 150-MHz recorder bandwidth, the SNR (peak-to-peak signal to rms noise) is greater than 40 dB. The laser was free of undesired spectral components due to mode beats within the frequency band of interest. The fundamental longitudinal mode beat frequency ($c/2L$) for the laser diode used was 500 GHz, compared to 115 MHz for the argon laser. Therefore, an additional cavity was not required to inhibit multiple longitudinal modes, since the beat frequency was well above the signal frequency band.

3.3 Record Tests

A dc bias of 450 mA and ac signal swing of 75 mA p-p produced optimum recordings. Under these conditions, the peak power striking the film was measured at 0.73 mW while the average was 0.25 mW. Fig. 15a is a photomicrograph of an argon laser recording at 60 MHz (100 cycles/mm). Fig. 15b shows an injection laser recording at the same frequency. The improved recording mode with the laser diode source is attributed primarily to the higher contrast ratio available (25:1) from the modulated diode output. Figs. 16 a, b, c, and d are semiconductor laser recordings at 30, 60, 80, and 100 MHz, respectively.

3.4 Comparison of the Argon Laser System with the (AlGa)As Laser System

Table 2 compares the two laser systems for continuous recording at 63,500 cm/sec spot velocity.

The recordings made with laser diodes were not continuous. Continuous recording is accomplished by illuminating 2 separate polygon mirrors, which requires twice the laser power. The argon laser recorder has substantial optical losses due to the line selecting prism, the

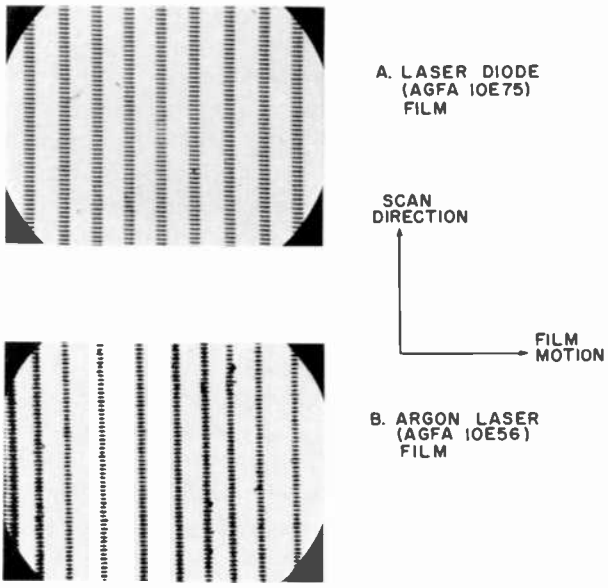

Fig. 15—Comparison of laser diode to argon laser/EO modulator recordings at 60 MHz.

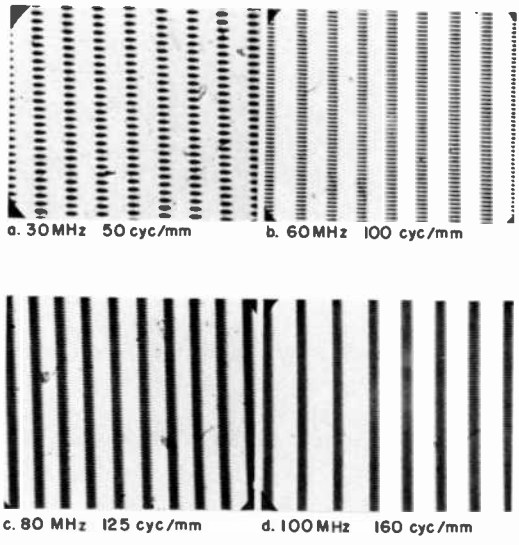

Fig. 16—Laser diode recordings.

etalon, the light modulator, and the aperture that converts the circular beam to a rectangular format.

4. Summary and Conclusions

CW injection lasers have demonstrated excellent performance when used in a wideband film recorder. Such lasers have been internally modulated from 1–200 MHz (±2 dB) and film recordings of signal frequencies up to 100 MHz (160 cycles/mm) have been made. The lasers are stripe contact (AlGa)As devices emitting up to 10 mW at 710 nm at an operating temperature of 77°K. Plans for future experiments include the mating of an injection laser with an acousto-optic beam deflector[4] to make a laser scanner or film recorder. The use of reliable 800-nm cw room-temperature diodes, recently developed,[6] to expose IR film in a moderate-resolution image recorder is also planned.

Table 2—Comparison of Argon Laser and Laser Diode Systems

	Argon	(AlGa)As Diode
Input electrical power	10 kW	10 W
Light power required	1 W (all lines)	8 mW
Wavelength	488 nm	710 nm
AC contrast ratio	5:1	25:1
Spot size	5 × 20 μm	8 × 25 μm
Peak record spot power	0.4 mW(AGFA 10E56)	0.8 mW(AGFA 10E75)
Transmission and aperturing losses	2000:1	10:1
Mode beat frequency ($c/2L$)	115 MHz	500 GHz
Coolant	Water	Liquid nitrogen

Acknowledgments

The author wishes to acknowledge the assistance of G. M. Claffie and S. L. Corsover of the RCA Advanced Technology Laboratories. H. Kressel, I. Landany, F. Z. Hawrylo, and D. Gilbert of the RCA Laboratories provided technical guidance and supplied developmental diode samples. This effort has been partially supported by the Rome Air Development Center under Contract #F30602-74-C-0053. The technical monitors of the program were Messrs. A. Jamberdino and J. Petrozelli.

References

[1] H. Kressel and F. Hawrylo, "Red-Light-Emitting AlGaAs Heterojunction Laser Diodes," *J. Appl. Phys.*, **44**, p. 4222, Sept. 1973.

[2] H. Kressel, H. F. Lockwood, and H. Nelson, "Low Threshold AlGaAs Visible and IR Light-Emitting Diode Lasers," *IEEE J. Quant. Elect.*, **6**, p. 278 (1970).

[3] R. M. Scott, "The Practical Application of Modulation Transfer Functions," *Photogr. Sci. Eng.*, **9**, No. 4, p. 237, July-Aug. 1965.

[4] I. Gorog, J. D. Knox, P. V. Goedertler, and I. Shidlovsky, "A Television Rate Laser Scanner—II. Recent Developments," *RCA Review*, **33**, p. 667, Dec. 1972.

[5] R. F. Kenville, "Wideband Analog Recorder/Readout System," Final Tech. Report, RADC-TR-71-289, Air Force Systems Command, Rome Air Development Center, Oct. 1971.

[6] I. Ladany and H. Kressel, "The Influence of Device Fabrication Parameters on the Degradation of AlGaAs CW Laser Diodes," *Appl. Phys. Lett.*, **25**, No. 12, Dec. 15, 1974.

The Chirp Z-Transform—A CCD Implementation

G. J. Mayer

RCA Missile and Surface Radar Division, Morrestown, N.J.

Abstract—The chirp *z*-transform is a signal processing algorithm that can efficiently evaluate the *z*-transform of a time sampled signal when implemented using charge-coupled devices. The charge-coupled-device chirp *z*-transform realizes significant hardware savings over alternative approaches to perform spectral analysis and has the potential of greater signal-processing flexibility.

1. Introduction

Charge coupled devices (CCD's) are MOS integrated circuits that provide analog delay of electric charge. The optical or electrical input to the CCD is sampled and converted to a packet of charge whose magnitude is proportional to the input. The charge packet moves down the CCD stages, shift register fashion, under the control of clock voltages. The charge packets are transferred from one stage to the next until they reach an output stage where the magnitude of the charge packet is sensed and converted to an electrical analog signal. The clock frequency and the number of stages transferred determine the time delay introduced. These characteristics led initially to the application of CCDs to image sensing and digital memories.

More recently, the application of CCD's to analog signal processing has been receiving great interest. Analog signal processing using CCD's has great potential in areas as diversified as consumer television, seismic instrumentation, and radar systems. In analog sampled-data signal processing, the continuous analog signal is sampled and the analog value is retained. In digital signal processing, on the other

hand, the continuous analog signal sample must be digitized. The digitizing process involved is a source of error and is only the first operation in a stream of complex processing steps.

Analog signal processing using CCD's employs two architectures, untapped and tapped analog delay lines. Applications for the untapped delay line include electrically variable analog delay, time expansion and compression, and time alignment of analog signals. Tapped delay-line applications include time correlation of analog signals, spectrum analyzers, and band-width compression. Some CCD signal processing devices that have been developed at various laboratories are described in References [1]–[3].

2. Chirp *Z*-Transform Algorithm

A signal processing application that makes use of both untapped and tapped CCD delay lines is the chirp z-transform[4] (CZT), which is an algorithm that evaluates the z-transform. Presently, spectrum analysis in signal processing is performed by the fast Fourier transform (FFT) which is an implementation of the discrete Fourier transform (DFT). The CZT algorithm offers many signal processing advantages over the FFT, but only if it can be implemented using analog techniques. Such an implementation is possible using CCDs. The hardware savings of CCD technology and analog sampled-data signal processing offer added incentive to develop the CCD chirp z-transform.

The following derivation is based upon a report by Rabiner, Schafer, and Rader (Ref [4]). The CZT algorithm evaluates the z-transform of a sequence of P samples as shown in Fig. 1. The z-transform of a sequence of samples x_p is defined as

$$X(z) = \sum_{p=-\infty}^{\infty} x_p z^{-p}. \qquad [1]$$

Assuming that the right side of Eq. [1] converges for some values of z, and restricting the evaluation of the z-transform to sequences with a finite number P of non-zero samples, Eq. [1] becomes

$$X(z) = \sum_{p=0}^{P-1} x_p z^{-p}. \qquad [2]$$

For a finite number of points z_k,

$$X_k = X(z_k) = \sum_{p=0}^{P-1} x_p z_k{}^{-p}. \qquad [3]$$

The special case of the z-transform which has received consider-

able attention is the set of points equally spaced around the unit circle of the z-plane:

$$z_k = \exp\left(j \frac{2\pi}{P} k\right), k = 0,1,\ldots,P-1, \quad [4]$$

which gives

$$X_k = \sum_{p=0}^{P-1} x_p \exp\left(-j \frac{2\pi}{P} pk\right), k = 0,1,\ldots,P-1. \quad [5]$$

Eq. [5] is the discrete Fourier transform (DFT). Thus, the DFT is a special case of the z-transform and contains inherent limitations. The limitations include (1) integration only on the unit circle of the z-plane; (2) the number of time samples must be equal to the number of points evaluated by the z-transform; (3) the number of samples evaluated for efficient operation, must be a power of two; and (4) the angular spacing of z_k is as specified by Eq. [4]. The CZT algorithm eliminates these limitations.

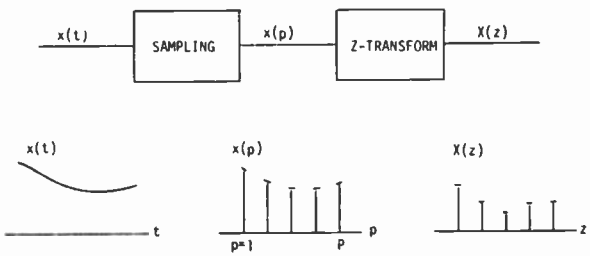

Fig. 1—*Z*-Transform evaluation.

The CZT algorithm can be derived from Eq. [3] using the equation

$$z_k = AB^{-k}, k = 0,1,\ldots,K-1 \quad [6]$$

where K is an arbitrary integer and A and B are arbitrary complex numbers of the form

$$A = A_0 \exp(j\, 2\pi\theta_0) \quad [7]$$

$$B = B_0 \exp(j\, 2\pi\phi_0). \quad [8]$$

Therefore Eq. [3] becomes

$$X_k = \sum_{p=0}^{P-1} x_p A^{-p} B^{pk}, \qquad k = 0,1,\ldots,K-1. \quad [9]$$

By making the substitution[5]

$$pk = \frac{p^2 + k^2 - (k-p)^2}{2}, \qquad [10]$$

Eq. [9] becomes

$$X_k = \sum_{p=0}^{P-1} x_p A^{-p} B^{(p^2/2)} B^{(k^2/2)} B^{-(k-p)^2/2}, k = 0,1,\ldots,K-1. \qquad [11]$$

While Eq. [11] appears to be a more complicated expression of Eq. [9], it leads to a more efficient hardware implementation. Eq. [11] can be broken into three processing parts.

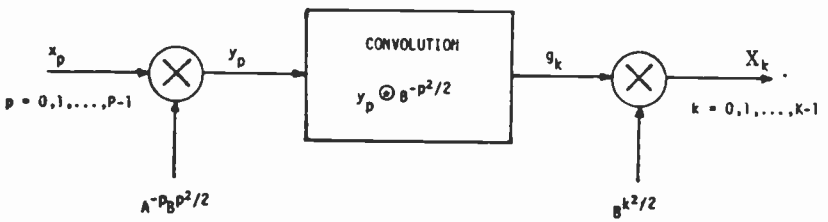

Fig. 2—Processing steps of the chirp z-transform.

The first part consists of a complex multiplication

$$y_p = x_p A^{-p} B^{p^2/2}, p = 0,1,\ldots,P-1 \qquad [12]$$

The series y_p is then multiplied by the term $B^{-(k-p)^2/2}$ and summed to perform complex convolution

$$g_k = \sum_{p=0}^{P-1} y_p B^{-(k-p)^2/2}, \qquad k = 0,1,\ldots,K-1. \qquad [13]$$

The series g_k is multiplied by $B^{k^2/2}$. Therefore

$$X_k = g_k B^{k^2/2}, k = 0,1,\ldots,K-1. \qquad [14]$$

This CZT three-step process is illustrated in Fig. 2.

Use of the CZT algorithm thus eliminates the limitations of the DFT mentioned earlier:

(1) The CZT algorithm can evaluate the z-transform along contours inside and outside the unit circle of the z-plane. By evaluating the z-transform along a selected contour, the transfer function

of a linear system can be adjusted to sharpen or flatten the frequency response. The choice of contour is dependent on which of the systems poles should be emphasized.

(2) The CZT algorithm allows arbitrary selection of starting frequency and frequency spacing, independent of the number of time samples. It can therefore evaluate high-resolution narrow-frequency-band spectra at relatively low cost, providing high resolution for a limited range of frequencies and low resolution for the undesired ranges of the rest of the spectrum.

(3) With CZT, interpolation between time samples of a bandlimited function can be obtained with greater ease than with the DFT, and interpolation at arbitrary sampling intervals can be performed efficiently.

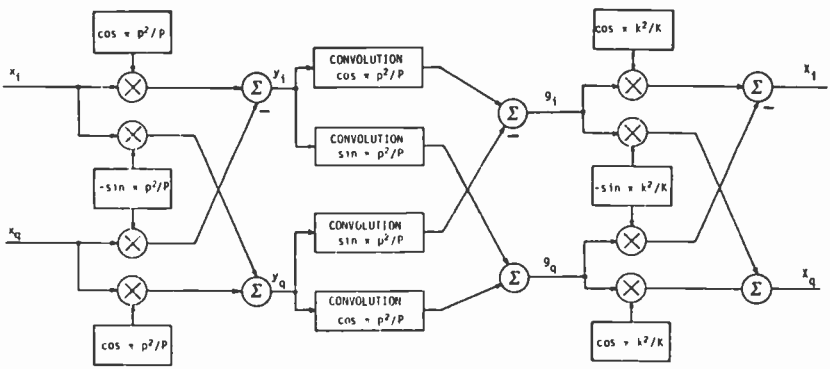

Fig. 3—Functional diagram of the chirp *z*-transform.

As an example of the signal processing tasks to which the CZT is applicable, we will describe here its use as a spectral analyzer that will process complex data. The implementation of the algorithm is derived from Fig. 2 and is shown in Fig. 3. In the derivation the real and complex quantities are represented by i and q, respectively. Letting

$$f = A^{-p}B^{p^2/2} \quad [15]$$

$$y = xf \quad [16]$$

$$y = x_i f_i + jx_i f_q + jx_q f_i + j^2 x_q f_q \quad [17]$$

$$y_i = x_i f_i + j^2 x_q f_q \quad [18]$$

$$y_i = x_i f_i - x_q f_q \quad [19]$$

$$y_q = j x_i f_q + j x_q f_i \quad [20]$$

$$y_q = j(x_i f_q + x_q f_i). \quad [21]$$

Similarly, letting

$$e = B^{-p^2/2}, \quad [22]$$

$$g = y^* e \quad [23]$$

$$g = y_i^* e_i + y_i^* j e_q + j y_q^* e_i + j y_q^* j e_q \quad [24]$$

$$g_i = y_i^* e_i - y_q^* e_q \quad [25]$$

$$g_q = y_i^* j e_q + j y_q^* e_i; \quad [26]$$

and letting

$$d = B^{k^2/2}, \quad [27]$$

$$X = gd \quad [28]$$

$$X = g_i d_i + j g_i d_q + j g_q d_i + j^2 g_q d_q \quad [29]$$

$$X_i = g_i d_i - g_q d_q \quad [30]$$

$$X_q = j(g_i d_q + g_q d_i). \quad [31]$$

For $B_0 = 1$ in Eq. [8], the sequence $B^{p^2/2}$ is a complex sinusoid. Eqs. [15], [22], and [27] can therefore be represented as follows:

$$f_i = \cos \pi p^2/P \quad [32]$$

$$f_q = -\sin \pi\, p^2/P \quad [33]$$

$$e_i = \cos \pi\, p^2/P \quad [34]$$

$$e_q = \sin \pi\, p^2/P \quad [35]$$

$$d_i = \cos \pi\, k^2/K \quad [36]$$

$$d_q = -\sin \pi k^2/K \quad [37]$$

Substituting Eqs. [32], [33], [34], [35], [36], and [37] into Eqs. [19], [21], [25], [26], [30], and [31], respectively, the complex CZT implementation can be described:

$$y_i = x_i\, (\cos \pi\, p^2/P) + (\sin \pi p^2/P) \quad [38]$$

$$y_q = j\, [-x_i\, (\sin \pi\, p^2/P) + x_q\, (\cos \pi\, p^2/P)] \quad [39]$$

$$g_i = y_i^*\, (\cos \pi\, p^2/P) - y_q^*\, (\sin \pi\, p^2/P) \quad [40]$$

$$g_q = y_i{*}j\ (\sin \pi\, p^2/P) + jy_q{*}\ (\cos \pi\, p^2/P) \quad [41]$$

$$X_i = g_i\ (\cos \pi\, k^2/K) + g_q\ (\sin \pi\, k^2/K) \quad [42]$$

$$X_g = j[-g_i\ (\sin \pi\, k^2/K) + g_q\ (\cos \pi\, k^2/K)] \quad [43]$$

The CZT of Fig. 3 can be implemented using off-the-shelf analog components and CCD's.

Implementation of the Chirp Z-Transform with CCD's

The application of CCD's to the chirp z-transform algorithm requires the use of tapped and untapped delay lines to perform the convolution shown in Fig. 3. A tapped CCD is used as a correlator with the weights in reverse order (see Fig. 3). It gives partial product terms. An untapped CCD is used to combine these terms and give convolution. A block diagram of the CCD CZT is shown in Fig. 4.

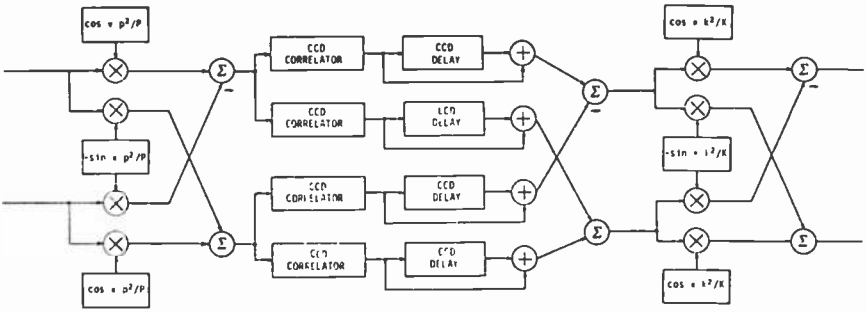

Fig. 4—CCD chirp z-transform.

The CCD correlators of Fig. 4 can be implemented using either of two arrays. One is a thirty-two stage delay line, where each stage of the delay line is tapped and weighted. This is accomplished using a split-gate weighting technique (see Figs. 5 and 6). Fig. 5 shows the split-gate electrodes above the SiO_2-Si interface, which contains the charges. The amount of charge passing under the split-gate electrodes is sensed and weighted according to the percent of the electrode for the positive ($+\phi_2$) and negative ($-\phi_2$) bus as shown in Fig. 6. In Fig. 6 the first split gate is more negatively weighted, the second more positively weighted, and the third is equally weighted. The output signal is obtained by connecting the $+\phi_2$ and $-\phi_2$ bus to a differential amplifier circuit. It is not only necessary to sense the signal due

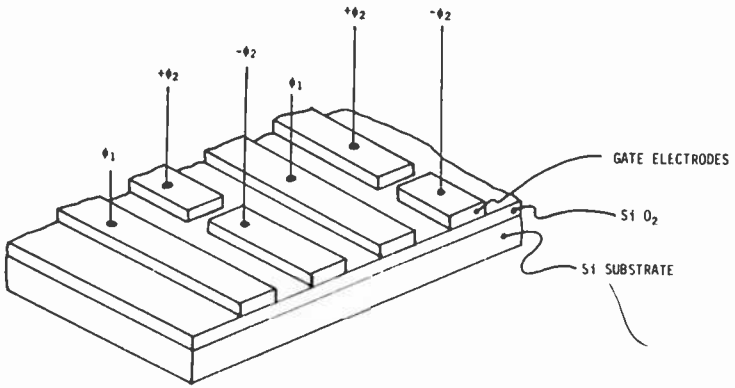

Fig. 5—Split-gate CCD.

to the charges and the weighting, it is also necessary to eliminate the ϕ_2 clock.

The weighting required is incorporated into the mask at the time of fabrication of the CCD. Although mask programmable weighting is a viable technique, it is an inherent limitation.

The other CCD array, currently under development, uses a weighting technique that allows for programmable weights. This array consists of two sixty-four stage CCD delay lines that are tapped at every other stage. The tapped outputs are coupled, as shown in Fig. 7, through four-quadrant MOS multipliers (*1 through *32). The + and − bus lines are the output of the MOS multipliers, and a differential amplifier circuit is used to obtain the partial product terms of the convolution. The partial products are summed, to give the convolution, using operational amplifiers.

The other major part of the CZT consists of the CZT weighting, which occurs before and after the correlation as shown in Fig. 4. Since

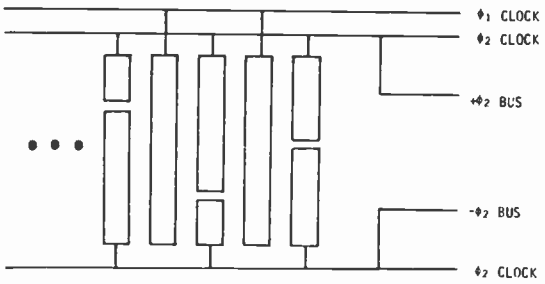

Fig. 6—Split-gate weighting.

both are implemented in essentially the same manner, a single description will suffice. Two techniques have been envisioned. The first consists of wideband four-quadrant analog multipliers with the weights generated by programmable read-only memories (PROM's) and coupled through digital/analog converters (D/A's). This would provide the appropriate weights in analog form. The second technique uses multiplying D/A's with PROM weight storage.

The entire CZT requires appropriate clocking and timing circuitry for processing and weight generation. Initially a feasibility model of the CZT would evaluate thirty-two complex z-transform samples. To accomplish this would require sixty-four clock periods. The first thirty-two clock periods would be used for the CZT weighting prior to correlation and to fill the correlator. The second thirty-two clock periods would empty the correlator and perform the CTZ weighting after the correlation. A correlator length of thirty-two taps was chosen to optimize the flexibility of use in various signal processing systems.

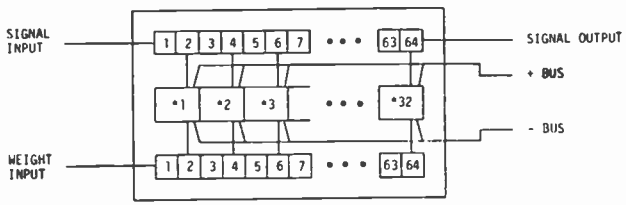

Fig. 7—Programmable weight CCD correlator.

Computer Simulation

The CZT algorithm was programmed to verify the anticipated operation of the CZT and to provide the values necessary for the CZT convolution. The convolution values generated were used to program the split gate weights as shown in Figs. 5 and 6. These weights, for the I and Q arrays, are shown in Table 1.

The program verified that the CZT algorithm performs the z-transform and that the complex correlation technique used performs the complex convolution. The input for the CZT requires that the thirty-two input samples be followed by thirty-two zeros. This is necessary, as the convolution is performed using a correlator. The first thirty-one output samples are invalid for the same reason. Output samples thirty-two to sixty-three therefore, constitute the spectral

Table 1—CZT Convolution Weights

1	BI	0.995184	BQ 0.098025	17	BI	−0.995135	BQ −0.098019
2	BI	0.923877	BQ 0.382689	18	BI	0.923882	BQ 0.382677
3	BI	0.634389	BQ 0.773014	19	BI	−0.634392	BQ −0.773011
4	BI	−0.000005	BQ 1.000000	20	BI	−0.000001	BQ 1.000000
5	BI	−0.773013	BQ 0.634390	21	BI	0.773011	BQ −0.634393
6	BI	−0.923878	BQ −0.382688	22	BI	−0.923880	BQ −0.382684
7	BI	0.098023	BQ −0.995184	23	BI	−0.098018	BQ 0.995185
8	BI	1.000000	BQ −0.000007	24	BI	1.000000	BQ 0.000001
9	BI	−0.098012	BQ 0.995185	25	BI	0.098017	BQ −0.995185
10	BI	−0.923881	BQ −0.382681	26	BI	−0.923880	BQ −0.382683
11	BI	0.773011	BQ −0.634393	27	BI	0.773010	BQ 0.634394
12	BI	0.000011	BQ 1.000000	28	BI	0.000000	BQ 1.000000
13	BI	−0.634398	BQ −0.773006	29	BI	0.634393	BQ 0.773010
14	BI	0.923880	BQ 0.382682	30	BI	0.923880	BQ 0.382683
15	BI	−0.995186	BQ −0.098006	31	BI	0.995185	BQ 0.098017
16	BI	1.000000	BQ −0.000005	32	BI	1.000000	BQ 0.000000

output of the CZT and, for simplicity, will be numbered one to thirty-two. The inputs and outputs used in the simulation are shown in Figs. 8 through 13.

Figure 8 shows a real (XI) and imaginary (XQ) sinusoidal input of two cycles across the aperture. The output magnitude ratio and phase angle are also shown corresponding to this input. Fig. 9 shows an input of twice the frequency (four cycles) and the corresponding output, which is shifted two spectral lines to the left. Fig. 10 shows an input of four times that of Fig. 8. The output here is shifted by six spectral lines to the left of that in Fig. 8. In Fig. 11 the input of sixteen cycles (eight times that of Fig. 8) gives an output whose spectral line is shifted fourteen spectral lines to the left of that in Figure 8.

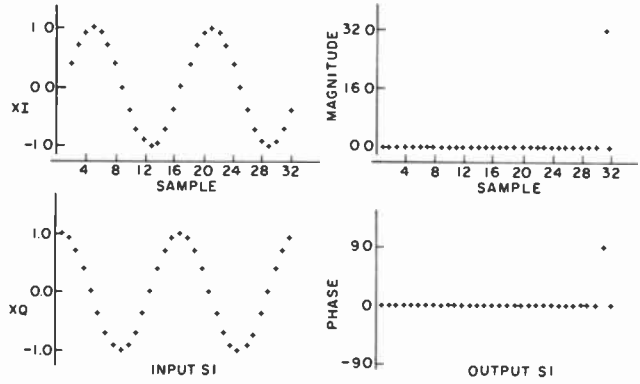

Fig. 8—Real (XI) and imaginary (XQ) sinusoidal input of two cycles across the aperture.

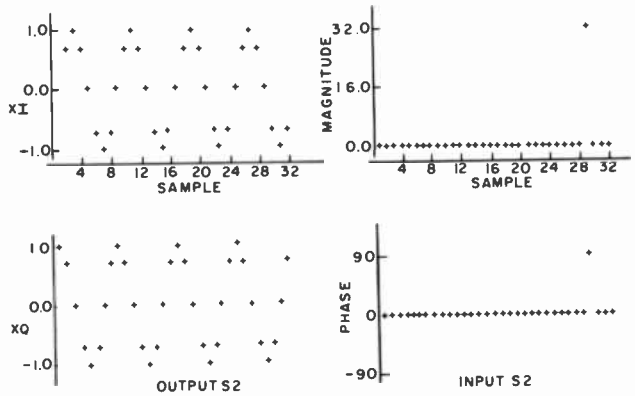

Fig. 9—Input twice that of Fig. 8 (4 cycles) and corresponding output.

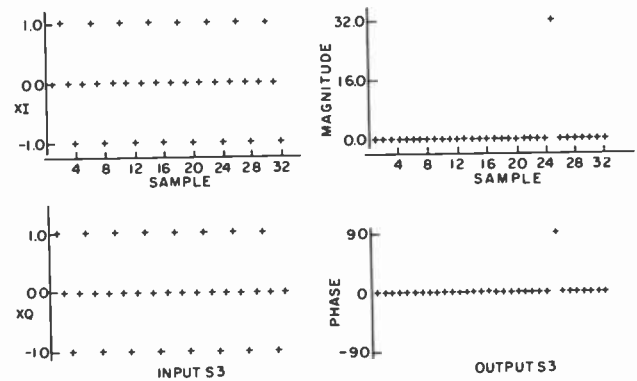

Fig. 10—Input four times that of Fig. 8 and corresponding output.

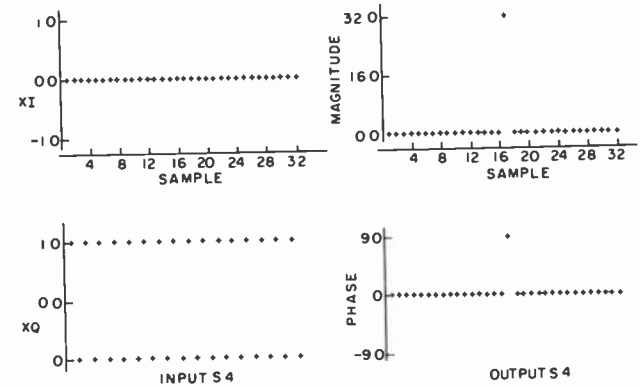

Fig. 11—Input of sixteen cycles and output (shifted 14 spectral lines to the left of Fig. 8).

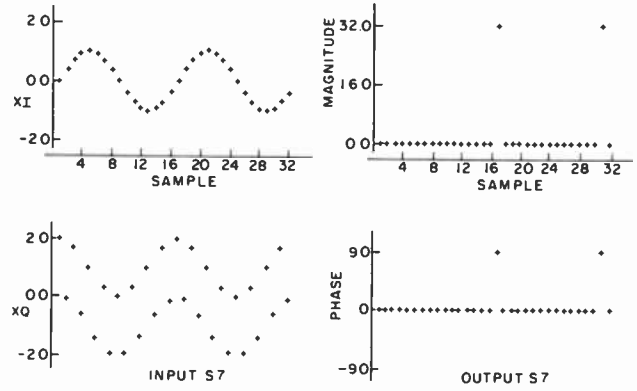

Fig. 12—Superposition (addition of inputs from Figs. 8 and 11) and corresponding output.

Fig. 12 illustrates superposition, as the input is the addition of the inputs from Figs. 8 and 11, and the output is the addition of the outputs.

To simulate the impulse response with I and Q processing, values for the impulse can be chosen to give an arbitrary phase angle. In Fig. 13 the values for the input were chosen to give a phase angle of 74.5°. The simulated output for this input is shown in Fig. 13 and gives the expected results.

The inverse chirp z-transform (CZT^{-1}) takes z-transform samples of a time sampled input and converts them back into the time domain. Computer simulation was used to determine the proper algorithm. This was done as shown in Fig. 14. The first attempt to obtain the CZT^{-1} used a CZT and varied the sign of the inputs. Table 2

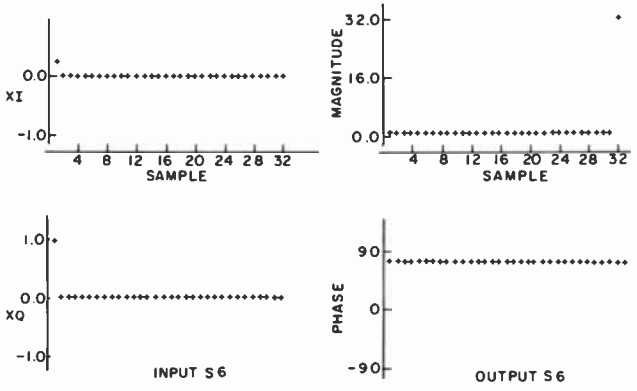

Fig. 13—Simulated output for input chosen to give phase angle of 74.5°.

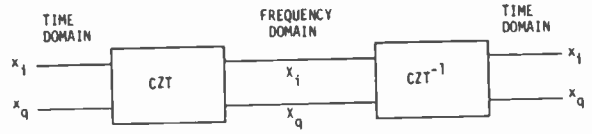

Fig. 14—Simulation to determine inverse chirp z-transform (CZT^{-1}) algorithm.

summarizes these simulations. The time input used is shown in Fig. 15 along with the CZT output. This input was chosen because its asymmetry would be helpful in determining if the CZT^{-1} output was in the proper time sequence.

The results of the simulations shown in Table 2 suggest that the CZT^{-1} algorithm should accept the z-transformed samples in reversed order. A second set of simulations was undertaken in which the first z-transformed sample out of the CZT is the last one into the CZT^{-1} and so on. A summary of these simulations is shown in Table 3.

From the simulation, it is observed that the correct CZT^{-1} algo-

Table 2—Simulations for CZT^{-1}

	Sign of CZT^{-1} Inputs		CZT^{-1} Outputs	
	X_i	X_q	x_i	x_q
Case 1	+	+	Reverse time sequence	Reverse time sequence
Case 2	+	–	Correct	180° out of phase
Case 3	–	+	180° out of phase	Correct
Case 4	–	–	Reverse time sequence, 180° out of phase	Reverse time sequence, 180° out of phase

Table 3—Simulations for CZT^{-1} with Z-Transformed Samples in Reversed Order

	Sign of CZT^{-1} Inputs		CZT^{-1} Outputs	
	X_i	X_q	x_i	x_q
Case 5	+	+	Correct	Correct
Case 6	+	—	Reverse time sequence, 180° out of phase	Reverse time sequence
Case 7	—	+	Reverse time sequence	Reverse time sequence, 180° out of phase
Case 8	—	—	180° out of phase	180° out of phase

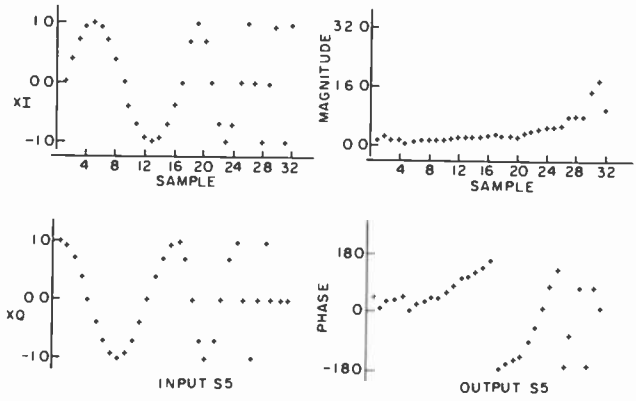

Fig. 15—Time input used in CZT^{-1} simulation and output.

rithm requires that the sequence of the z-transform samples for the input be reversed with no sign change.

Applications

The CCD chirp z-transform can be used in a variety of applications. One example, where its application could have great impact, is in pulse compression. Pulse compression is a signal processing function used in radar and sonar systems to reduce the peak power requirements of the transmitter by sending out a long coded pulse and then compressing the received pulse to obtain resolution comparable to that obtained when transmitting a narrow pulse.

Fig. 16 is a block diagram of a linear FM pulse-compression system incorporating a CZT and CZT^{-1} using the step transform.[6] The step transform algorithm functionally operates by mixing the expanded pulse video input with a frequency ramped sawtooth reference waveform. The effect of this mixing is to convert the long-duration-input linear FM waveform into a staircase waveform with individual "steps," each of duration much less than the expanded pulse length. The staircase waveform steps are obtained by repeating the reference for each ramp of the sawtooth. The first CCD CZT operates on the continuous steps and enters the spectral coefficients associated with

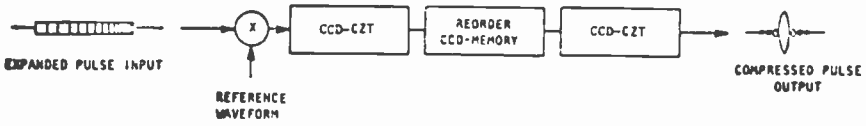

Fig. 16—CCD step transform.

each step into the reorder CCD memory. The second CCD CZT operates on appropriately selected spectral samples from each of the steps across the entire waveform and provides a coherent weighted sum at the output. A square-sum combination of the real and imaginary output channels provides the compressed pulse output. Fig. 16 is a simplified diagram; the reader is referred to Ref. [6] for a more complete treatment of the step-transform process.

Further analysis has indicated that the CZT processing functions and those required by the step-transform process, can be combined to streamline the CCD step-transform processor. . A simplified block diagram is shown in Fig. 17. The half-aperture delay is provided to fa-

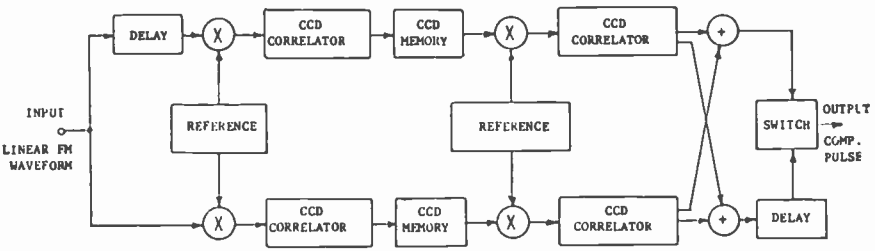

Fig. 17—CCD step-transform processor.

cilitate a continuous matched filtering process. If the processor is implemented with the 32-stage CCD correlator described earlier, the time bandwidth product will be 256. Longer time-bandwidth products can be obtained by cascading the correlators and appropriately changing the memory and reference storage. The two reference storage locations combine the CZT weighting coefficients, reference waveform, and sidelobe suppression weighting. This functional combination results in a very efficient hardware implementation.

References

[1] M. F. Tempsett and E. J. Zimany, "Use of Charge-Coupled Devices for Analog Delay," 1972 ISSC Conf., Phila., Pa., Digest Tech. Papers, p. 136.

[2] D. D. Buss, D. R. Collins, W. H. Bailey, and C. R. Reeves, "Transversal Filtering Using Charge Coupled Devices," *IEEE J. Solid-State Circuits*, **SC-8**, p. 138, 1973.

[3] L. O. Upton and G. J. Mayer, "Charge Coupled Devices and Radar Signal Processing," RCA Reprint RE21-1-6.

[4] L. R. Rabiner, R. W. Schafer, and C. M. Rader, "The Chirp-Z-Transform Algorithm and its Application," *Bell. Syst. Tech. J.*, p. 1249, May–June 1969.

[5] L. I. Bluestein, "A Linear Filtering Approach to the Computation of the Discrete Fourier Transform," *1968 Northeast Elec. Research and Eng. Meeting Record*, p. 218, Nov. 1968.

[6] R. P. Perry and H. W. Kaiser, "Digital Step Transform Approach to Airborne Radar Processing," *NAECON '73 Record*, p. 280.

Recent Papers by RCA Authors

Listing is alphabetical by name of primary author. For copies of reprints, the reader should contact the publication directly.

B. Abeles, H. L. Pinch, and J. I. Gittleman, "Percolation Conductivity in W-Al_2O_3 Granular Metal Films," **Phys. Review Lett.**, Vol. 35, No. 4, p. 247, July 28, 1975.

B. Abeles, P. Sheng, M. D. Coutts, and Y. Arie, "Structural and Electrical Properties of Granular Metal Films," **Advances in Phys.**, Vol. 24, No. 3, p. 407, May 1975.

B. Abeles, "Tunneling Conductivity in Granular Metal Films," **RCA Review**, Vol. 36, No. 3, p. 594, Sept. 1975.

M. S. Abrahams and C. J. Buiocchi, "Cross-Sectional Electron Microscopy of Silicon on Sapphire," **Appl. Phys. Lett.**, Vol. 27, No. 6, p. 324, Sept. 1975.

M. S. Abrahams, C. J. Buiocchi and G. H. Olsen, "Dislocations in Vapor-Grown Compositionally Graded (In,Ga)P," **J. Appl. Phys.**, Vol. 40, No. 10, p. 4259, Oct. 1975.

A. Akselrad, R. E. Novak, and D. L. Patterson, "Influence of Annealing on the Absorption of Bi-Based Iron Garnet Films," **AIP Conference Proceedings**, 20th Annual Conference No. 24.

R. C. Alig, "Acoustic Diffraction and the Electrostrictive Transducer," **J. Appl. Phys.**, Vol. 46, No. 9, p. 3731, Sept. 1975.

V. S. Ban and S. L. Gilbert, "Chemical Processes in Vapor Deposition," **J. Electrochem. Soc.**, Vol. 122, No. 10, p. 1384, Oct. 1975.

D. E. Carlson, "The Deposition of Tin Oxide Films from a D-C Glow Discharge," **J. Electrochem. Soc.**, Vol. 122, No. 10, p. 1334, Oct. 1975.

R. S. Crandall, "Criterion for the Onset of Hot-Electron Transport," **RCA Review**, Vol. 36, No. 3, p. 531, Sept. 1975.

E. C. Douglas and A. F. F. Dingwall, "Surface Doping Using Ion Implantation for Optimum Guard Layer Design in COS/MOS Structures," **IEEE Trans. Electron Devices**, Vol. 22, No. 10, p. 840, Oct. 1975.

M. Ettenberg and C. J. Nuese, "Comparison of Zn-Doped GaAs Layers Prepared by Liquid-Phase and Vapor-Phase Techniques, Including Diffusion Lengths and Photo-Luminescence," **J. Appl. Phys.**, Vol. 46, No. 8, p. 3500, Aug. 1975.

B. W. Faughnan, R. S. Crandall, and M. A. Lampert, "Model for the Bleaching of WO_3 Electrochomic Films by an Electric Field," **Appl. Phys. Lett.**, Vol. 27, No. 5, p. 275, Sept. 1, 1975.

A. M. Goodman, "An Approximate Model of the Beam-Blocking Contact in a PbO Vidicon," **RCA Review**, Vol. 36, No. 3, p. 408, September 1975.

J. J. Hanak, "Co-Sputtering—Its Limitations and Possibilities," **LeVide**, No. 175, p. 11, Jan./Feb. 1975.

G. Harbeke, "Interlayer Interaction and Optical Properties of Layer Semiconductors: 2H and 4H Polytypes of PbI_2," **Phys. Stat. Sol. (b)**, Vol. 68, p. 569, 1975.

K. C. Hernqvist and A. H. Firester, "Prealignment of Gas Laser Cavities," **Rev. Scientific Instruments**, Vol. 46, No. 8, p. 1040, Aug. 1975.

G. Kaganowicz, E. F. Hockings, and J. W. Robinson, "Influence of Zinc on Cobalt Substituted Magnetic Recording Media," **IEEE Trans. of Magnetic**, Vol. Mag-11, No. 5, p. 1194, Sept. 1975.

J. Kane, H. P. Schweizer, and W. Kern, "Chemical Vapor Deposition of Transparent Electrically Conducting Layers of Indium Oxide Doped with Tin," **Thin Solid Films**, Vol. 29, p. 155, 1975.

J. Kane, H. P. Schweizer and W. Kern, "Chemical Vapor Deposition of Transparent, Electrically Conductive Tin Oxide Films Formed from Dibutyl Tin Diacetate," **J. Electrochem. Soc.**, Vol. 122, No. 8, p. 1145, Aug. 1975.

H. Kiess and B. Binggeli, "Speed of Response of Photocurrents in CdSe," **RCA Review**, Vol. 36, No. 3, p. 485, Sept. 1975.

J. Klatskin and A. Rosen, "Simple Method for Separating Completed Diodes from Semiconductor Wafers," **J. Electrochem. Soc.**, Vol. 122, No. 11, p. 1565, Nov. 1975.

W. F. Kosonocky and J. E. Carnes, "Basic Concepts of Charge-Coupled Devices," **RCA Review**, Vol. 36, No. 3, p. 566, Sept. 1975.

H. Kressel, "The Application of Heterojunction Structures to Optical Devices," **J. Electronic Materials,** Vol. 4, No. 5, 1975.
H. Kressel and M. Ettenberg, "A New Edge-Emitting (AlGa)As Heterojunction LED for Fiber-Optic Communications," **Proc. IEEE,** p. 1360, Sept. 1975.
M. A. Lampert, "Simplicity in Theory: An Anecdotal Account of Current Injection in Solids—In Tribute to Albert Rose," **RCA Review,** Vol. 36, No. 3, p. 444, Sept. 1975.
S. Larach and J. Gerber, "Analysis of Phosphor Coatings by Luminescence Thermal Degradation," **Analytica Chimica Acta,** p. 329, 1975.
S. Larach, "Preparation and Doping of $CaLaZrTaO_7$ Pyrochlore," **Inorganica Chimica Acta Lett.,** Vol. 15, No. 1, July 31, 1975.
H. W. Lehman and R. Widmer, "Preparation and Properties of Relatively Co-Sputtered Transparent Conducting Films," **Thin Solid Films,** Vol. 27, No. 2, p. 359, July 1975.
J. J. Mezrich, "Pattern Meaningfulness and Pattern Detectability," **RCA Review,** Vol. 36, No. 3, p. 621, September 1975.
R. Mezrich and D. H. R. Vilkomerson, "Ultrasonic Phase-Contrast Imaging," **Appl. Phys. Lett.,** Vol. 27, No. 4, Aug. 1975.
A. R. Moore, "Solar-Cell Capacitance," **RCA Review,** Vol. 36, No. 3, p. 551, Sept. 1975.
J. I. Pankove, "Low-Voltage Blue Electroluminescence in GaN," **IEEE Trans. Electron Devices,** Vol. ED-22, No. 9, p. 721, Sept. 1975.
R. J. Powell, "Hole Photocurrents and Electron Tunnel Injection Induced by Trapped Holes in SiO_2 Films," **J. Appl. Phys.,** Vol. 40, No. 10, p. 4457, Oct. 1975.
David Redfield, "Optical and Electrical Effects," **J. Electronic Materials,** Vol. 4, No. 5, 1975.
David Redfield, "Transparent Properties of Electrons in Energy Band Tails," **Advances in Phys.,** Vol. 24, No. 4, p. 463, July 1975.
A. Rosen, H. Kawamoto, J. Klatskin, and E. L. Allen, Jr., "Integrated TRAPATT Diode Arrays," **J. MTT,** p. 841, Oct. 1975.
J. Sandercock, "Some Recent Applications of Brillouin Scattering in Solid State Physics," **Advances in Solid State Phys.,** Vol. XV, p. 183, 1975.
G. L. Schnable, "Passivation of Coatings on Silicon Devices," **J. Electrochem. Soc.,** Vol. 122, No. 8, p. 1093, Aug. 1975.
R. W. Smith, "An X-Ray Sensitive Fiber-Optic Intensifier Screen for Topography," **RCA Review,** Vol. 36, No. 3, p. 632, Sept. 1975.
C. W. Struck and W. H. Fonger, "Relation Between Inverse Emission and Absorption Rates for Multiphonon Transitions," **J. Chem. Phys.,** Vol. 63, No. 4, p. 1533, Aug. 15, 1975.
J. L. Vossen and J. J. O'Neill, Jr., "Ultra-Stable System for RF Sputtering with RF-Induced Substrate Bias," **J. Vac. Sc. Technol.,** Vol. 12, No. 5, p. 1052, Sept./Oct., 1975.
R. S. Mezrich, K. F. Etzold and D. H. R. Vilkomerson, "System for Visualizing and Measuring Ultrasonic Wavefronts," **Acoustical Holography,** Vol. 6.
S. V. Forgue, L. D. Miller, and J. O. Schroeder, "The Iricon: A Passive Infrared Camera Tube," **IEEE Trans. on Electron Devices,** Vol. ED-22, No. 10, p. 904, Oct. 1975.
E. B. Priestley, B. Abeles, and R. W. Cohen, "Surface Plasmons in Granular Ag-SiO_2 Films," **Phys. Rev. B,** Vol. 12, No. 6, p. 2121, Sept. 15, 1975.
P. K. Weimer, "From Camera Tubes to Solid-State Sensors," **RCA Review,** Vol. 36, No. 3, p. 385, Sept. 1975.
D. Vilkomerson and B. Hurley, "Progress in Annular Array Imaging," **Acoustical Holography,** p. 145, Vol. 6, Plenum Publishing Corp. (1975).
R. Williams, "Structure and Energy of the Interface Between an Insulator and an Electrolyte," **RCA Review,** Vol. 36, No. 3, p. 542, Sept. 1975.
C. R. Wronski, "Semiconductor Heterojunction Vidicons," **RCA Review,** Vol. 36, No. 3, p. 425, Sept. 1975.

Patents Issued to RCA Inventors, Third Quarter 1975

July

P. R. Ahrens High Voltage Protection Circuit (3,894,269)
F. L. Bechly and J. J. Young Technique for Minimizing Interference in Video Records Reproducer Systems (3,893,168)
G. T. Burton Control Circuits (3,895,317)
G. N. Butterwick Proximity Image Tube with Bellows Focussing Structure (3,894,258)
R. B. Comizzoli Method of Selectively Depositing Glass on Semiconductor Devices (3,895,127)
J. P. Dismukes Chemical Vapor Deposition of Liminescent Films (3,894,164)
R. J. D'Amoto Cathode-Ray Tube Screening Correction Lens with a Non-Solarizing Material (3,893,750)
G. B. Dodson, III Average Value Crossover Detector (3,892,950)
G. B. Dodson, III Circuit for Determining the Time of Transitions in an Alternating Signal (3,892,949)
S. L. Gilbert and M. Ettenberg Method for Epitaxially Growing a Semiconductor Material on a Substrate from the Liquid Phase (3,897,281)
A. M. Goodman and G. M. Breece Provision of Reproducible Thin Layers of Silicon Dioxide (3,892,891)
L. A. Goodman and D. E. Carlson Fabrication of Liquid Crystal Devices (3, 896,016)
H. Huang and A. San-Paolo Method of Making a Semiconductor Device (3,895,429)
R. B. Jarl Apparatus for Non-Destructively Testing a Forwardly Biased Transistor for Second Breakdown (3,895,297)
M. Kaplan and E. B. Davidson Electron Beam Recording Media (3,893,127)
N. I. Korman Radar System with a Very Short Pulse Length (3,895,383)
I. E. Martin Multiple Cell High Frequency Power Semiconductor Device Having Bond Wires of Differing Inductance from Cell to Cell (3,893,159)
A. Mayer and S. Shwartzman Megasonic Cleaning System (3,893,869)
J. E. Miller Computer for Threshold of Tau (3,893,112)
J. Mitchell, Jr. and L. A. Carr, Jr. Technique for Fabricating High *Q* MIM Capacitors (3,894,872)
A. M. Morrell, W. H. Barkow, and J. Gross Self-Converging Color Television Display System (3,892,996)
J. H. Owens Method of Setting the 4.5 MHZ Trap in a Television Receiver (3, 892,913)
G. D. Pyles System for Dynamic and Static Muting (3,894,201)
L. C. Schaeperkoetter Spectrum Differential Noise Squelch System (3,894,285)
S. A. Steckler Electric Circuit for Providing Temperature Compensated Current (3,895,286)
J. E. Wright Power Transistor Having Good Thermal Fatique Capabilities (3,896,486)

August

A. A. Ahmed Switching Circuit Having Multiple Operating Modes (3,902,079)
T. V. Bolger Integral Correction and Transverse Equalization Method and Apparatus (3,899,666)
M. G. Brown, Jr. and D. W. Barch Cathode-Ray Tube Having Lithium Silicate Glare Reducing Coating with Reduced Light Transmission and Method of Fabrication (3,898,509)
J. Conradi Semiconductor Radiation Detector (3,898,686)

W. H. Donovan Programmable Test of Read/Write Circuitry by Varing Clipping Levels (3,902,190)
N. N. Feldstein Method of Electroless Plating (3,900,599)
J. B. George Crystal-Lock Tuning System for Tuning Regularly and Irregularly Spaced Channel Frequencies (3,898,567)
E. C. Giamio, Jr. Method of Making a Transparency of a Colored Image in a Magneto-Electric Printing System (3,898,082)
R. Goodman Adjustable Bed (3,898,702)
J. J. Hanak and D. M. Stevenson Method of Forming a Thin Piezoelectric Body Metallically Bonded to a Propagation Medium Crystal (3,897,628)
W. J. Hannan and R. S. Singleton Notch Rejection Filter (3,898,375)
K. C. Hudson Illuminator Employing Holographic Technique (3,901,578)
D. S. Jacobson High Frequency Transistor (3,902,188)
J. B. Klatskin Method for Manufacturing Semiconductor Devices (3,897,627)
I. Ladany and W. M. Cannull Method of Forming PN Junctions by Liquid Phase Epitaxy (3,899,371)
R. M. Mehalso and G. Kaganowicz Metallized Video Disc Having a Dielectric Coating Thereon (3,901,994)
M. A. Polinsky Method of Making a Junction-Isolated Semiconductor Integrated Circuit Device (3,898,107)
A. R. Rabb Compact Frequency Reuse Antenna (3,898,667)
R. J. Ryan and H. G. Schelble Holographic Recording Media (3,898,358)
P. R. Scott, Jr. Print Actuator Arrangement and Encoder (3,901,371)
S. A. Steckler Hysteresis Voltage Supply for Deflection Synchronizing Waveform Generator (3,898,525)
S. A. Steckler and A. L. Limberg Dual Mode Deflection Synchronizing System (3,899,635)
U. M. Van Bogget Circuit for Supplying Power to a Load (3,898,553)
P. K. Weimer Charge Amplifier (3,900,743)
C. R. Wheeler and R. K. Reusch Electrical Device with Electrode Connections (3,902,003)
C. T. Wu Apparatus for Scanning Raised Indicia (3,900,717)

September

T. C. Abrahamsen and J. D. Zaccai Check-Out Counter on Similar Article (D236780)
A. A. Ahmed Current Amplifier (3,904,976)
A. L. Baker Signal Switching Apparatus for Compensating Record Defects (3,909,518)
W. M. Binder Grinding Machine for Generating A Surface of Revolution on a Hollow Workpiece (3,903,656)
J. K. Clemens Disc Records with Groove Bottom Depth Variations (3,909,517)
A. S. Clorfeine Lumped Element, Broad-Band Microwave Apparatus Using Semiconductor Diodes Operating in the Trapatt Mode (3,909,740)
W. W. Evans Digital Tuning of Voltage Control Television Tuners (3,906,351)
J. B. Fischer, R. A. Ito, W. L. Ross, M. R. Schmidt, and S. W. Stoddard Electronic Scoring System for Bowling Establishments (3,907,290)
B. F. Floden Film Projector Apparatus (3,906,691)
P. Foldes Multimode Horn Antenna (3,906,508)
P. Foldes Adjustable Polarization Antenna System (RE28546)
R. T. Griffin and D. L. Hillman Circuits Exhibiting Hysteresis Using Transistors of Complementary Conductivity Type (3,904,888)
P. E. Haferl Combined Amplifiers Which Consume Substantially Constant Current (3,904,973)
J. F. Heagy Production of Lead Monoxide Coated Vidicon Target (3,909,308)

F. F. Henriques Fault Detector Facilitating Means for Card Reader of Identification Card Reading System (3,906,448)
K. C. Hernqvist Gas Laser Tube (3,904,986)
C. D. Hughes, W. C. Painter, and C. A. Rypinski Data Signaling Noise Suppression System (3,909,727)
L. R. Hulls and S. C. Hadden Exhaust-Responsive Engine Speed and Condition Indicator (3,908,167)
K. Katagi Quasi-Constant Rate Vector Generator (3,903,506)
H. G. Kiess Apparatus for Copying an Electrostatic Charge Pattern in Intensified Form (3,906,501)
M. G. Kovac Removal of Dark Current Spikes from Image Sensor Output Signals (3,904,888)
H. J. Laiming Adherent Solderable Cermet Conductor (3,903,344)
A. J. Leidich Overvoltage Protection Circuit (3,904,931)
A. L. Limberg Transistor Base Biasing Using Semiconductor Junctions (3,903,479)
I. E. Martin High Frequency Semiconductor Device Having Improved Metallized Patterns (3,908,185)
R. J. Matarese Separate Interdigital Electrodes Without Using Any Special Photolithographic Techniques (3,908,263)
D. Meyerhofer Liquid Crystal Devices of Improved Contrast (3,905,682)
D. Meyerhofer Controlled Angle Viewing Screens by Interference Techniques (3,909,111)
A. Meyerhofer Indexing System for Microfiche Viewer (3,909,123)
D. A. Moe Failure Detecting and Inhibiting Circuit (3,906,258)
S. Naroff Sheet Wrapping and Unwrapping Apparatus (3,908,981)
R. W. Nosker and L. P. Fox True Replication of Soft Substrates (3,904,488)
W. R. Roach and L. Darcy Deformable Mirror Light Value for Real Time Operation (3,905,683)
R. E. Rooney Cryogenic Dewar (3,909,225)
H. E. Schade Electron Tube Having a Semiconductor Coated Metal Anode Electrode to Prevent Electron Bombardment Stimulated Desorption of Contaminants Therefrom (3,906,277)
M. B. Shrader Vacuum Seal for Envelope Portions (3,904,065)
W. W. Siekanowicz Frequency Translator Using Gyromagnetic Material (3,906,408)
D. H. Vilkomerson and R. S. Mezrich Elastic Light-Scattering Modulator Device (3,907,407)
R. K. Walter Electronic Component Assembly (3,905,000)
D. H. Willis High Voltage Protection Circuit (3,906,304)
C. F. Wheatley, Jr. and O. Shevchenko Voltage Reduction Circuit for Deflection Yoke (3,904,927)
R. M. Wilson and W. J. Bachman Direction Indicating Display System (3,909,691)
S. Yuan and R. L. Camisa Digitally Controlled Oscillator Using Semiconductor Capacitance Elements (3,909,748)

AUTHORS

Lawrence A. Ezard received the B.S. in electrical engineering from The Pennsylvania State University in 1960, the M.S. in physics from Franklin and Marshall College in 1965, and the Ph.D. in electrical engineering from The University of Pennsylvania in 1970. In August 1960 Dr. Ezard was employed as an engineer by RCA, Lancaster, Pennsylvania. His work, during eleven years at RCA, included research, design, development, and evaluation of image tubes. More specifically, his area of study has included electron optics; photoemission; processing of multialkali, cesium-oxygen-silver, and III-V type semiconductor photocathodes; and phosphor screens. In 1966 he received an RCA Electronic Components and Devices Engineering Achievement Award for Image tube Development. He has been responsible for the design and development of more than a dozen image tubes during his association with RCA. In September 1971 Dr. Ezard accepted an appointment as Assistant Professor of Engineering at The Pennsylvania State University, The Capitol Campus, Middletown, Pennsylvania.

Dr. Ezard is a member of Eta Kappa Nu, Tau Beta Pi, and a senior member of the IEEEE. He is also a registered professional engineer in the state Pennsylvania.

Helmut Kiess attended the University of Stuttgart from 1953 to 1957 and the University of Darmstadt from 1958 to 1960. He received the doctor's degree from the University of Karlsruhe in 1963. Dr. Kiess joined the Laboratories RCA Ltd., Zürich, Switzerland in 1963 and since then has worked on the physics of photoconductors and insulators. During the period from July 1970 to April 1971 he was at RCA Laboratories in Princeton.

Gerard J. Mayer received the BE in electrical engineering from Villanova University in 1973. He is currently pursuing the MS at the University of Pennsylvania. Mr. Mayer is presently investigating the application of Charge Coupled Devices (CCD) to signal processing. He joined the RCA Missile and Surface Radar Division, Advanced Systems and Technology group, Morrestown, N. J., in 1973, where he has been involved in the design, implementation and evaluation of a developmental CCD clutter rejection system used to evaluate the signal processing potential of CCD's. He has prime responsibility for the development of CCD signal processing at MSRD, including a CCD radar pulse-compression system. Previous assignments included the design of subsystems for an advanced CMOS/SOS digital pulse compression signal processor. He developed a custom CMOS/SOS array which is a basic building block of the processor and implements a variety of signal processing functions. He has also performed system studies on image rejection, image jamming and cover pulse jamming for the Navy's AEGIS system. Mr. Mayer is a member of Eta Kappa Nu.

Adolph Presser received the B.E.E. degree from the Institute of Technology, Vienna, Austria, in 1950, and the M.E.E. degree from the Polytechnic Institute of Brooklyn, New York, in 1961. In 1959, Mr. Presser joined the RCA Microwave Technology Center at the David Sarnoff Research Center in Princeton, New Jersey, as a member of the technical staff. As a member of the Microwave Electronics section of this group, he has been engaged in the development of various solid-state microwave devices. His work includes the design and development of parametric amplifiers, tunnel-diode amplifiers, tunnel-diode frequency converters, and tunnel-diode oscillators. In 1965, Mr. Presser's field of interest shifted towards microwave integrated circuitry. He was instrumental in the design and development of telemetry transmitters, high-power transistor amplifiers, power sources for ECM systems, and more recently, of linear transistor power amplifiers and Doppler radar modules.

In 1964, Mr. Presser received the RCA Electronic Components Outstanding Performance Award and in 1965 the RCA Laboratories Achievement Award.

J. E. Roddy received a BS degree in Physics from Villanova University in 1966. He is presently pursuing a master's degree in Electrical Engineering at Drexel University. Since joining RCA's Advanced Technology Laboratories in 1966, he has worked on the development of laser and other electro-optic systems. He contributed to the modification and field support of the Ideographic Composing Machine—a display and printout system for Chinese, Japanese, and Korean languages. He was engaged in the development and testing of a 100-MHz FM laser signal recorder. He designed a wideband, low-voltage, electro-optic light modulator for this film recorder. He has analyzed and evaluated electro-optic components for use in laser signal and image recorders. Since 1968, Mr. Roddy has been active in evaluating laser hazards. He was a member of the ANSI Z-136 committee, which published a standard on the safe use of lasers in September 1973. He is presently investigating semiconductor lasers, acousto-optic deflectors, and photographic films for use in laser recording systems.

Mr. Roddy is a member of the IEEE.

Harold S. Veloric received the B.A. in chemistry from the University of Pennsylvania in 1951 and the M.S. and Ph.D. degrees in physical chemistry from the University of Delaware in 1952 and 1954, respectively. Dr. Veloric joined the Bell Telephone Laboratories in 1954 where he worked on the development of various types of silicon diodes including power rectifiers, voltage-regulatory diodes, computer diodes, and solar cells. He joined RCA Solid-State Division in 1958, where he worked on the design and development of high frequency transistors for consumer and computer applications. In 1960 he was responsible as Engineering Manager for the design and development of signal and switching transistors, and subsequently for MOS Engineering, Device Process Development, and RF transistor Engineering.

He is currently a Member of the Technical Staff of the Microwave Technology Center at RCA Laboratories, working on technology developments for the microwave group.

James P. Wittke received the M.E. degree from Stevens Institute of Technology, Hoboken, New Jersey in 1949, and the M.A. and Ph.D. degrees in physics from Princeton University, Princeton, N. J., in 1952 and 1955, respectively. His doctoral research was a precision microwave determination of the hyperfine splitting in atomic hydrogen. He was an instructor in physics at Princeton for one year before joining the technical staff of RCA laboratories, Princeton. At RCA he has engaged in paramagnetic resonance and microwave maser studies, in research on optically excited crystal lasers, and in investigations of the motions and properties of impurities in rutile. He has also worked on various classified projects. In 1967 Dr. Wittke was awarded an RCA Fellowship for a year of study abroad, which he spent at the Clarendon Laboratory at Oxford, England. Since then, he has studied the luminescence of heavily doped GaAs, helped develop new infrared-stimulated light emitting phosphors, and worked on the generation of ultra-short laser pulses, using mode-locking techniques. He is currently studying optical fiber communications systems, including measurements of the characteristics of fast-light-emitting diodes and of various low-loss fibers.

Dr. Wittke is a member of the Optical Society of America, IEEE, and of Tau Beta Pi and a Fellow of the American Physical Society.

Frank J. Woznlak attended RCA Institute from 1964 to 1966. Upon graduation, he worked at N.Y.U. where he took several technical courses. He joined RCA in 1969, working in the Defense Microelectronics Group in Somerville, N.J. In 1971, he transferred to the Microwave Technology Center at RCA Laboratories, Princeton, N. J., where he is engaged in the fabrication of components for microwave integrated circuits.

RCA Review

A technical journal published quarterly by RCA Research and Engineering in cooperation with the subsidiaries and divisions of RCA.

Index Volume 36, 1975

March 1975 Volume 36 Number 1

Optical Properties of Materials

June 1975 Volume 36 Number 2

September 1975 Volume 36 Number 3

December 1975 Volume 36 Number 4

Index to Authors, Volume 36, 1975

D. Redfield Optical Propteties of $SrTiO_3$ and $LiNbO_3$, March, p. 149
J. J. Risko A Study of Second-Harmonic-Extraction Trapatt Amplifiers for X-Band Operation, June, p. 274
J. E. Roddy Wideband Signal Recording on Film Using (AlGa)As CW Injection Lasers, December, p. 744
J. R. Sandercock Some Recent Developments in Brillouin Scattering, March, p. 89
J. H. Scott, Jr. Mobility of Current Carriers in Silicon-on-Sapphire (SOS) Films, June, p. 240
I. P. Shkarofsky Review on Industrial Applications of High-Power Laser Beams III, June, p. 336
R. W. Smith An X-Ray-Sensitive Fiber-Optic Intensifier Screen for Topography, September, p. 632
D. L. Staebler Time-Dependent Characteristics of Photo-Induced Space-Charge Field and Phase Holograms in Lithium Niobate and Other Photorefractive Media, June, p. 213
E. F. Steigmeier Coupled Lattice Modes in Light Scattering, March, p. 70
F. Sterzer The Conversion Efficiency of Ideal Shockley P-N Junction Photovoltaic Converters in Concentrated Sunlight, June, p. 316
F. Stockmann On the Concept of "Lifetimes" in Photoconductors, September, p. 499
E. Tosatti Optical Properties of Layer Structures Compounds, March, p. 40
H. S. Veloric Ultra-Thin RF Silicon Transistors with a Copper-Plated Heat Sink, December, p. 731
H. Weakliem Optical Properties of $SrTiO_3$ and $LiNbO_3$, March, p. 149
R. K. Wehner Coupled Lattice Modes in Light Scattering, March, p. 70
P. K. Weimer From Camera Tubes to Solid-State Sensors, September, p. 385
R. Williams Structure and Energy of the Interface Between an Insulator and Electrolyte, September, p. 542
J. P. Wittke Spontaneous-Emission-Rate Alteration by Dielectric and Other Waveguiding Structures, December, p. 655
P. J. Wojtowicz Two Dimensional Phase Transitions of Mobile Ions at SiO_2–Si Interfaces, March, p. 132
F. J. Wozniak Ultra-Thin RF Silicon Transistors with a Copper-Plated Heat Sink, December, p. 731
C. R. Wronski Semiconductor Heterojunction Vidicons, September, p. 425
S. Yuan Microwave Integrated-Circuit MIS Varactor Phase Shifter, June, p. 296